ADVANCEMENTS IN INKJET PRINTING TECHNIQUES FOR IMPROVING FIELD-EFFECT TRANSISTORS IN PRINTED ELECTRONICS

PARIA NADERI

A DISSERTATION SUBMITTED TO THE FACULTY OF GRADUATE STUDIES IN PARTIAL FULFILLMENT OF THE REQUIREMENTS FOR THE DEGREE OF DOCTOR OF PHILOSOPHY

GRADUATE PROGRAM IN ELECTRICAL ENGINEERING AND COMPUTER SCIENCE

YORK UNIVERSITY, TORONTO, ONTARIO

December 2023 © Paria Naderi, 2023

Abstract

This thesis centers on the enhancement of printed field-effect transistors (FETs) with a primary focus on addressing challenges through innovative inkjet printing methodologies. The study concentrates on the utilization of hydrophobic fluoropolymers, particularly Teflon amorphous fluoropolymer (Teflon-AF), as gate dielectrics in organic thin-film transistors (OTFTs). Teflon-AF, while promising for its low charge trap density, thermal stability, and low dielectric constant, presents impediments due to its low surface energy, resulting in issues like dewetting and bulging of printed patterns. This obstructs the creation of uniform lines using low-viscosity ink. To resolve these challenges, this thesis presents novel strategies for inkjet printing micro-patterns on hydrophobic surfaces.

Two approaches are outlined to successfully inkjet print micro-patterns on hydrophobic surfaces. The first involves a sequential inkjet printing and drying process, which maintains ink adherence to the surface. Meanwhile, an energy minimization technique predicts the equilibrium shape and volume of patterns, which is influenced by surface tension forces. The simulation accurately predicts the required ink volume for achieving dry patterns with smooth edges, advancing inkjet printing techniques for electronics. The second approach demonstrates stacked-coin methodology to form smooth lines on hydrophobic surfaces. Variations in drop spacing, stage speed, and stage temperature map out various regimes: isolated droplets, isolated groupings, broken lines, true stacked-coin, and delamination.

The study further investigates the fabrication of OTFTs employing Teflon-AF gate dielectric. Plasma treatment is applied to render the hydrophobic layer amenable to inkjet printing of silver electrodes. Morphological and surface chemical properties of Teflon-AF films change after plasma

treatment and gradually reverse after annealing of the electrodes. This affects the organic semiconductor/dielectric interface and, consequently, the OTFT performance.

Moreover, the research explores inkjet printing capabilities by incorporating carbon nanotubes (CNTs) into the TFT channel. Strategic utilization and engineering of the coffee ring effect in inkjet-printed CNT channel obviate the need for surface treatment. Inkjet printing leads to the aligning and bundling of CNTs on the line edges, which improves device performance.

To my parents,

Mahnaz and Mohieddin

Acknowledgments

My heartfelt appreciation goes to my supervisor, Prof. Gerd Grau, for giving me the opportunity to work in his group. Over the course of my doctoral studies, I was consistently granted the freedom to explore new avenues within my research. He always provided guidance and feedback while ensuring that I maintained autonomy over my work.

I would like to acknowledge the support of the Natural Sciences and Engineering Research Council of Canada (NSERC) for funding my Ph.D. studies at York University.

I extend my sincere gratitude to my esteemed committee members, Prof. Simone Pisana and Prof. Paul O'Brien, for their invaluable feedback on my work. I was extremely fortunate to take a course with Prof. O'Brien in my first year. His teaching made a lasting impact, and I am grateful for the experience. I would also like to thank my defense examiners Prof. Carmichael and Prof. Magierowski for their valuable feedback on my thesis.

I also wish to express my gratitude to Prof. Alidad Amirfazli for encouraging me and teaching me mentorship skills, which was paramount in boosting my confidence as a Ph.D. student. Working with him on two projects greatly contributed to my growth as a researcher.

Toward the end of my Ph.D. program, I had the privilege of doing a research internship at Karlsruhe Institute of Technology (KIT). Prof. Uli Lemmer and Prof. Gerardo Hernandez Sosa graciously accommodated my stay in their group at InnovationLab. Being exposed to such a professional and welcoming environment was an enriching experience.

I am thankful to my friends and colleagues at York University and KIT for their support and friendship: Mohamad Kannan Idris, Mehraneh Tavakkoli Gilavan, Iman Babaei Yazdi, Milad Ghalamboran, Yoland El-hajj, Christian Rainer, Lia Compos Arias, Dr. Ali Tunc, Ozan Karakaya, Kai Xia, Peter Krebsbach, Dr. Mikel Rincon-Iglesias and Luis Ruiz Preciado.

Finally, my deepest gratitude goes to my parents, Mahnaz and Mohieddin, and my siblings, Maziar, Parnian, and Bahram, for being pillars of my strength, hope, and happiness. I am grateful to my husband, Mohsen, for his never-ending love and patience. I am indebted to my dearest friends, Parisa and Ramin, for their companionship and kindness.

Table of Contents

List of Figures

List of Tables

List of Symbols

B_0	Bond number
C_{ox}	Oxide capacitance
I_d	Drain current
I_{off}	Off current
I_{on}	On current
R_c	Contact resistance
R_o	Output resistance
V_d	Drain voltage
V_g	Gate voltage
V_t	Threshold voltage
g_d	Conductance
g_m	Transconductance
θ_a	Advancing contact angle
θ_r	Receding contact angle
μ	Field-effect mobility
μ_0	Low-field mobility
SS	Subthreshold swing
T	Temperature
T_g	Glass transition temperature
r_{pin}	Pinned radius
r_{wet}	Wet radius
V_{pin}	Pinned volume
V_{wet}	Wet volume
V_{wet}	Dry volume
γ	Surface tension
η	Viscosity
ν	Velocity
ρ	Density
Re	Reynolds number
We	Weber number
Z	Z number

Chapter 1: Introduction

1.1. Printed electronics

Printed electronics offers many potential advantages, including low-cost and low-temperature manufacturing, chemical tailorability of materials, mechanical flexibility, and large-area printability [1]. Although it falls behind silicon electronics in terms of power consumption and performance, it offers more design and fabrication freedom both chemically and mechanically. There are areas where organic electronics can surpass the capabilities realized by the traditional silicon industry. It is possible to print materials with different functionalities including conductors, semiconductors, and insulators as long as they can be prepared in solution form. Stacks of devices and materials can be printed on a variety of substrates such as paper and textile. Therefore, it offers promising applications in health monitoring, smart packaging, and recyclable electronics.[1,2] An important research focus in the area of printed electronics is to explore simple, inexpensive and versatile fabrication processes for large-area electronics. Organic and carbon-based semiconductors can be deposited as thin films in electrical devices using solution processing techniques such as inkjet printing, extrusion printing, gravure, blade coating and spin coating.

Thin-film transistors (TFTs) are the fundamental components of many circuits, and improving their performance is a key to improving printed electronics[3–5]. For instance, conventional TFTs used in active-matrix backplanes are rigid and their fabrication needs chemicals for etching, masks, and expensive vacuum processes. One of the most important characteristics of semiconductors specifically for transistor applications, is carrier mobility. Carrier mobility is an important factor for the maximum switching speed in circuits, and it is still relatively low in organic semiconductors. New synthesis methods and solution processing techniques have been employed to achieve high carrier mobility in organic semiconductors. For instance, TIPS-pentacene organic thin-film transistors (OTFTs) with the mobility of 4.6 $cm^2/V.s$ have been achieved through solution sheering.[6] Considering that amorphous silicon carrier mobility is in the order of 1 $cm^2/V.s$ and it is sufficient for use in TFTs[7], the recent progress in solution-processed OTFTs is quite promising. Carbon-based semiconductors such as carbon nanotubes (CNTs) have high carrier mobility and since they can be formulated as printable inks, they are popular candidates for printed TFTs. CNT TFTs are used in flexible displays and electronic circuits, mainly as switches and invertors.[8–10] CNTs are robust and flexible and they have carrier mobilities in the order of 10 $cm^2/V.s$ even when solution-processed. Both OTFTs and CNT TFTs will be discussed in this thesis with the goal to improve their performance.

Direct-write printing methods such as inkjet offer the advantage of drop-on-demand (DOD) printing, which adds flexibility and creativity to the designs during the printing process. A wide range of devices can be inkjet-printed with high accuracy and resolution. Moreover, inkjet can be incorporated with other printing techniques. Inkjet printing has limitations as well, some of which are low throughput,[11] pattern formation dependency on surface wettability and post-printing challenges present in patterns with low viscosity ink. The inkjet printing process, its requirements and pattern formation challenges will be discussed in this chapter.

1.2. Inkjet printing

Inkjet printing is a direct-write printing technique that is advantageous for rapid prototyping and the ability to modify the design while printing.[12] Moreover, inkjet printing can cover a large range of film thickness and pattern width, and has high edge sharpness compared to other printing techniques.[13] Inkjet printing is a nonimpact printing (NIP) technique. This means that the ink transfer to the substrate is contactless, and therefore the substrate is not polluted by the printing equipment. The droplet formation can happen in two different ways: DOD and continuous. In DOD, the droplets are ejected only when they are needed. The inkjet printing equipment consists of a nozzle, ink reservoir, pressure control unit to keep the ink at the nozzle orifice, and a stage which holds the substrate. The nozzle can have either a thermal or a piezoelectric actuator which ejects droplets either by an electric pulse or thermal expansion, respectively. Figure 1-1 shows inkjet printing operation schematically. In the next section, ink and substrate requirements for inkjet printing are discussed as those topics will be addressed in the subsequent chapters.

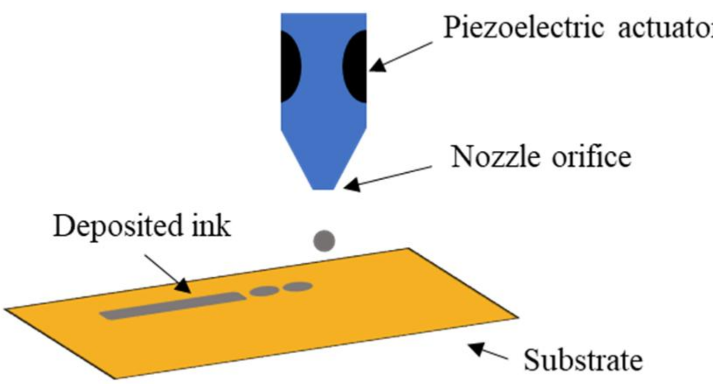

Figure 1-1. Inkjet printing operation

1.2.1. Inkjet printing requirements

In terms of printable materials, inkjet printing is applicable to inks that fall into a printability window. Printability is defined with ink properties such as viscosity (μ), surface tension (γ) and density (η). To define a printability range, two dimensionless numbers are used which show the interplay of interfacial, viscous, and inertial forces. These numbers are Reynolds number (Re) and Weber number (We):

$$Re = \frac{\upsilon a \rho}{\eta} \qquad 1\text{-}1$$

$$We = \frac{\upsilon^2 a \rho}{\gamma} \qquad 1\text{-}2$$

where ν, ρ, γ, and η are the ink velocity, density, surface tension, and viscosity, respectively, and a is the radius of the printing nozzle orifice. Z number is the ratio of Re over the square root of We and it is commonly used to define the printability window for inks. Generally, its lower and upper limits are defined by high and low viscosity inks, respectively.[14]

$$Z = \frac{Re}{We^{1/2}} = \frac{(\gamma \rho a)^{1/2}}{\eta} \qquad 1\text{-}3$$

In addition to ink properties and nozzle dimensions, the waveform produced by the piezoelectric actuator also affects the droplet formation. Waveforms can have different shapes such as unipolar, bipolar, and square. Figure 1-2a shows a 60 μm-diameter nozzle and a stable jetting of low viscosity ink. Prior to the printing of the pattern, the waveform is optimized for a stable droplet jetting. Figure 1-2b shows the waveform. Here, the waveform is bipolar and its parameters are pulse voltages (23 and -23 V), pulse rise and fall times (12 μs) and pulse dwell and echo times (40 μs).

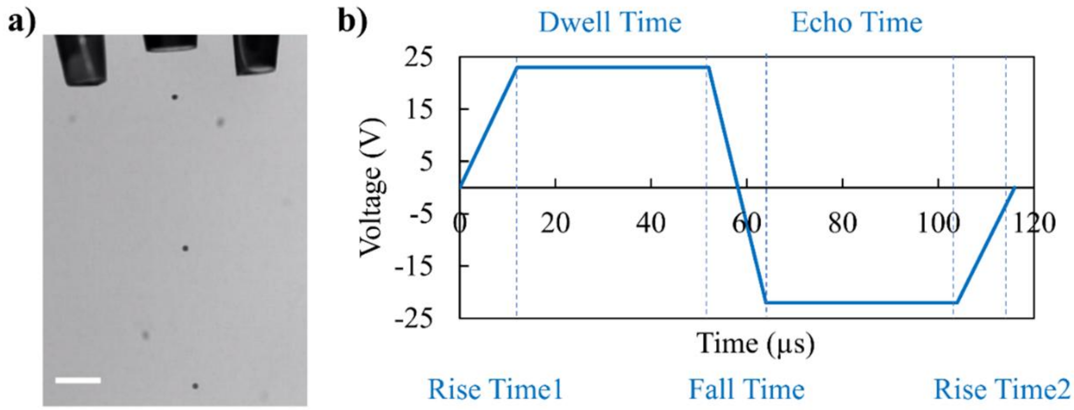

Figure 1-2. a) Microfab nozzle and a stable jetting of a low viscosity ink. The scale bar represents 500 µm. b) The waveform used to jet the ink.

1.2.2. Pattern formation with inkjet printing

To print high-resolution patterns, printing techniques such as inkjet and gravure are used.[15–17] For both of these techniques, the ink spreading and pattern formation are influenced by substrate wettability. After a droplet of liquid has been ejected from the nozzle and deposited on a substrate, before it dries, the pattern starts to form. The liquid, the substrate and the surrounding gas form a solid-liquid-gas three-phase system. As shown in Figure 1-3, the three phases come into a final equilibrium depending on the relative energies between them. Surface tensions of the three phases are linked to each other by Young's equation:

$$\gamma_{LG} cos\theta = \gamma_{SG} - \gamma_{SL} \qquad 1\text{-}4$$

Where γ_{LG}, γ_{SG} and γ_{SL} are surface tensions of the liquid-gas, solid-gas and solid-liquid interfaces. θ is the angle between the liquid and the solid and is called contact angle.

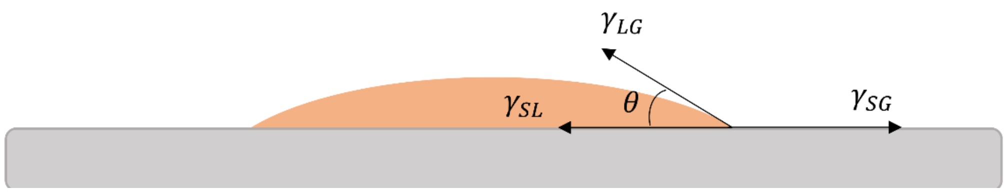

Figure 1-3. A droplet on a surface. Arrows showing surface tensions of the liquid-gas, solid-gas and solid-liquid interfaces. θ is the contact angle between the liquid and the substrate.

On surfaces with high wettability, the ink contact angle is below 90°, meaning that lines and other patterns can be printed. But if the contact angle is above 90°, the printed droplets will not spread to merge with each other and form patterns.[18] Usually, reporting an equilibrium contact angle is not enough to characterize the wettability of a surface. Two dynamic contact angle values are required. After droplet impact on the surface, if the surface is wettable, the droplet contact line will advance with an advancing contact angle (θ_a) until it stops and starts to recede with a receding contact angle (θ_r) until the droplet gets pinned on the surface and its contact line stays fixed and drying begins. The difference between these two angles is called contact angle hysteresis ($\Delta\theta$). According to Young's equation, $\Delta\theta$ is ideally zero, but factors such as surface roughness and contamination increase its value.[19] Surfaces with low wettability have low $\Delta\theta$, as their roughness is low. Figure 1-4a and b show images of droplets advancing and receding on surfaces with relatively high wettability. In this case, $\Delta\theta$ is high. Similarly, Figure 1-4c and d show images of droplets advancing and receding on surfaces with low wettability having low $\Delta\theta$.

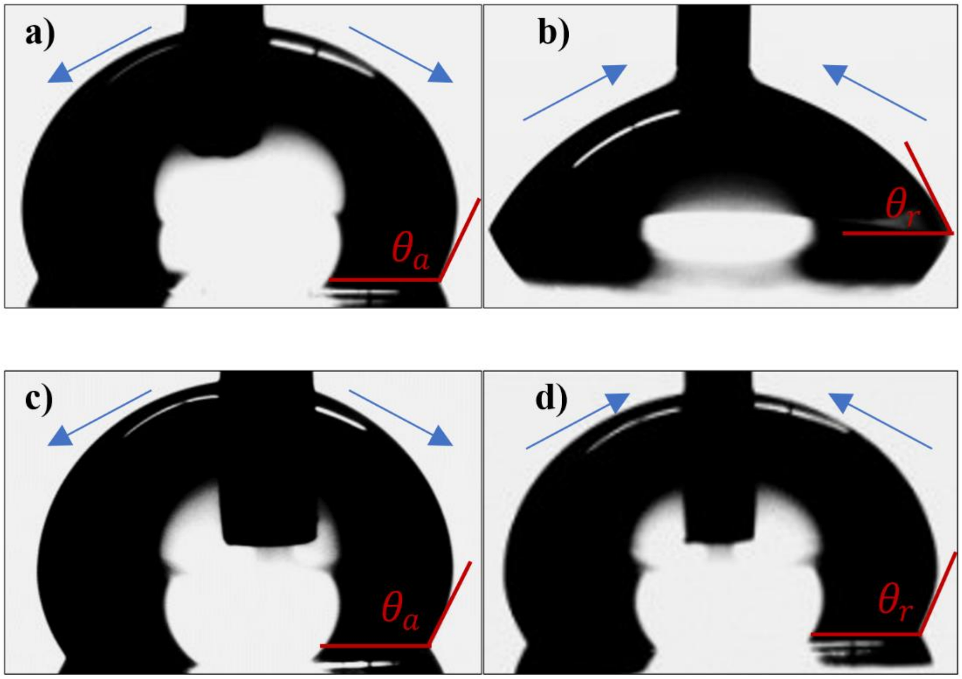

Figure 1-4. Images of droplets on surfaces with relatively high wettability (a) advancing and (b) receding. Similarly, droplets (c) advancing and (e) receding on surfaces with low wettability.

5.2.2.1. Line formation

In microelectronics, smooth patterns with low edge roughness are needed. For instance, when printing source and drain electrodes in transistors or gate electrodes in top-gate configurations, low line edge roughness will ensure accurate measurement of channel length and gate electrode overlap, respectively. In this thesis, the focus is on the simplest pattern as a building block for more complex patterns, devices, and circuits: lines. In chapter 2 and 3 the formation of smooth lines will be extensively discussed through experiments and simulations. Inkjet-printed silver lines are used as source and drain electrodes in OTFTs in chapter 4. Moreover, CNT lines with controlled thickness variation are inkjet-printed in the channel of TFTs in chapter 5. Therefore, in this section a brief overview of the subject is presented.

Different modes of behavior have been defined for inkjet-printed lines.[20,21] As shown in Figure 1-5, these different modes are individual drops, scalloped lines, smooth lines, bulged lines and stacked-coin lines. Contact angle, drop spacing and stage temperature determine the morphology of a printed line.

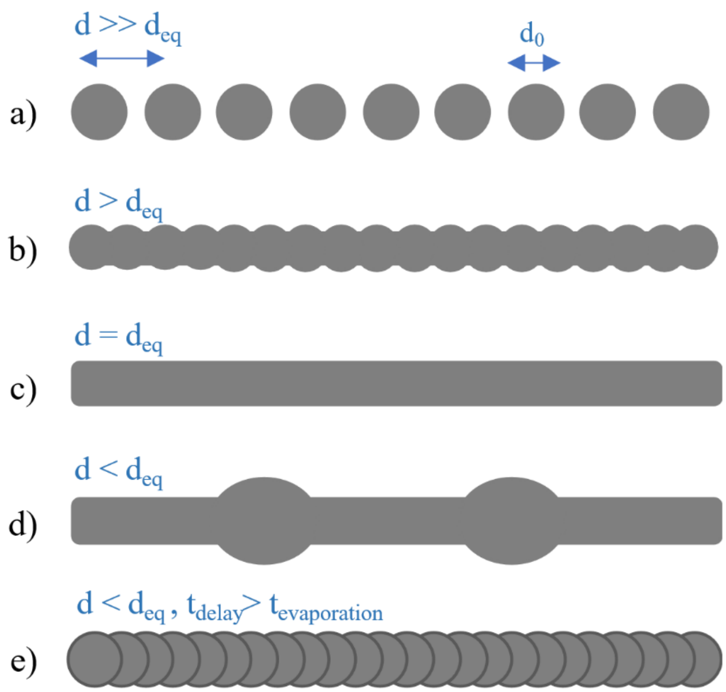

Figure 1-5. Different modes of behavior for printed lines: (a) individual drops, (b) scalloped lines, (c) smooth line, (d) bulged lines and (e) stacked-coin lines.

For ink droplets to coalesce and form connected lines, the drop spacing between consequent printed droplets (d) must be smaller than the diameter of the droplet on the surface (d_0). Therefore, the condition of $d < d_0$ must be satisfied, otherwise individual droplets are printed (Figure 1-5a). Equilibrium drop spacing (d_{eq}) is the drop spacing that leads to a smooth line with parallel edges. When $d > d_{eq}$ scalloped lines are formed (Figure 1-5b) and when $d < d_{eq}$ bulged lines are formed (Figure 1-5d). Only at $d = d_{eq}$ smooth lines are achieved (Figure 1-5c). All these morphologies occur when the ink evaporation duration is longer than the droplet deposition delay. If the ink evaporates faster than the droplet deposition delay, each droplet dries before the deposition of the subsequent droplet, leading to the formation of stacked-coin lines (Figure 1-5e). In this case, changing the drop spacing will not change the line width. This morphology will be discussed in detail in chapter 3.

1.2.3. Coffee ring effect

One of the primary challenges encountered in solution processing, involves the occurrence of the coffee ring effect. Coffee ring effect is the ring-shaped pattern that is left on the surface after a liquid pattern dries as depicted in Figure 1-6. During the evaporation process, the edge of the droplet evaporates faster. The contact line, which is the interface of the solid, liquid and the surrounding vapor, is pinned. The contact line tends to stay pinned, therefore, the loss of solvent is compensated by liquid flowing from center to the edges. As a result, this capillary flow takes most of the solute to the edges.[22] In short, two factors cause the formation of a coffee ring: The pinning of the contact line and the evaporation of the droplet from the edges. In the case of lines, the pattern will be linear instead of circular.

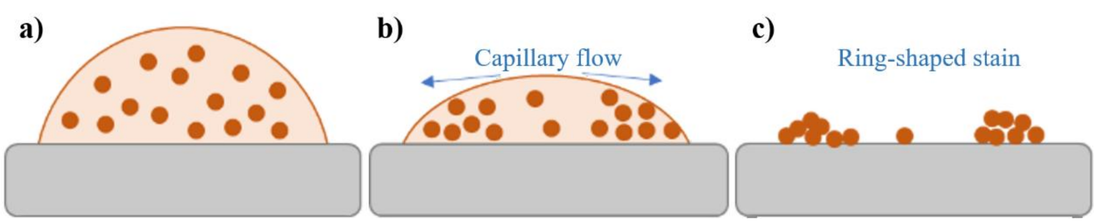

Figure 1-6. Coffee ring effect (a) droplet after deposition on the surface, (b) the drying and capillary flow moving the solute particles to the edges, and (c) the ring-shaped stain left on the surface.

Figure 1-7 shows an optical micrograph of printed silver source and drain electrodes on poly vinyl phenol (PVP)-coated glass and the thickness profile of the lines showing coffee ring effect on the line edges. In this case, coffee ring effect is not critical to the device performance. However, thickness variation in the channel of transistors is undesirable. Generally, efforts are made to avoid coffee ring effect and film thickness non-uniformity when a layer is solution-processed in a device.[23,24] In chapter 5, instead of eliminating coffee ring effect, we engineer it and take advantage of the carbon nanotube alignment in the printed line edges to improve transistor performance.

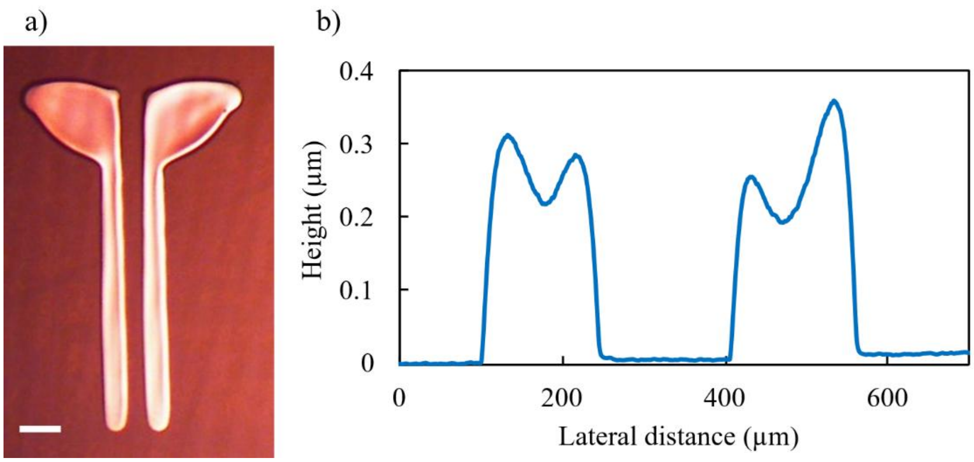

Figure 1-7. (a) Optical micrograph of printed source and drain electrodes on PVP-coated glass. (b) Thickness profile of the lines showing coffee ring effect on the line edges. Scale bar represents 200 µm.

In this dissertation, inkjet printing is used to fabricate TFTs. TFT electrodes and channels are inkjet-printed while interfaces are engineered to optimize device performance. Therefore, TFT structure and parameters are discussed in the next section.

1.3. Thin-film transistors

Solution-processed field-effect transistors (FETs) are getting a lot of attention due to their application in displays, biosensors and flexible amplifier circuits.[25] As was discussed earlier, in this thesis, we aim to investigate some challenges of solution processed electronic devices. For that purpose, transistors are used since they consist of multiple layers and thus their fabrication requires multiple processing steps. Therefore, to demonstrate difficulties that arise during both printing and processing steps such as annealing, we showcase two groups of transistors, OFETs and CNT TFTs. Then we turn those difficulties into opportunities to explore and improve the device performance. OTFTs are very similar to metal-oxide-semiconductor field-effect transistors (MOSFETs). TFTs have four layers: gate electrode, gate dielectric, source and drain electrodes, and the semiconductor (organic or inorganic). In MOSFETs, the substrate is doped silicon, and the source and drain electrodes are highly doped silicon regions with opposite polarity to the body to ensure low resistance contact to the terminals. The channel is formed when the polarity of the substrate inverts in a thin layer between the source and drain electrodes. In OTFTs, the substrate and the semiconductor are of different materials. The substrate does not have an electrical function, the semiconductor does not invert its polarity to conduct, and the source and drain electrodes are conductive materials that are deposited in contact with the semiconductor layer. Figure 1-8 depicts OTFTs in two configurations: bottom-gate top-contact, and bottom-gate bottom-contact. The same configurations can be applied to CNT TFTs as well, where instead of an organic semiconductor, carbon nanotubes are deposited in the channel region.

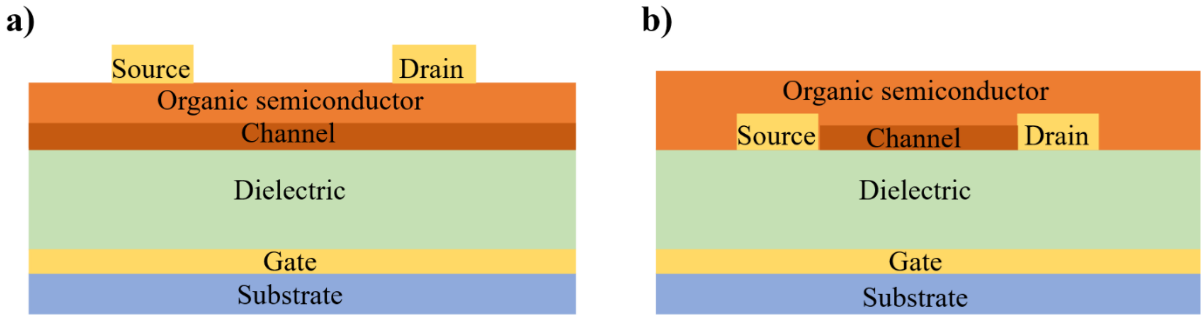

Figure 1-8. Organic thin-film transistors in (a) bottom-gate top-contact, and (b) bottom-gate bottom-contact configurations

1.3.1. TFT operation and parameters

To characterize TFTs electrically, output (I_{d}–V_{d}) and transfer (I_{d}–V_{g}) characteristics are studied. In this thesis, we fabricate TFTs and evaluate them based on their parameters. Those parameters are extracted from device I-V characteristics which we discuss here briefly.

The output characteristics (drain current (I_d) versus drain voltage (V_d)) has two regimes: linear and saturation. Linear and saturation drain current and voltage satisfy the following equations:

$$I_{d,lin} = \frac{W}{L}\mu C_{ox}[(V_g - V_t)V_d - \frac{1}{2}V_d^2] \qquad 1\text{-}5$$

and,

$$I_{d,sat} = \frac{W}{2L}\mu C_{ox}(V_g - V_t)^2 \qquad 1\text{-}6$$

Where W and L are the transistor channel width and length, respectively, C_{ox} is the capacitance of the dielectric layer, V_t is the threshold voltage, and μ is the charge-carrier mobility.

Field effect mobility (μ)

Field effect mobility is one of the most important parameters in a transistor. Field-effect mobility is the velocity of charge carriers in the presence of an external electric field. It is calculated from the slope of $I_{d}\_V_g$ in the linear regime and the slope of $\sqrt{I_{d}}\_V_g$ in the saturation regime:

$$\mu_{lin} = \frac{L}{C_{ox}WV_d}\frac{\partial I_d}{\partial V_g} \qquad 1\text{-}7$$

$$\mu_{sat} = \frac{2L}{C_{ox}W}(\frac{\partial\sqrt{I_d}}{\partial V_g})^2 \qquad 1\text{-}8$$

I_{on}/I_{off} ratio

I_{on} is the maximum transistor current at its maximum V_g and V_d values. It depends on many factors such as the length and width of the semiconductor channel, the charge field-effect mobility, the capacitance of the gate dielectric, and the device operating voltage. I_{off} is the minimum transistor current which ideally occurs when the transistor is switched off ($V_g = 0$). A large I_{on}/I_{off} ratio will distinguish between on-state and off-state of a transistor, and it is a determining factor in designing digital circuits.

Threshold voltage (V_t)

When increasing V_g, the transistor current will start increasing after the interfacial traps are filled. The onset voltage for the transistor to turn on is called threshold voltage (V_t). Its most common method of extraction is using the extrapolation of the square root of I_d versus V_g in saturation regime , and the extrapolation of I_d versus V_g in linear regime[26]:

$$V_{t-sat} = V_g - \frac{\sqrt{I_d}}{\partial\sqrt{I_d}/\partial V_g} \qquad 1\text{-}9$$

and,

$$V_{t-lin} = V_g - \frac{I_d}{\partial I_d/\partial V_g} \qquad 1\text{-}10$$

Subthreshold swing (SS)

Subthreshold swing (SS) is another parameter that indicates the presence of charge traps, and it is defined as the inverse slope of I_d (in log scale) versus V_g. SS shows how fast a device switches from off state to on state, and it has the units of V/decade (meaning: the amount of increase of V_g needed to cause a 10-fold increase in I_d). It is defined as:

$$SS = \frac{\partial V_g}{\partial(log_{10} I_d)} \qquad 1\text{-}11$$

Output resistance (R_o)

The conductance of a transistor is equal to the slope of the $I_d - V_d$ curve. The output resistance is equal to the inverse of the conductance:

$$R_o = \frac{1}{g_d} = {dI_d}/{dV_d} \qquad 1\text{-}12$$

Output resistance in the linear regime depends on contact resistance, which is an important factor in transistor performance. Contact resistance will be used to explain the results in chapters 4 and 5. Therefore, in the next section its definition and different extraction methods will be discussed.

1.3.2. Contact resistance in OTFTs

As voltage is applied to the channel through source and drain electrodes, in addition to channel resistance, the total applied voltage drops at the semiconductor/metal contacts interface due to contact resistance:

$$V_{tot} = \Delta V_s + \Delta V_{ch} + \Delta V_d = I_d(R_s + R_{ch} + R_d) \qquad \text{1-13}$$

and,

$$R_c = R_s + R_d \qquad \text{1-14}$$

ΔV_s and ΔV_d are voltage drops across the source and drain electrodes, and R_s and R_d are the contact resistance (R_c) at source and drain terminals, respectively. ΔV_{ch} and R_{ch} are channel voltage drop and resistance across the semiconductor channel. R_{ch} is assumed proportional to the channel length, but if the channel length is too small, R_c will dominate the device, and it will become difficult to get accurate resistance values [27].

There are different methods of measuring and extracting contact resistance in transistors. In this dissertation, I-V measurements are used with two extraction methods: transfer length method (TLM) and Y-function method (YFM).

5.2.2.2. Transfer length method (TLM)

TLM is the most widely used contact resistance characterization method in OFETs. In this method, devices with different channel lengths and fixed channel widths are fabricated. Then, their total output resistance is extracted using the inverse of the slope of the output characteristics in the linear regime. The total resistance is the sum of contact resistances ($R_c = R_s + R_d$) and the channel resistance (R_{ch}).

$$R_{tot} = R_s + R_d + R_{ch} \qquad 1\text{-}15$$

As an example, in Figure 1-9, the width normalized total resistance ($R_{tot}W$) values of an OFET are plotted versus the channel length. The y-intercept of the line equation gives R_cW. With $W = 1300$ µm, R_c is calculated to be 12 $K\Omega$. One disadvantage of TLM is that the reported value is an average over several devices. Moreover, it is sometimes difficult to find a good linear fit to extract contact resistance due to large parameter variations from one device to another[28].

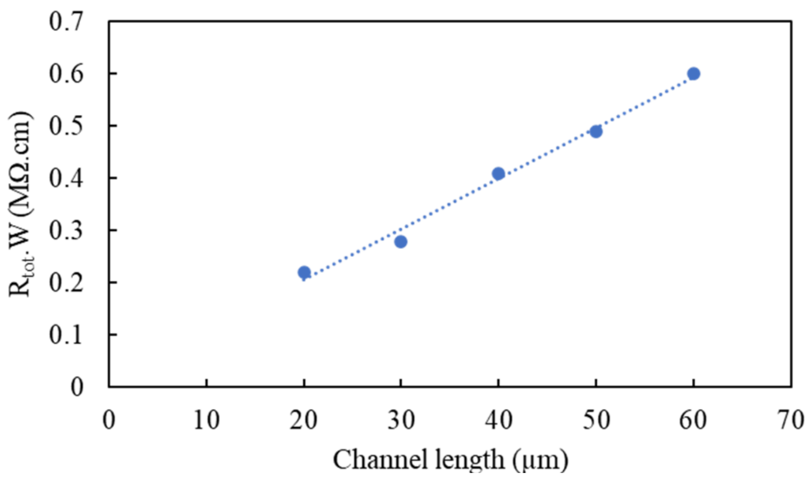

Figure 1-9. R_{tot}.W versus channel length in an OFET

5.2.2.3. Y-function method (YFM)

YFM is a simple and efficient method to extract low-field mobility, contact resistance and threshold voltage. Low-field mobility is the intrinsic carrier mobility of the transistor, which is not affected by contact resistance. When compared with extracted field-effect mobility values from other methods, low-field mobility provides information on how voltage drop affects carrier transport in the channel. The main advantage of YFM is the possibility of contact resistance extraction from a single device. The YFM technique is introduced in detail in Ref. [28]. In YFM, the transfer characteristic in the linear regime is used. Using the current equation in the linear regime, the Y-function is defined as:

$$Y = \frac{I_d}{\sqrt{g_m}} = \sqrt{\frac{W}{L} C_{ox} \mu_0 V_d} \times (V_g - V_t) \qquad 1\text{-}16$$

where g_m is the transconductance, W and L are the channel width and length of the transistor, C_{ox} is the dielectric capacitance per unit area, μ_0 is the low-field mobility, V_d is the drain voltage, and V_t is the threshold voltage. From the slope of Y versus V_g, μ_0 is obtained and from the x-intercept, V_t is extracted (see Figure 1-10a). Next, $\frac{1}{\sqrt{g_m}}$ versus $V_g - V_t$ is plotted, using the equation below:

$$\frac{1}{\sqrt{g_m}} = \frac{1 + \theta(V_g - V_t)}{\sqrt{\frac{W}{L} C_{ox} \mu_0 V_d}} \qquad 1\text{-}17$$

Finally, from the x-intercept, θ and contact resistance are extracted (see Figure 1-10b). θ is the mobility attenuation factor and it leads to the extraction of contact resistance:

$$\theta = \theta_0 + \theta^* = \theta_0 + G_m \times R_{sd} \qquad 1\text{-}18$$

$$G_m = \frac{W}{L} C_{ox} \mu_0 \qquad 1\text{-}19$$

where θ_0 (≈ 0), G_m and R_{sd} are the mobility reduction coefficient, transconductance parameter, and the source-drain contact resistance, respectively. In our calculations we ignored θ_0, and assumed the carrier mobility to be constant under the applied vertical field. This assumption ignores phonon scattering in the channel. As a result, comparisons with TLM show an overestimation of contact resistance.[29]

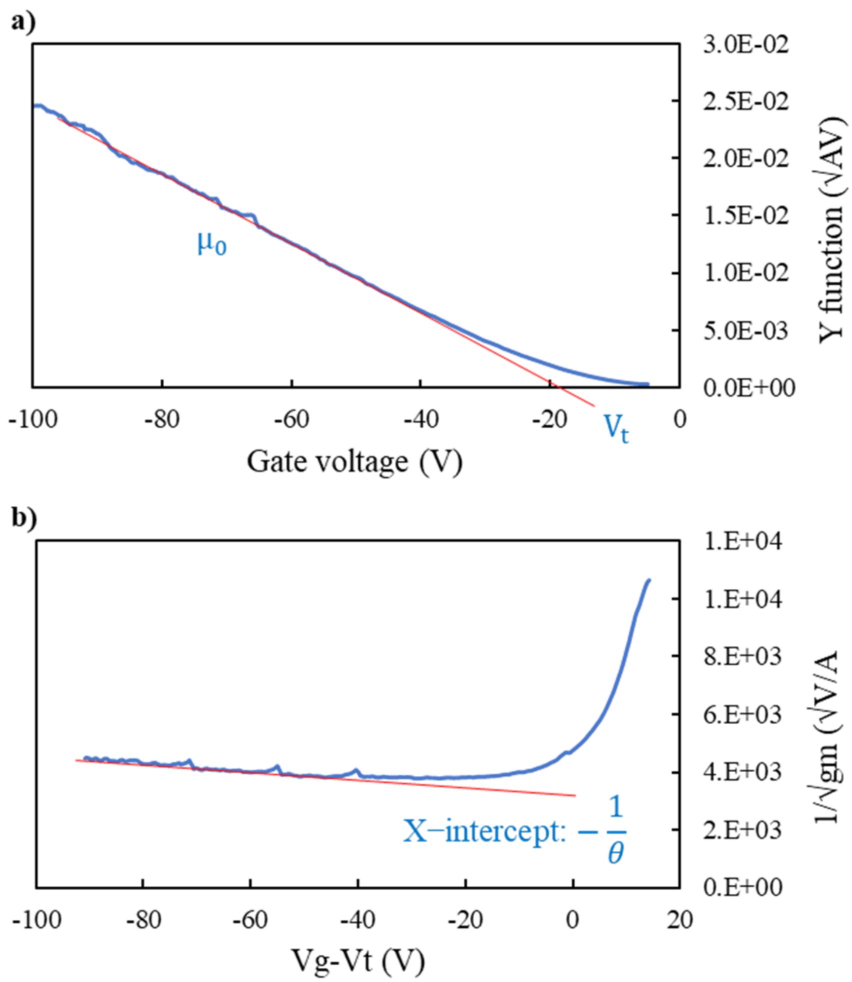

Figure 1-10. a) Y function versus gate voltage, b) $\frac{1}{\sqrt{g_m}}$ versus $V_g - V_t$

1.4. Motivation

Solution-processed field-effect transistors have key applications in flexible electronics, biomedical devices, energy harvesting and storage systems, and smart packaging. Their fabrication is cost-effective, scalable, and versatile. In this thesis, fabrication challenges in the areas of inkjet printing and challenging surfaces such as surfaces with low wettability will be discussed.

Multifaceted challenges are encountered when attempting inkjet printing on hydrophobic surfaces.[30,31] These challenges are prevalent in various fields, notably microelectronics and biological applications, where achieving high-resolution patterns on such surfaces proves to be a complex task. Hydrophobic fluoropolymers have many applications such as coating material, circuit encapsulation and gate dielectric in field-effect transistors.[32–35] While printing methods such as extrusion and screen printing are less influenced by substrate wettability, their resolution is limited. To achieve high-resolution patterns, inkjet printing is employed, but on surfaces with low wettability, issues arise. Adjacent droplets tend to merge and bulge, deviating from the intended pattern. Surface modification can increase surface wettability, but it requires extra steps and equipment, moreover it can change the surface morphology and chemical composition.[36–41] Techniques such as symmetric printing, stacked-coin lines, and simulations to predict ink behavior have been proved successful in producing patterns on hydrophilic surfaces,[17,21,42,43] however they have not been investigated on hydrophobic surfaces.

The utilization of hydrophobic fluoropolymers like Teflon amorphous fluoropolymers (Teflon-AF) in TFTs offers numerous advantages, such as water-repellency and smoother dielectric surfaces, leading to enhanced performance by reducing defects in the organic semiconductor (OSC) channel.[32,44] Despite these benefits, incorporating hydrophobic fluoropolymers into solution-processed electronic devices poses considerable challenges. One of the key obstacles is the difficulty in fabricating transistors with small channel lengths due to the necessity of high wettability surfaces for inkjet-printed source and drain electrodes. Plasma treatment, a commonly used method to increase wettability, changes surface properties such as roughness and chemical composition without affecting the bulk material, but it can influence the surface chemically and morphologically, potentially altering carrier transport.[41] Consequently, many reports limit OTFTs with hydrophobic gate dielectrics to vacuum-processed electrodes, mainly due to the complexity of printing electrodes onto a hydrophobic dielectric.[45,46]

Inkjet printing stands out as a highly promising method for depositing CNT inks in the channels of TFTs,[47,48] owing to its widespread use in creating CNT-based devices like TFTs,[10,48–50] strain and chemical sensors,[51,52] and conductive films[53,54]. CNT ink formulations have been designed to accommodate a high percentage of semiconducting CNTs,[55,56] offering a viable solution for inkjet printing and providing an effective means of regulating the distribution of CNTs within the TFT channel.[57–59] Different deposition techniques often involve trade-offs; high-density techniques like drop casting or spin-coating offer high field-effect mobilities but result in lower on-off current ratios, whereas low-density methods like inkjet printing generally achieve higher on-off current ratios at the expense of lowering the field-effect mobility.[8,60–64] These challenges have led to exploring innovative strategies to improve CNT TFT performance by controlling CNTs' placement within the TFT channel.[57–59] Coffee ring effect, although typically a challenge causing tube aggregation on pattern edges, [22] can be leveraged as a natural mechanism, eliminating the need for surface treatment[65] or the use of multiple solvents[66–68]. With inkjet printing, CNTs can be aligned on droplet edges as a result of capillary flow.[53,69] And, since the performance of CNT TFTs improves by regulating CNTs inside the TFT channel using solution processing techniques, [57–59] coffee ring effect can be utilized and engineered to enhance transistor performance. This technique allows precise manipulation and control over CNTs' distribution within the channel, effectively regulating their alignment and density, critical factors influencing the device's electrical performance.

In summary, the inherent capabilities of inkjet printing to finely deposit inks on challenging surfaces and its applicability for printing low viscosity inks play a crucial role in addressing the intricate trade-offs typically encountered in TFTs. The aim of this thesis is to tackle the above-mentioned challenges and take advantage of inkjet printing as a technique to deposit high-resolution features with low viscosity inks.

1.5. Thesis Organization

As discussed in the previous section, in this dissertation, inkjet printing is utilized to form thin films of material that have implications as micropatterns on challenging surfaces, conducting electrodes in TFTs, and aligned carbon nanotubes in the TFT channel. Here, the content of each chapter is briefly introduced. In this thesis, first, two approaches to inkjet printing patterns on hydrophobic surfaces are discussed. Then, OTFTs with inkjet-printed electrodes incorporating a hydrophobic dielectric with reversible surface properties are presented. Finally, inkjet printing is used to align carbon nanotubes in the TFT channel.

In chapter 2, the challenge of inkjet printing on hydrophobic surfaces is tackled through sequential printing and drying and controlled surface energy minimization. The use of a sequential printing and drying process, coupled with computational modeling, becomes an innovative strategy to create micro-patterns on such surfaces without the need for blanket surface modification. This approach enables the creation of hydrophilic/hydrophobic regions by inserting a drying step in the printing process. Subsequently, this technique forms precise micro-patterns using a combination of inkjet printing and drying sequences, which aids in regulating and predicting ink volumes necessary for specific pattern dimensions.

In chapter 3, another approach to inkjet printing conductive lines on hydrophobic surfaces is demonstrated. In stacked-coin methodology, an interplay of printing speed, drop spacing and stage temperature leads to the formation of smooth lines. Stacked-coin printing, proven effective for creating conductive lines on hydrophilic surfaces, involves depositing subsequent droplets with longer delay than the evaporation time of the prior droplet. This allows wet ink to adhere to the previously dried ink area. By expediting the ink's drying rate through stage heating and studying different regimes, the adapted stacked-coin method becomes applicable on hydrophobic surfaces.

In chapter 4, a hydrophobic material (Teflon-AF) is used as the gate dielectric in OTFTs. It is shown that plasma treatment as a surface modification technique changes the morphological and chemical properties of Teflon-AF surface which are reversed with a subsequent annealing step in the device fabrication process. The source and drain electrodes are inkjet-printed with a 20 µm channel length on plasma treated Teflon-AF and are later annealed. This annealing step acts as a post-annealing step for Teflon-AF and depending on the temperature, its surface properties are reversed, which affects the transistor performance. Understanding the reversible nature of Teflon-AF surfaces becomes pivotal in engineering the interface between OSC and dielectric, impacting the OTFT performance. The study reveals that post-annealing after plasma treatment plays a significant role in reversing the effects of surface modification, enhancing the transistor performance by reducing surface roughness and altering wettability and reactive elements on the surface.

In chapter 5, inkjet printing is used to regulate CNTs in the TFT channel. Through inkjet printing, thin films of low viscosity inks are deposited and when such inks are dried, very often a phenomenon called coffee ring effect occurs. Efforts are usually made to avoid coffee ring in devices such as transistors where channel thickness and roughness are required to be minimum for better charge carrier transport. Here, the coffee ring effect is managed and transformed into an advantageous mechanism. By using inkjet printing, the need for additional surface treatments or complex multi-solvent systems is avoided. By carefully engineering the coffee ring effect in the CNT film, low resistance aligned CNTs are achieved through CNT bundling. The research highlights the importance of inkjet printing as a scalable and cost-effective solution for producing high-quality CNT TFTs, aligning with the nature of solution-processed printed electronics.

Finally, chapter 6 provides a summary and conclusion of all the chapters with insights into possible areas for future research.

Chapter 2: Controlled pattern formation on hydrophobic surfaces using sequential drying and surface energy simulations

This chapter was published in The Journal of Chemical Physics, Copyright AIP Publishing.

Paria Naderi, Benjamin Raskin Sheuten, Alidad Amirfazli, Gerd Grau; Inkjet printing on hydrophobic surfaces: Controlled pattern formation using sequential drying. *J. Chem. Phys.* 14 July 2023; 159 (2): 024712. https://doi.org/10.1063/5.0149663

2.1. Introduction

In this chapter, an approach to inkjet printing on a hydrophobic surface is discussed. It is often inevitable to use hydrophobic films such as Teflon amorphous fluoropolymers (Teflon-AF) as a coating material, device encapsulation, or the gate dielectric in transistors.[32–35] Since later in the thesis, the fabrication of OTFTs with Teflon-AF as gate dielectric is presented, pattern formation on such surfaces is investigated here in detail. The formation of micro-patterns on surfaces with low wettability, seen in applications such as microelectronic devices and bio-surfaces with cell-based assays poses a significant challenge.[30,31] Printing techniques such as extrusion and screen printing are not as influenced by substrate wettability compared to other techniques, but their resolution is low.[70,71] To print high-resolution patterns, inkjet printing and gravure printing are used.[15–17] For both of these techniques, the ink spreading and pattern formation are influenced by substrate wettability. On surfaces with low wettability, adjacent droplets merge and bulge into larger circular drops rather than maintain the printed pattern such as a line or square. Consequently, to deposit functional inks on hydrophobic surfaces, for instance, as conducting electrodes in printed electronics, a common approach is to increase the wettability of the surface using surface-modification.[72] For example, to achieve finer thin-film patterning through printing, surfaces with hydrophilic/hydrophobic adjacent regions can be created with plasma treatment. The ink wets the hydrophilic region and is confined by the hydrophobic regions.[73] However, in addition to adding extra manufacturing steps to the process, surface treatment methods such as plasma[36–41] and addition or removal of monolayers[74,75] may alter the surface both chemically and physically[37], potentially compromising the functionality of the printed micro-patterns.[35]

There are some ways of forming micro-patterns on hydrophobic surfaces without resorting to surface modification. One approach is the chemical modification of the ink, for instance by using gelation polymers mixed with TiO_2 ink, where the thermal gelation of the ink prevents it from dewetting the hydrophobic surface and helps forming straight lines[76]. This approach requires modifying the ink formulation, which may not always be a viable option. On the other hand, stacked-coin lines have been inkjet-printed on surfaces with high wettability.[21] In this method, the printing stage is heated and the ink is dried immediately after it is deposited on the substrate. Ideally, each droplet is dried before it retracts, and the subsequent droplet is pinned on the previous droplet. When printing stacked-coin lines, the heat from the print stage can cause the solvent to evaporate in the nozzle and hinder droplet jetting due to ink agglomeration[21]. While it helps with pinning the droplets on the surface, it is more applicable to solvents with high boiling point, and due to the high temperature condition, it is not considered as a general method. Stacked-coin method will be extensively studied in the next chapter, where we demonstrate successful inkjet printing of lines on Teflon-AF within a defined temperature and speed range.

Another technique for forming ink patterns on hydrophobic substrates involves printing of the corners of a rectangle and drying them, followed by the deposition of ink between those corners, which is then stretched by the previously dried corner droplets.[77] However, in Ref [77], the focus was to use the printed pattern as a fully-overlapped transistor gate electrode without the need for accurate patterning, low edge roughness, or high resolution. In a similar study leveraging surface tension forces, high-resolution lines were formed by sandwiching a layer of ink between a pre-patterned substrate with printed dots and a cover plate. Bridges were formed between the dots as the ink solvent evaporated.[78] While smooth and well-controlled lines were formed with this method, the process requires careful control over the dewetting process limiting the types of patterns that can be printed. Additionally, the entire surface is initially covered with the ink, which may pose difficulties for complex multi-layer devices.

When lines are inkjet-printed on surfaces regardless of wettability, the beginning of the patterns tend to bulge due to Laplace pressure gradient between an already printed larger volume with lower curvature and the newly printed droplet with higher curvature. One way of preventing inkjet-printed lines from bulging at the beginning of the line is to use symmetric printing.[17] With symmetric printing, three-droplet line segments are printed with the middle droplet being printed last. This method prevents the bulging at the beginning of printed patterns[17,79] on surfaces with high wettability, however it has not yet been explored on surfaces with low wettability. There is a need to understand and control the printed line formation process on hydrophobic surfaces through the development of novel methods.

Simulations can be used to predict printed ink behavior on a surface and prevent waste of material and time, while providing better understanding of the pattern formation. Different simulation methods have been employed to predict the formation of micro-patterns, for example, the Navier-Stokes and continuity equations,[80,81] the lattice Boltzmann equation,[82,83] and the energy minimization integral.[42] Among these methods, the energy minimization approach is simple, time-efficient, and it can emulate the shape of micro-droplets with a high level of accuracy to find a steady-state solution.[43] This method finds the equilibrium state of the droplet by calculating its energy using the surface integral of the applied forces. The minimum energy state for the system represents the equilibrium state.[84,85] Surface Evolver is a popular simulation tool that uses gradient descent method to minimize the energy to study the equilibrium state of droplets by taking into account forces such as surface tension, and gravity.[84] The energy is minimized using the gradient descent method, in which each vertex on the surface of the body has an energy and a force that acts on it. The total energy of the surface is a function of the coordinates. The negative of the energy gradient is the force which has a direction from higher to lower energy and moves the vertex in that direction to define the shape of the interface in an iterative process. As such, when running the simulation, the system, through iterations and refinements, moves vertices simultaneously to minimize the surface energy.[84] Gradient descent method is a popular method to find the minimum energy state, but it can have challenges. For example, achieving good convergence by employing the gradient descent method alone, is often not possible[42]. One challenge with the energy minimization method is the accurate modelling of the contact angle at the discontinuities between regions of different wettabilities. At these boundaries, the energy minimization integral fails to work. One way of dealing with this problem is replacing the gradient descent method with a direct search method at the boundaries,[42,43] which means using two different methods for the different areas. This approach requires more time and alternating between two algorithms.

To overcome the challenge of printing on hydrophobic surfaces, here a combination of simulation and experimental approaches is demonstrated, following the strategy below. To produce micro-patterns on a hydrophobic surface, silver nanoparticle ink is inkjet-printed on Teflon-AF films. The method uses printing and drying sequences, where hydrophilic/hydrophobic regions are created on the surface without blanket surface modification. The dried ink from the first printing sequence acts as the hydrophilic region as the high silver nanoparticle content of the ink renders it hydrophilic. The desired pattern is formed in the second step by depositing and drying more ink on the hydrophobic region between pre-printed anchors. In other words, with an adaptation of the symmetric printing methodology, patterns are inkjet-printed on hydrophobic surfaces, with a drying step to be inserted into the symmetric printing process to form line segments. Schematics of the sequential printing and drying steps to form micro-patterns are shown in Figure 2-1. The edge profile of the line is influenced by the volume of the printed ink. It is crucial to have the ability to anticipate and regulate the required volume of ink for a specific line length, particularly in areas such as microelectronics where pattern dimensions determine electrical performance. Instead of experimental trial and error methods to determine accurate micro-pattern dimensions, a computational model was devised based on energy minimization with Surface Evolver to predict the ink volume required to print line segments with different lengths and other patterns such as triangles. The printed patterns are simulated and analyzed with only the contact angle of the ink on the substrate as an input parameter. This allows us to confirm whether surface tension is the main force controlling the equilibrium state of micro-patterns obtained through the sequential print and dry method. The simulation results are used to predict the printed volume necessary to print smooth patterns after drying.

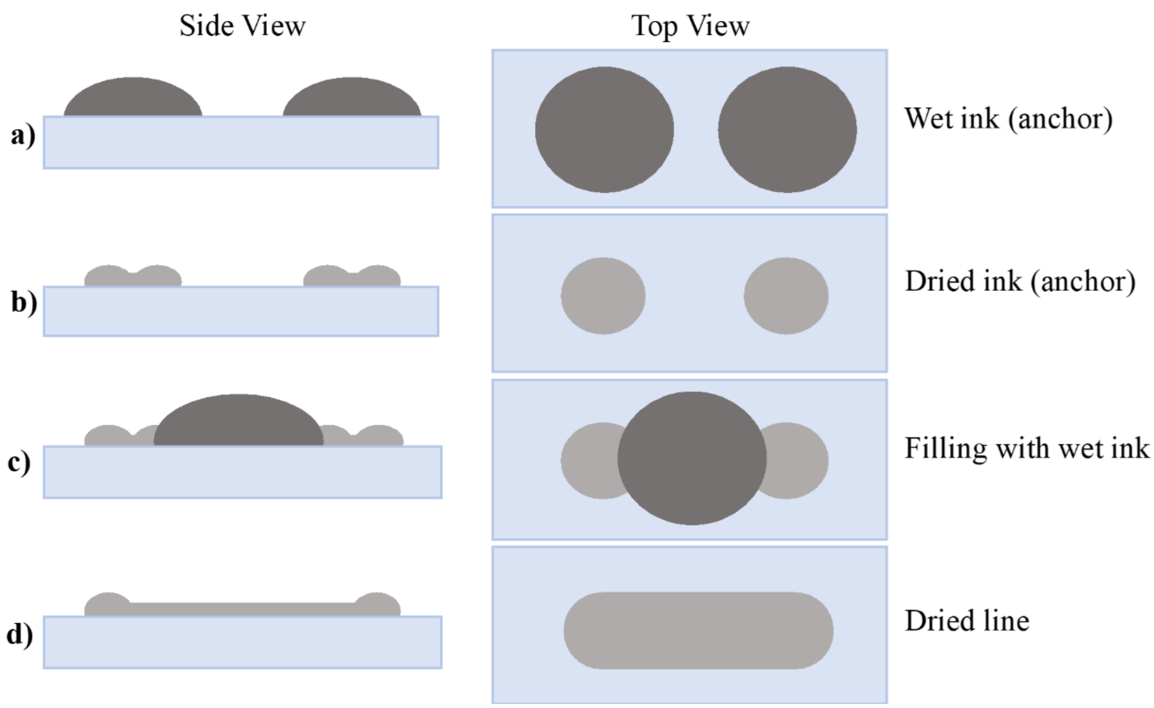

Figure 2-1. Schematics of the side and top views of the sequential printing and drying of the micro-patterns with the following steps: (a) Print the first sequence of droplets, (b) dry droplets, (c) print the second sequence of droplets, and (d) dry final pattern.

2.2. Experimental

Teflon-AF 1600 (Sigma-Aldrich, Oakville, Canada) was used as the hydrophobic surface. It was dissolved in Fluorinert FC-40 (Sigma-Aldrich, Oakville, Canada) with a 1.6% concentration. The Teflon-AF solution was spin-coated at 500 rpm for 1 minute on glass slides and dried at 150 °C for 15 minutes. Two printing approaches were used for printing lines, i.e., the traditional method (method 1) and the sequential printing and drying method (method 2). In this thesis, a custom-built inkjet-printer with a 60 μm-diameter nozzle (MJ-ATP-01-60-8MX, Microfab Technologies, Inc. Plano, TX) was used. And, for the micropatterns, silver nanoparticle ink (ANP DGP 40LT-15C, Advanced Nano Products, Co., Sejong, Korea) was used. In the traditional method, single droplets (volume 0.19 nL) were printed with different spacing, i.e., the drop spacing of the printed single droplets was varied between 10-85 μm. In the sequential printing and drying method, first, two anchors each comprising of 10 droplets (volume 1.9 nL) were printed at different distances from each other (170-260 μm). Next, the printed anchors were dried at 150 °C for 15 minutes. Finally, different volumes of the ink were printed between the two anchors. For each anchor spacing between 170-260 μm, first a minimum volume of ink was printed to connect the anchors. Then, the volume was increased droplet by droplet, to find where a relatively smooth line will form.

2.3. Simulations

To model the line pattern formed by the sequential printing and drying method, Surface Evolver was used. The surface in general is defined as a complex of vertices, edges and facets. A vertex is a point with coordinates. An edge is defined by the head and tail vertices, and each facet is defined by at least three edges. A body is defined by the facets that make up its boundaries. The body initially has an approximate shape (but accurate volume), and later approaches the desired shape defined by the imposed constrains through an iterative evolution. The surface energy is the integral of the forces acting on the surface. For instance, if the force is only surface tension, we can write the energy as:

$$E = \int\int_{facet} -T\vec{k}.\overrightarrow{dA} = \int\int_{facet} -T\cos\theta . dA \qquad 2\text{-}1$$

where T is the surface tension, $\vec{k}$ is the surface tension unit vector, A is the area of the facet, and θ is the contact angle of the liquid on the solid surface.

In the present work, the system was defined as two regions having ink contact angles of 84°±2° for printing surface and 0° for anchor region. Figure 2-2 shows the advancing and receding contact angles of silver ink and deionized (DI) water on Teflon-AF. The contact angle of the silver nanoparticle ink on a Teflon-AF film is 84°±2°. Although the surface is not as non-wetting as it is for water with a contact angle of 120° ± 2°, it is still considered as non-wetting in practice. Since Teflon-AF has low wettability, the contact angle hysteresis is low. The above-mentioned contact angles are average values of the advancing and receding contact angles. The contact angle of DI water and silver ink on Teflon-AF and dry silver ink were measured using the sessile drop method (Krüss DSA10, Krüss Scientific, Germany).

In the simulation, gravity was ignored since the printed features are in the micro scale with a Bond number (Bo) equal to 4.13×10^{-3}. Bo is the ratio between gravitational and surface tension forces:

$$B_0 = \frac{R_0^2 \Delta w}{\gamma} \qquad \text{2-2}$$

Where R_0 , Δw and γ are liquid spherical droplet radius, liquid/vapor specific weight difference (density) and surface tension respectively. $\Delta w = w_{silver} - w_{air} = \rho g_{silver} - \rho g_{air}$, and $w_{air} = 12.6\ N/m^3$. Silver nanoparticle ink properties are given in Table 2-1.

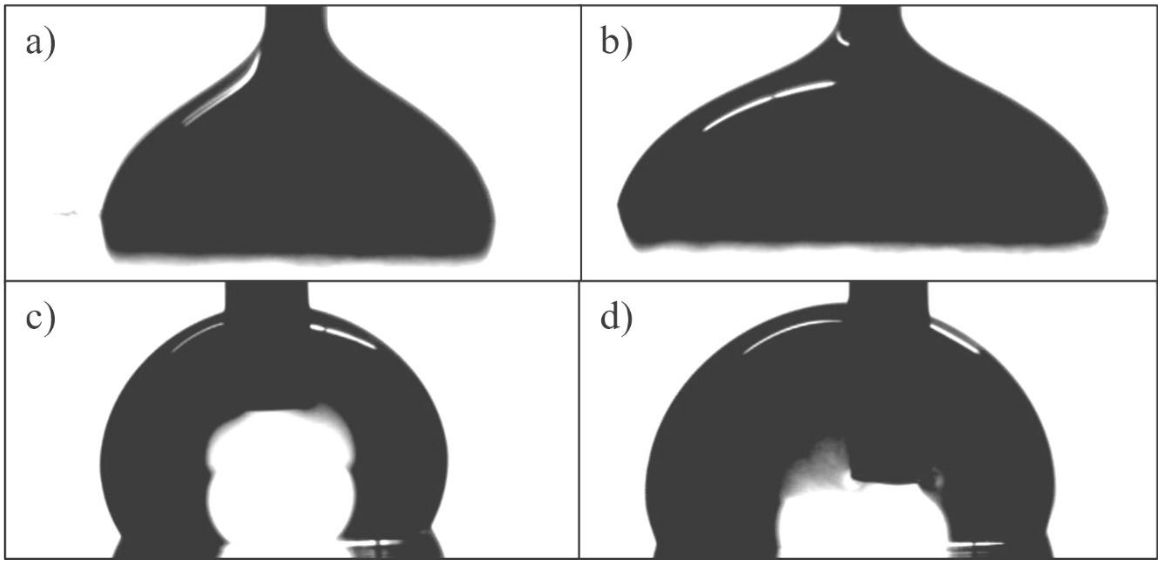

Figure 2-2. (a) Advancing and (b) receding contact angles of silver ink on Teflon-AF. (c) Advancing and (d) receding contact angles of DI water on Teflon-AF.

Table 2-1. Silver nanoparticle ink properties

Ink Property	**Value**
Surface tension (mN/m)	35
Viscosity (cps)	16.7
Density (g/mL)	1.38
Silver content (wt %)	31.7
Contact angle (°) on Teflon-AF	84±2
Contact angle (°) on dry silver	12±2

The anchor regions were positioned at a distance of d to each other. Due to geometry limitations in Surface Evolver, anchor regions were assumed to be flat circles flush with the printing surface. In this model, surface properties are applied to a flat substrate surface and the anchor thickness and its variations are not accounted for in the simulation environment as the thickness of the dried anchors is negligible compared with the thickness of the wet line segment. The radius *r* of the anchor regions was 39 µm. The perimeters of these circles are the parametric boundaries and are schematically shown in Figure 2-3.

As detailed in Ref [84], parametric boundaries are mathematical constrains applied to the geometry of the simulated body and are defined using equations and algorithms. The vertices that are positioned on the boundaries can only move on the 1D boundary paths and they do not participate in the surface minimization process. In the model, half of the vertices were placed on the perimeters of the anchors (fixed), with the other half placed on the top surface of the anchor hemispheres. The anchors were modeled as hemispheres, and the volume of the hemispheres was ignored in the calculation of the total liquid volume because it only represents 2.5% of the volume of a wet droplet. The parametric boundaries were imposed on the edges of the initial body to confine the body (printed ink) to the perimeters of the anchors. This method ensures that the contact angle of 0° can be preserved for anchors. Here is the first part of the code where first the perimeters of the circles are defined through formulas, and then parameter boundaries are imposed on them:

1. constraint display1 (the left circle in Figure 2-3)

   formula: sqrt((x)^2 + y^2 + (z_height)^2) = rad

2. constraint display2 (the right circle in Figure 2-3)

formula: sqrt((x-droplet_distance)^2 + y^2 + (z_height)^2) = rad

3. Boundary hemi_con1 Parameter1 (imposing the parametric boundary the left circle in Figure 2-3)

   x1: rad*cos(p1)

   x2: rad*sin(p1)

   x3: 0

4. Boundary hemi_con2 Parameter1 (imposing the parametric boundary the right circle in Figure 2-3)

   x1: rad*cos(p1) + droplet_distance

   x2: rad*sin(p1)

   x3: 0

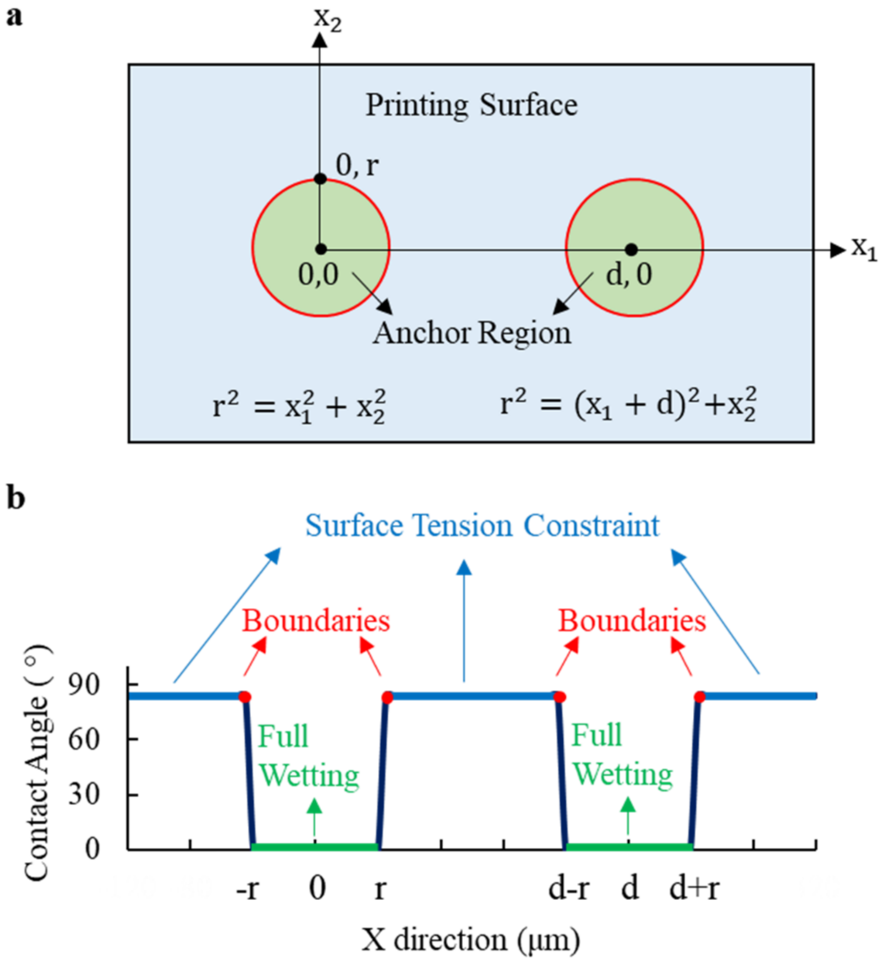

Figure 2-3. (a) Top view of the surface view in simulations. The circles represent the previously printed and dried silver drops, i.e., the anchor regions. (b) Local contact angle variation in the x-direction, with boundaries, full wetting, and surface tension constraint regions shown.

Figure 2-4a shows the initial body confined to the parametric boundaries at the perimeter of the anchors, and Figure 2-4b shows the same system without parametric boundaries. The volume of the anchor hemispheres shown in Figure 2-4 does not represent the real volume and it is simply used to hold the initial vertices on its surface. The simulated ink will only see the perimeters of the anchors and is not constrained by any other geometrical boundary. The body was defined as the volume encompassed by edges that connects vertices both on the perimeter and the top surface of the anchor hemispheres.

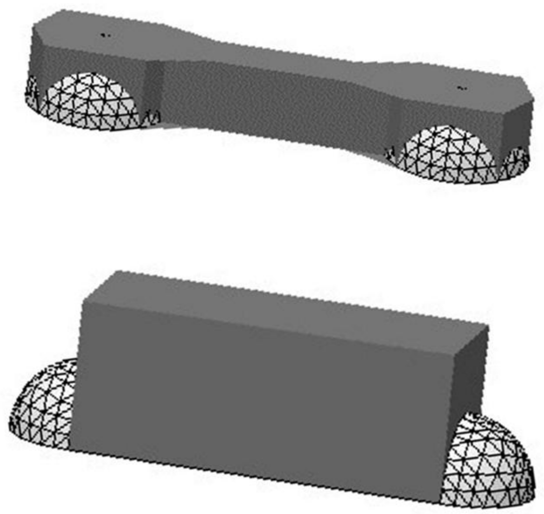

a

b

Figure 2-4. Initial defined body in Surface Evolver (a) with, and (b) without parametric boundaries imposed on its edges.

Another group of constrains defined in Ref [84] are 2D constraints, which are forces imposing restrictions on the body in two dimensions. The only 2D constraint used in this model is surface tension on the printing surface, see Figure 2-3. This 2D constraint is the foundation of the model in which the surface tension of the hydrophobic surface is included through Young's equation:

$$\cos(\theta) = \frac{\sigma_{sv} - \sigma_{sl}}{\sigma_{lv}} \qquad \text{2-3}$$

where σ_{sv}, σ_{sl}, and σ_{lv} are the solid-vapor, solid-liquid and liquid-vapor interfacial tensions. This constraint was exerted on the body facet that lies on the surface with low wettability.

In the code, first the contact angle of the ink on the surface is defined as input for the code to work. Next, the surface tension constraint is introduced with a keyword (here BOT). Then, after the faces are defined using the edge numbers, the constraint is applied on the face that is in touch with the surface. Here is the code:

1. parameter angle_bottom = 84 // contact angle between plane and surface
2. #define BOT (-cos(angle_bottom*pi/180)) // virtual surface tension of facet on plane
3. faces /* given by oriented edge loop */

   43 63 92 -77 -91 color cyan

   44 64 79 -78 -92 color cyan

   45 51 52 53 54 55 56 57 58 59 60 61 62 63 64 Tension BOT color cyan constraint 1

   46 65 66 67 68 69 70 71 72 73 74 75 76 77 78 color cyan

There are 16 facets in the initial ink body, but here only a few facets are given. Finally, the body is defined using the faces that make its boundaries with the surrounding environment, its volume and its density:

4. bodies /* one body, defined by its oriented faces */

   1 -31 -32 -33 -34 -35 -36 -37 -38 -39 -40 -41 -42 -43 -44 45 -46 volume ((37*200000) density 0.000000000000138

Here, 37 and 200000 are the number of printed droplets and the volume of an individual droplet, respectively. Since gravity effect is not taken into account as a constraint, the density value is not used in the calculations. At the end, the number and degree of iterations and refinements are added to the code.

The experimental methods (method 1 and 2) will be discussed in the next section. In the remaining chapter, using the simulation model described above, a correlation between experiment and simulation for inkjet-printed micro-patterns will be devised and demonstrated.

2.4. Droplet deposition on a surface with low wettability

Figure 2-5a shows the nozzle and the ejected droplet in the air. Figure 2-5b and c show single wet and dry droplets on the Teflon-AF surface; the initial volume of both were equal. The dry droplet has a radius of 18.6 µm (the diameter of a wet droplet on the Teflon-AF surface is ~71 µm), with an average thickness of 3.4 µm. The thickness profile of a single dry droplet is shown in Figure 2-5d. The thickness profiles of the dry droplets were measured using a stylus profilometer (Alpha-Step D-600, KLA-Tencor, USA). The dimple in Figure 2-5d is due to accumulation of material[86,87] on the edges of the droplet due to capillary flow[88].

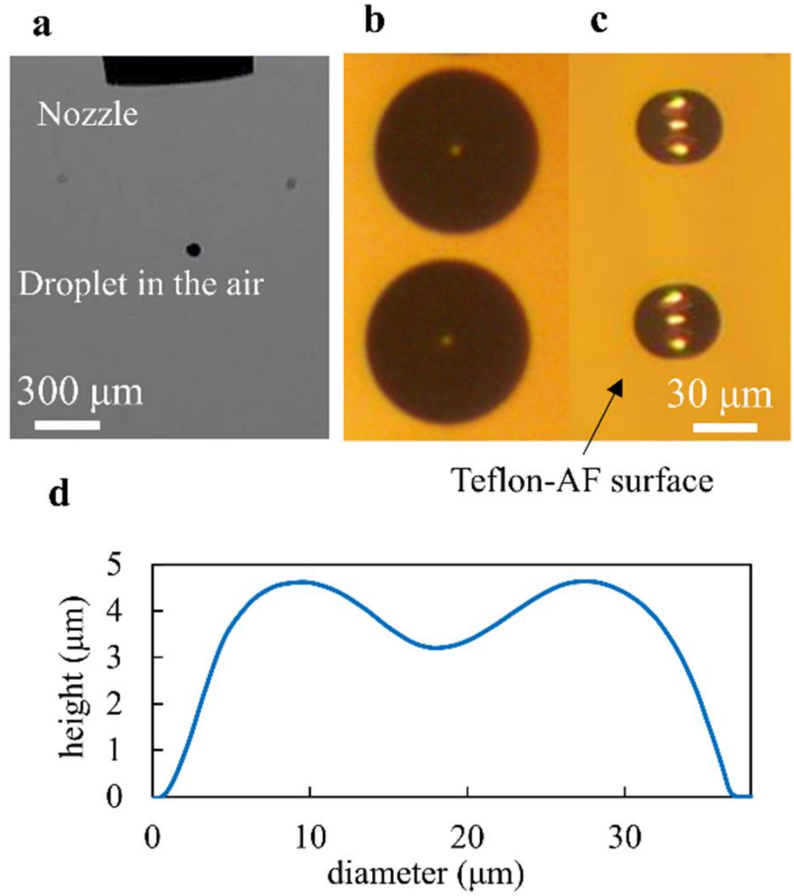

Figure 2-5. (a) A 60 µm-diameter inkjet nozzle and an ejected droplet in the air. Inkjet-printed single (b) wet, and (c) dry droplets on Teflon-AF surface. (d) Thickness profile of a single dry droplet.

When an ink droplet contracts or shrinks on a hydrophobic surface before complete drying, this phenomenon is often associated with the process of pinning. During inkjet printing, droplets are deposited onto the surface, and due to solvent evaporation, the droplet's outer edge advances inward. However, if the surface is hydrophobic, the contact angle remains high, preventing the ink from spreading out uniformly. As the solvent continues to evaporate, the ink undergoes a receding contact line behavior, where the liquid droplet's edges retract inward due to the force of surface tension and contact line pinning.[89] This pinning effect restricts the ink from spreading, resulting in a contracted, thicker center with receding edges, which influences the final morphology and density of the printed feature.

In the next two sections, two line formation methods will be discussed. The traditional approach involves adjusting droplet spacing to determine the line's formation, showcasing the challenges of forming continuous lines on a Teflon-AF surface. While smaller spacing results in droplet merging and irregularities, larger spacing leads to disjointed lines. This method emphasizes that altering the drop spacing won't resolve the challenge due to surface thermodynamics. Conversely, method 2 proposes a sequential printing and drying technique. Symmetric printing creates anchors at each line's ends, followed by printing the intermediate droplets. This method efficiently pins the ink on the surface, enabling the formation of line segments.

2.5. Method 1: Printing continuous lines on a surface with low wettability

Method 1 represents the traditional approach to form lines on a surface. With this method, a series of lines with varied drop spacing was printed with decrements of 5 µm. On a hydrophilic surface, an excessively small drop spacing results in lines that exhibit bulging, and an excessively large drop spacing leads to scalloping and discontinuities in the lines.[17,21] Figure 2-6a depicts a schematic of the inkjet printing process. On a hydrophobic surface, as can be seen in Figure 2-6b, when the drop spacing is small, every few droplets merge, and the number of the merging droplets decreases by increasing the drop spacing. In all panels in Figure 2-6b, the same number of droplets were printed (12). At a drop spacing of 75 µm, individual droplets appear. Beyond a drop spacing of 80 µm, the individual printed droplets no longer merge with one another. This experiment serves to affirm that the Teflon-AF surface exhibits a non-wetting behavior for this silver nanoparticle ink, pointing to the challenge that was discussed earlier to form a continuous line through adjustment of the drop spacing. Changing the volume of printed droplets will not remedy the issue due to the same surface thermodynamic principle that governs this phenomenon.

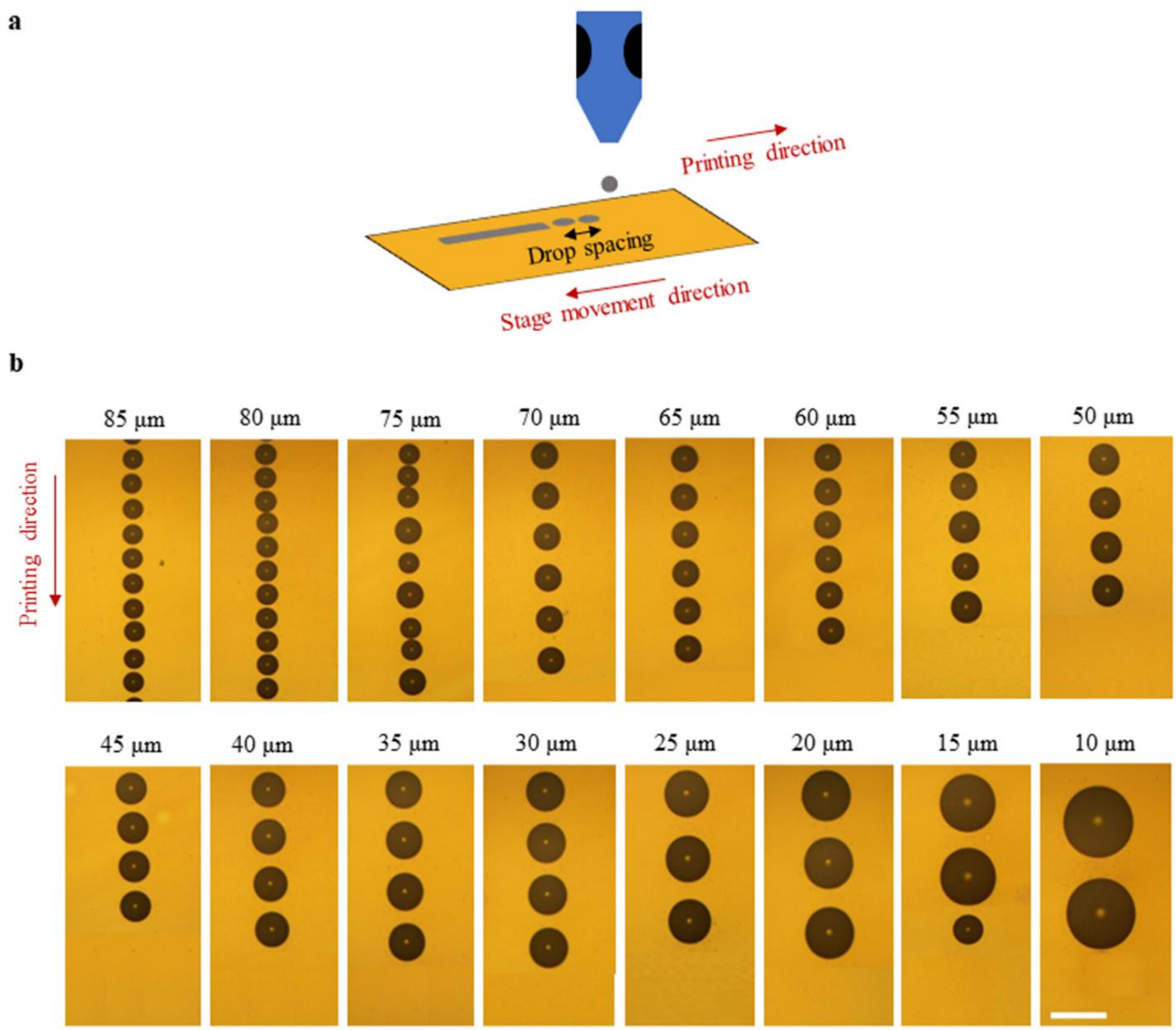

Figure 2-6. (a) Schematic of the inkjet printing process. (b) Inkjet-printed silver nanoparticle lines with different drop spacing on the Teflon-AF surface. The drop spacing for each image is shown on top of the image. The scale bar represents 200 μm. The volume of a drop in the air is $0.19\ nL$.

2.6. Method 2: Sequential printing and drying

Method 2 is the strategy proposed here. It was employed to print line segments on a surface with low wettability. Method 2 is a symmetric printing method, where anchors at the two ends of the line segments are printed first, and the middle droplets are printed last. To pin the ink on the surface, the first sequence of droplets was dried before printing the second sequence in the middle. Figure 2-7 shows the process. First, two anchors with a distance of 200 µm were printed and dried (Figure 2-7a). Each wet anchor has the volume of 1.93 nL (10 single printed droplets). Subsequently, ink volumes of 1.8 nL to 6.4 nL were printed between anchor regions, and dried (see Figure 2-7b-e). It can be observed from Figure 2-7 that varying the volume of the printed droplets in between the anchors changes the shape of the line segments. As the ink volume is gradually increased, the width of the line segments increases accordingly. When the volume of the printed droplets is insufficient, the connection is hardly formed after drying (Figure 2-7b). As the volume is increased, the connection widens, but it remains thinner than the anchor diameter (Figure 2-7c). At a specific volume for a given line segment length, the dry line width approaches the anchor diameter (Figure 2-7d), resulting in a smooth line after drying. However, further increasing the ink volume results in a line segment width larger than the anchor diameter (Figure 2-7e), which is generally not desirable. Considering the above, the strategy suggested in this study works for printing lines. Longer lines can be generated by repeating this process; even corners can be formed by positioning the next dry anchor not along the initial line, but at a desired orientation.

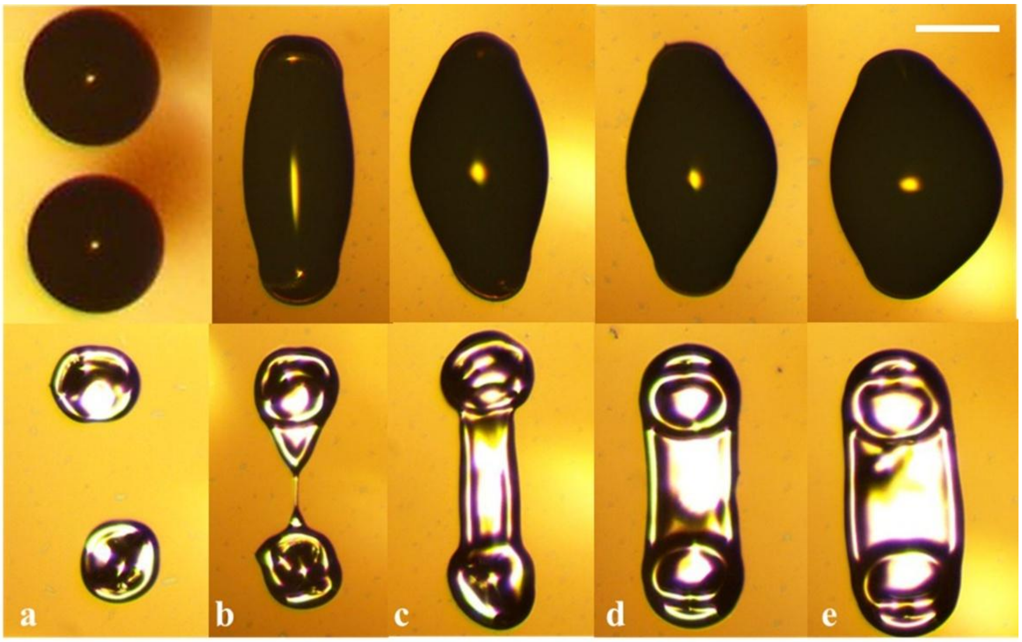

Figure 2-7. Optical images of line segments printed with method 2 in the wet (top row) and dry (bottom row) state. (a) Step one to form the anchor regions. Subsequently printed ink between anchor regions with ink volume of (b) 1.8 nL, (c) 3.6 nL, (d) 5 nL, and (e) 6.4 nL. The scale bar represents 100 µm. The droplet separation distance is 200 µm. In each column, the top row shows the line segments before drying, and the bottom row shows the same line segments after drying (at 150 °C for 15 minutes).

Figure 2-8 shows the drying process of a line segment with an anchor distance of 200 µm while stage temperature increases from 22 °C to 150 °C.

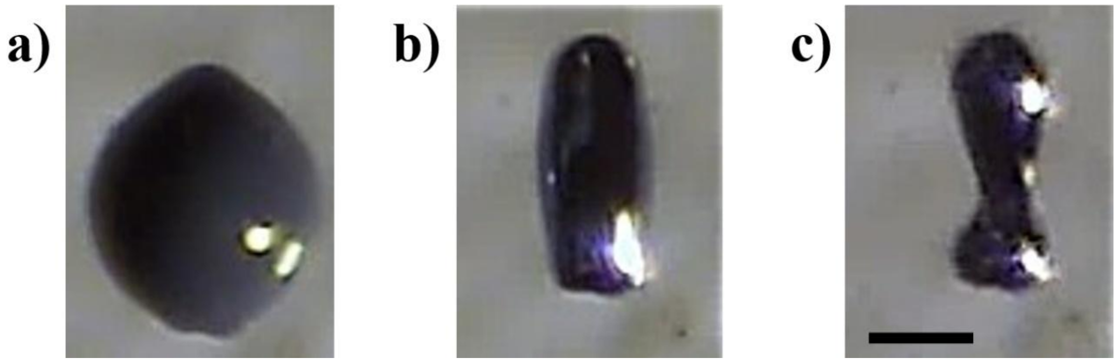

Figure 2-8. The drying process of a line segment with an anchor distance of 200 µm while stage temperature increases from (a) 22 °C, to (b) 57 °C, and to (c) 150 °C. Scale bar represents 100 µm.

2.7. Simulating the sequential printing and drying process

To minimize experimentation to produce printed lines with different characteristics and explore patterns other than a line, the wet patterns were simulated. Figure 2-9a and b show the experimental and simulated line segments before drying with the anchor distance of 200 µm for different ink volumes of 1.2, 3.2, and 5.0 nL. Figure 2-9c shows the graph of the midpoint for wet line width versus the printed volume for the same anchor distance; the objective is to attain a smooth line, so the width of the midpoint for the line was used as the point of comparison, the midpoint of the line was selected since it shows the most deviation from a straight line that is the goal of the work. Figure 2-9 shows an excellent agreement between experiment and simulation with an average error of 1.1%.

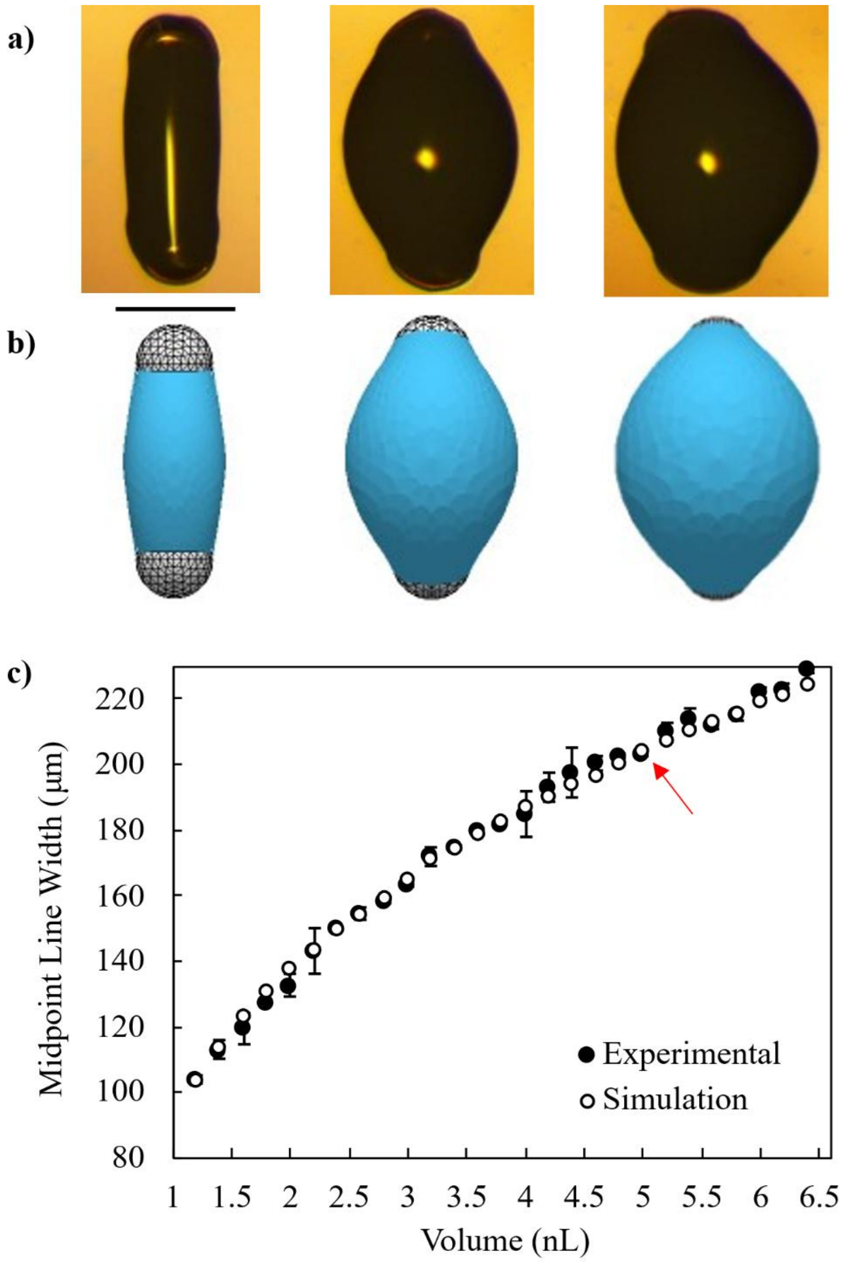

Figure 2-9. (a) Experimental printed, and (b) simulated line segments with the anchor distance of 200 µm for volumes of 1.2, 3.2 and 5.0 nL from left to right. The scale bar is 100 µm. (c) Graph of wet midpoint line width versus printed ink volume showing good agreement between experiment and simulation. The red arrow marks the volume of ink which results in a final smooth dry line segment.

The distance between the two anchors was varied in both experiments and simulations. The results for the anchor distances of 170 µm, 230 µm and 260 µm are shown in Figure 2-10. Optical images of both the inkjet-printed lines and their simulated counterparts are presented, offering a visual confirmation of the consistency between the real and modeled results. The inkjet-printed experimental and simulated data are very close to each other and follow the same trend. This trend could relate to the shape and width of the line segments or the degree of discontinuity within the printed lines. The close match between the experimental and simulation results implies that the primary forces at play are well-characterized by the inputs to the simulation, with the contact angle being a significant factor. The optical images of the inkjet-printed and simulated line segments for the volume of 5.6 nL for different lengths are also presented in Figure 2-10. Understanding how different anchor distances affect the final printed line profile is crucial for precision printing, where exact dimensions are necessary for functionality, such as in microscale transistors or sensors.

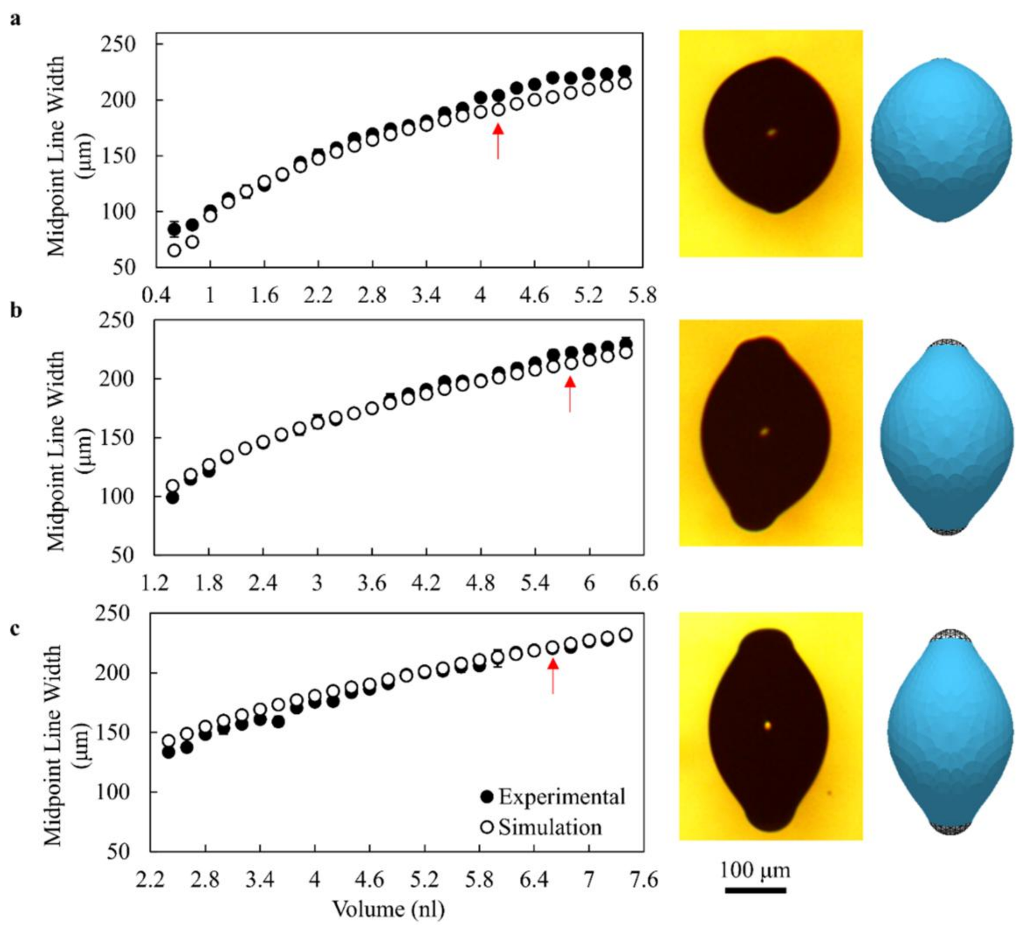

Figure 2-10. From left to right, graphs of the midpoint linewidth versus printed ink volume, top view images of printed and simulated line segments for an anchor distance of (a) 170 µm, (b) 230 µm, and (c) 260 µm. Red arrows point to a volume that results in a straight dry line in each case. The images of line segment are all for the volume of 5.6 nL.

Parametric boundaries were used on the perimeter of the anchors where the wettability abruptly changes from one region to the other, to avoid discontinuities in the gradient descent method. Defining parametric boundaries at the location of discontinuities allows us to remove the discontinuous coordinates from the energy minimization integral by fixing them in place. The implementation of surface tension via the contact angle ($T\vec{k}.\overrightarrow{dA} = T\cos\theta.dA$) as a 2D constraint leads to simulation results that fit the results obtained from printed patterns. As confirmed by this model, the formation of microdroplets with the sequential drying method is mainly governed by the surface energy of the substrate. Factors such as gravity, pinning, and drop impact do not significantly influence the equilibrium state of micro-patterns obtained through the sequential drying method, as these phenomena are not included in the model.

Understanding the surface tension forces that lead to the minimal energy state allows us to understand the final ink shape. Without the anchors, the wet ink makes a contact angle of ~90º with the surface and becomes a hemisphere instead of a line to minimize surface energy. As there is no pinning, no stable line can be formed. Increasing ink volume only adds to the hemisphere's radius. The anchors add two areas where pinning of contact line occurs allowing for formation of a line. Due to the high surface energy of the dried silver anchors, surface energy is minimized when the wet ink fully wets the anchors. This constraint allows a line to be formed rather than a hemisphere. The positioning of the ink exactly in the mid-point of the anchors leads them to be equally covered by wet ink. Therefore, a bridge of ink forms between the anchors, which increases in width with increasing ink volume as seen in Figure 2-7.

If we plot the ink volume versus the anchor distance which leads to a straight line with smooth edges (From Figure 2-9 and Figure 2-10), a line with constant slope can be found (see Figure 2-11); the error bars show an error margin of one droplet (0.2 nL). Such behavior suggests that a print factor (PF) exists which correlates the required printed volume to the anchor distance (d), i.e.:

$$Vol_{wet} = d \times PF \qquad 2\text{-}4$$

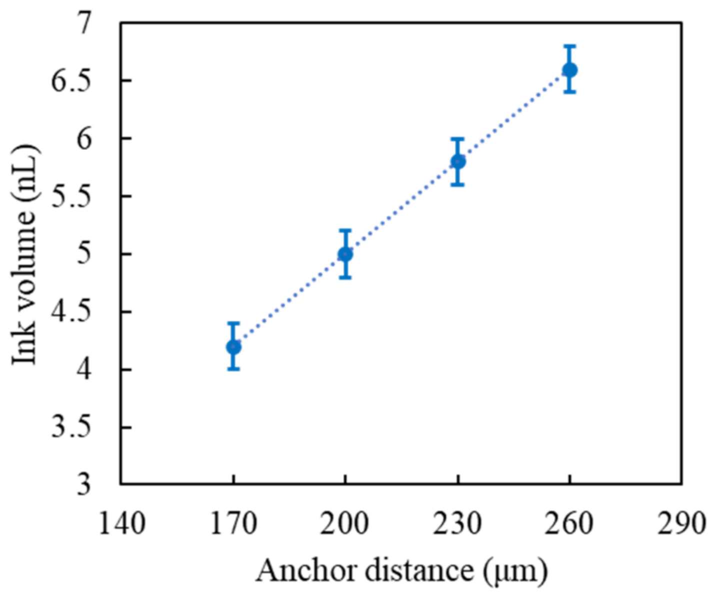

Figure 2-11. The ink volume needed to produce a smooth line segment versus line segment length. The graph shows a linear relationship between the Vol_{wet} and anchor distance and its linear fit. The slope of the linear fit is $2.7 \times 10^4\ \mu m^2$(with y-intercept, standard error and R^2 being equal to -0.3 nL, 5.2×10^{-18} nL and 1.00, respectively). The error bars show error margin of one droplet (0.2 nL).

PF serves as a metric that, once determined from an initial experiment involving the printing of a line of specific length, can be applied to predict the behavior of ink for printing lines of different lengths. This factor is essentially a bridge between the experimental data and the predictive models, capturing the essence of the ink’s flow, wetting, and drying behavior on a given substrate.

The significance of PF lies in its ability to infer the relationship between the volume of the ink deposited and the final width of the line post-drying. If the PF is consistent across various line lengths, then one can conclude that the ink's spread on the substrate and the subsequent drying follows a predictable pattern. This predictability is crucial for applications where precise line dimensions are necessary for the correct functioning of the printed circuits.

For instance, when a specific line length and ink volume result in a successful print with the desired line width and uniformity, the PF derived from this print can be used to calculate the volume of ink needed for a different line length aiming to achieve a similar print quality. This application of PF means that once the factor is determined experimentally for a particular set of conditions, it can streamline the printing process for new patterns without the need for extensive trial and error.

This will be further explained below, but before that in Figure 2-12 we show that this method of printing can be utilized for printing other features such as triangles using three-anchor patterns. Using method 2, equilateral triangles were inkjet-printed and compared with the simulation results. The top view optical images of the inkjet-printed experimental and simulated triangles and the graphs of the image area versus printed ink volume are shown in Figure 2-12. This comparison underscores the robustness of the model since it can adapt to more complex shapes beyond straight lines, which are more common in printed electronic circuits.

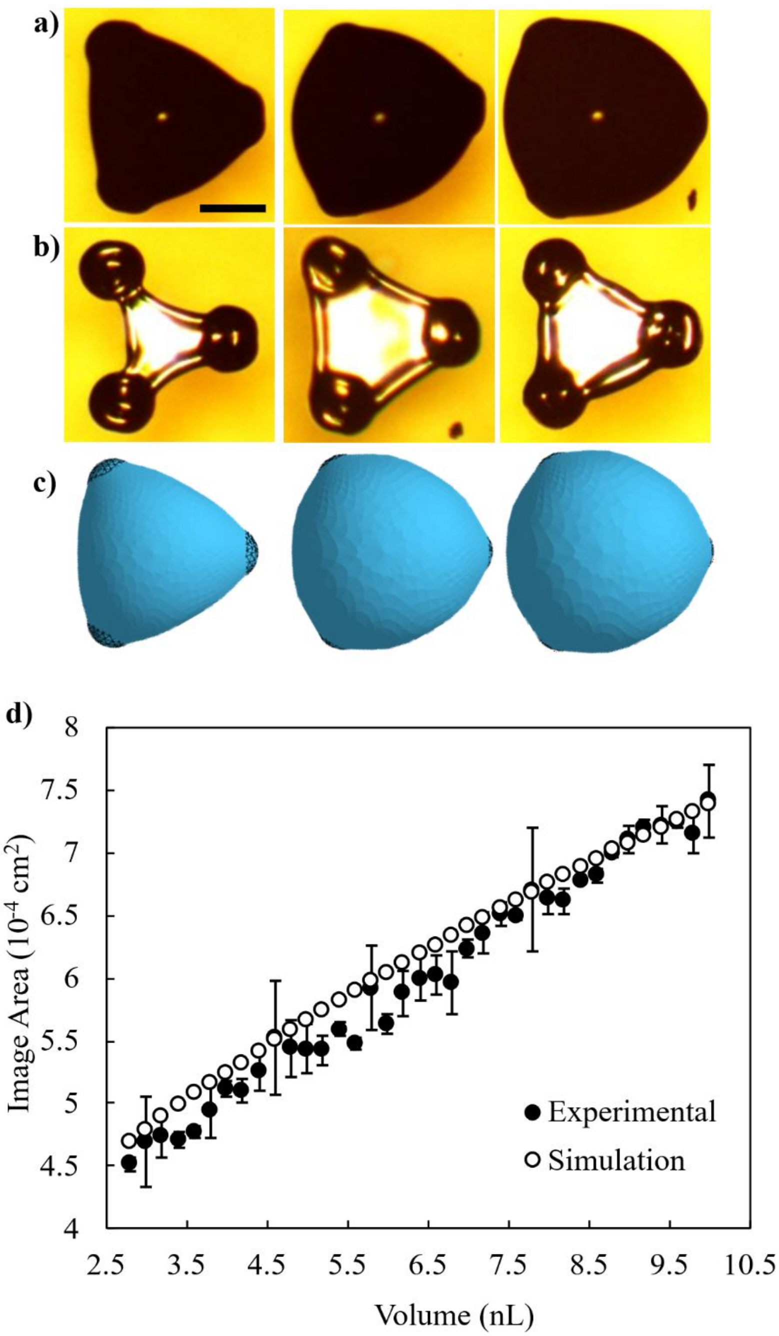

Figure 2-12. Optical images of (a) wet and (b) dry printed, and (c) simulated equilateral triangles (side dimension = 200 μm), with ink volumes of 5.2 nL, 8.8 nL, and 9.8 nL from left to right. The scale bar represents 100 μm. (d) The simulated and inkjet-printed image area versus ink volume with a percentage error of 2.9%.

To demonstrate the second implication of Figure 2-11 is to predict the final ink pattern using the simulations. Therefore, first we need to consider the drying process of the ink, i.e. the removal of the solvent and having only the solute (silver nanoparticles) left behind. The fact that we can predict the final ink pattern only considering surface energy minimization means that the dynamics of the drying process do not significantly affect the final equilibrium state. The drying of the ink where the contact line recedes and the final line shape is achieved is much slower, i.e., in the order of minutes compared to spreading – under a second. The drying process will determine feature dimension, which is of great importance in microelectronics since it affects the electrical properties. The simulations can be used to predict the dry shape and, in particular, the printed volume required to form straight smooth features on hydrophobic surfaces. The linewidth versus volume for all the four tested anchor distances in Figure 2-9 and Figure 2-10 can be fit to a square root function:

$$w = A\sqrt{V} \qquad \text{2-5}$$

where w is the line width, V is the printed volume or V_{wet}, and A is a fitting parameter. There are two distinct phases in the drying process of a droplet (or a pattern in general) on a surface with low contact angle hysteresis. The schematic drawing in Figure 2-13 shows the drying process of a droplet, starting from an initial wet droplet with the diameter of w_{wet}. In the first phase, as the droplet dries, the contact line recedes without being pinned to the surface due to the low wettability of the surface, while the contact angle stays fixed. Therefore, the droplet maintains the shape of a spherical cap. The volume of a spherical cap is proportional to the cube of its radius (r^3). The onset of the second phase is when the droplet becomes pinned. The simulations are based on energy minimization of the liquid surface and hold only for phase one. In phase one, the droplet is regarded as a spherical cap, so for the volume ratio between the pinned and wet state, we will have the following value based on the measured drop radii for this ink on Teflon-AF:

$$\mathrm{vol\%} = \frac{V_{pin}}{V_{wet}} = \left(\frac{r_{pin}}{r_{wet}}\right)^3 = \left(\frac{18.6}{35.5}\right)^3 \qquad 2\text{-}6$$

$$= 14.38\%$$

In phase two, the concentration and viscosity of the ink has increased sufficiently to inhibit the contact line from further movement, and the droplet contact angle starts to reduce. When pinning starts, the cord length (or contact length) in Figure 2-13 is w_{pin} (which is assumed to be equal to w_{dry}). Substituting w_{pin} in equation (2-5), leads to a value for V_{pin} and using the volume ratio in equation (2-6), V_{wet} can be calculated. We assume that the same relationships and assumptions hold for lines and other features, too, which was validated for lines and triangles. The V_{wet} value that results in smooth line segments (linewidth equal to anchor diameter) was measured for four different anchor distances. Figure 2-14a-d show the wet and smooth dry line segments for anchor distances of 170, 200, 230, and 260 mm, respectively. The plot in Figure 2-14e shows values for the printed volume needed to create smooth line segments versus the anchor distance for the experimental and simulation results.

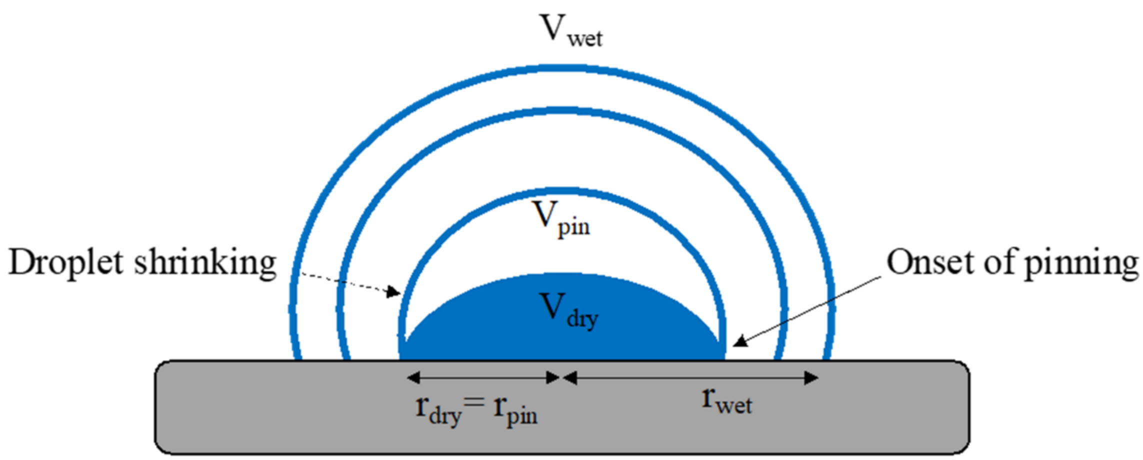

Figure 2-13. The drying process of a droplet, starting from an initial wet droplet with the diameter of w_{wet} until its diameter reaches w_{pin} in phase one. In phase two, the contact line is pinned as the drop volume is reduced to V_{dry}.

The values predicted from the simulation are close to the experimental results with an average absolute error of 10.7%. The same method was used to predict the area of triangles printed with different ink volumes and shows a good match with experiment with an average absolute error of 22.2%. The larger error for triangles is likely due to their more complicated shape having three anchors and three edges with complications arising from their pinning process.

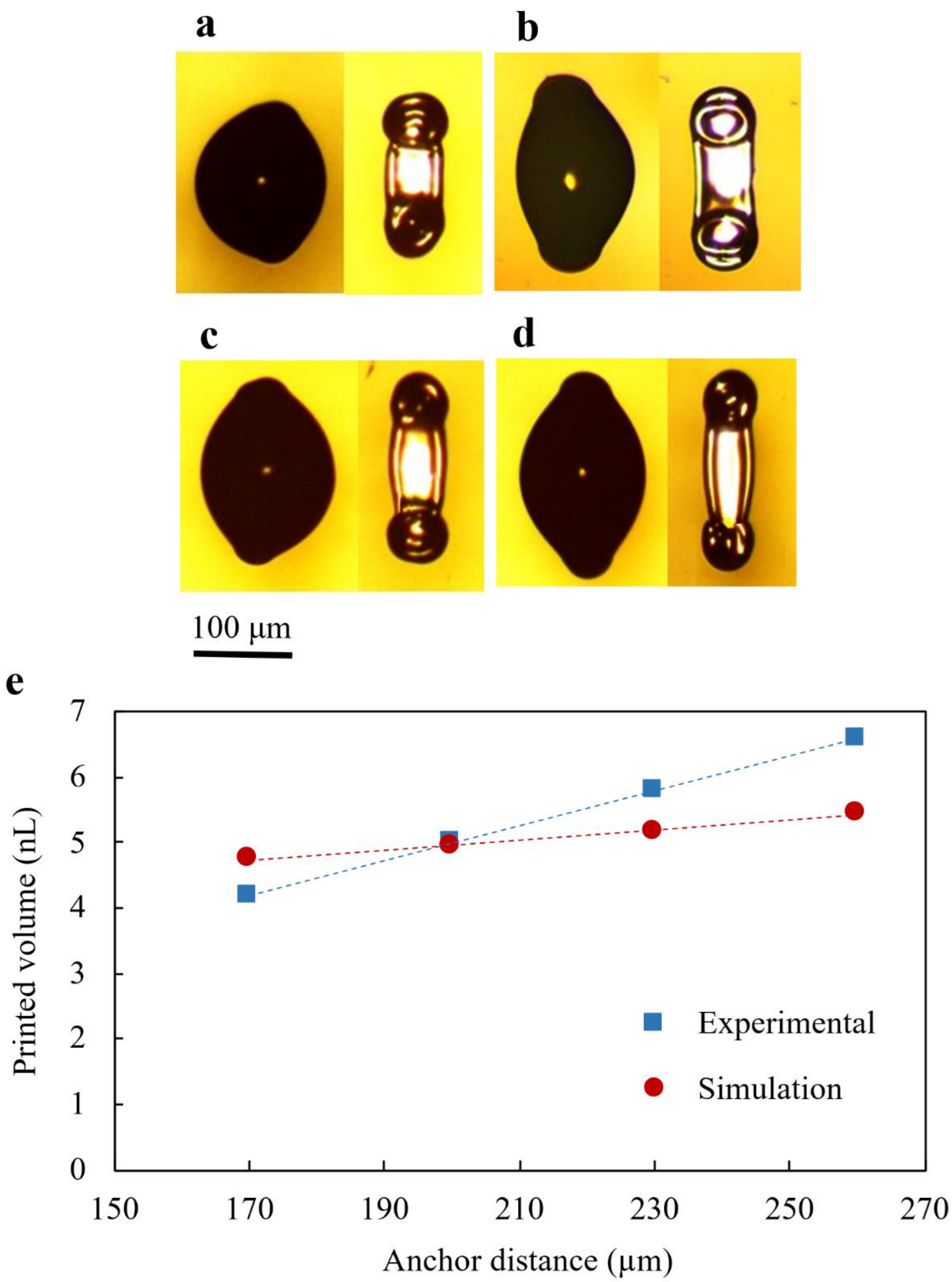

Figure 2-14. Images of smooth line segments in the wet and dry state for anchor distances of (a) 170, (b) 200, (c) 230, and (d) 260 mm, respectively. (e) The printed volume needed to print a smooth dry line segment versus the anchor distance for the experimental and simulation results.

2.8. Conclusions

In this chapter, a new printing method is shown to form micro-patterns on surfaces with low wettability that does not require surface modification. A model based on energy minimization predicts the shape of the inkjet-printed micro-patterns with good accuracy and only the contact angle of the ink on the surface as the input, confirming that the formation and equilibrium state of these micro-patterns are mainly governed by surface tension forces. Line segments with different length were printed and simulated. Both the experimental and simulation methods are extended to more complicated shapes such as triangles. Moreover, the energy minimization based simulations were used to predict the required printed ink to produce smooth dry features, which show good agreement with experimental results. The computational simulations that incorporate the PF provide a powerful tool for predicting the end result of the printing process. By inputting the contact angle of the ink on the substrate and the desired pattern dimensions into the simulation, it becomes possible to accurately forecast the outcome, thus reducing material waste and increasing the efficiency of the production process.

In the next chapter, another approach to realize inkjet printing on hydrophobic surfaces will be presented.

Chapter 3: Inkjet-printing on hydrophobic surfaces with the implementation of stacked-coin strategy

This chapter was published in Advanced Engineering Materials Journal, Copyright Wiley.

Docherty, M.J., Naderi, P., Grau, G., Sefiane, K. and Amirfazli, A. (2024), Inkjet Printing on Hydrophobic Surface: Practical Implementation of Stacked Coin Strategy. Adv. Eng. Mater., 26: 2400237. https://doi.org/10.1002/adem.202400237

3.1. Introduction

In this chapter, another method to overcome the difficulties of inkjet printing on hydrophobic substrates through stage heating is discussed. The method is an adaptation of stacked-coin printing, a technique which has been successfully used in the production of conductive lines on hydrophilic surfaces in thin-film transistors[90] and conductive films[91]. Stacked-coin printing is a technique in which the time taken to deposit a subsequent overlapping droplet in a pattern is longer than the evaporation time of the prior droplet.[21] Figure 3-1 shows how increasing the stage temperature results in droplet pinning on the surface and eventually, stacked-coin morphology. By introducing a heated stage, the drying kinetics of the droplet are altered. The temperature of the stage is controlled to enhance the evaporation rate of the solvent in the ink.

Conductive inks composed of silver nanoparticles and a solvent are commonly used in the printed electronics industry. When dried, due to the silver content, the ink becomes hydrophilic. Taking advantage of the hydrophilic nature, we showed in the previous chapter that wet ink can be anchored to a dried ink region[92]. The effect of impacting droplets experiencing a wettability gradient between the low surface energy substrate and the hydrophilic attraction to the previously dried hydrophilic droplet prevents the application of the stacked-coin technique at room temperature (Figure 3-1b). The drying time of the droplet at room temperature supersedes the time taken for a wet droplet to completely overlap the previous dried droplet in the system. Through manipulation of this situation, by accelerating the rate of drying of the ink through stage heating, we can adapt the stacked-coin method for use on hydrophobic surfaces (Figure 3-1c and d). The work in this chapter defines the window for successful printability by introducing and relating key parameters of droplet spacing, stage temperature and stage movement speed.

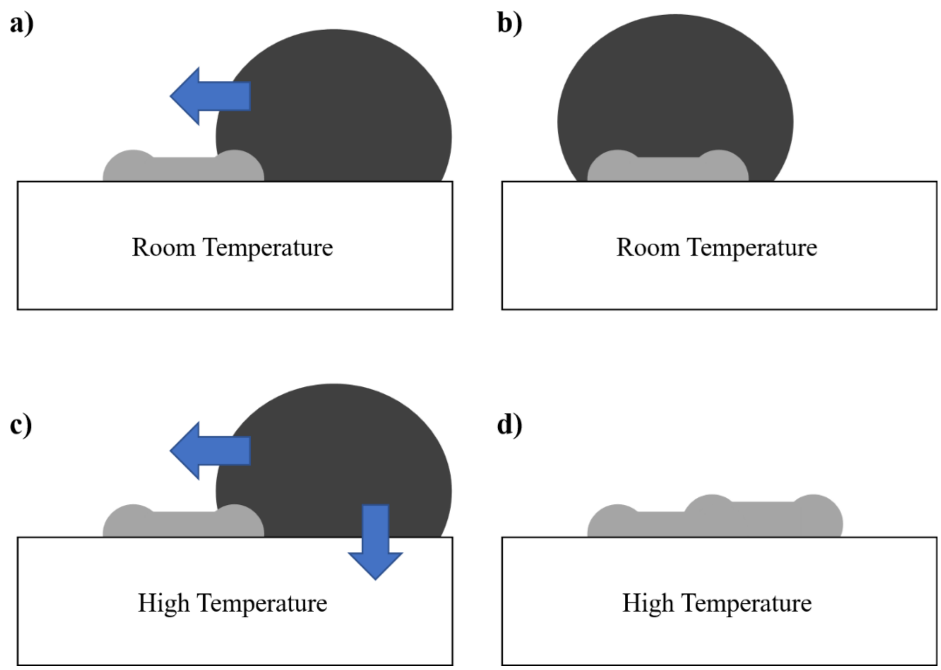

Figure 3-1. (a) Wet droplet is printed slightly overlapping a dry droplet. (b) Due to low surface wettability, wet droplet covers the dry droplet. (c) Wet droplet is printed slightly overlapping a dry droplet on a heated stage. (d) Wet droplet dries on the stage with an overlap on the previous droplet.

3.2. Substrate preparation and printing process

This work was done with a custom-built inkjet printer with an accuracy of 1.4 µm as will be demonstrated in subchapter 5.2.4. The stage was programmed to come to a complete stop in order to jet the droplet before moving to the subsequent position, limiting stage speed based on both drop spacing and the maximum acceleration of 256,000 µm/s. The printer was operated in a drop-on-demand (DOD) mode with a Microfab 60 µm orifice nozzle (MJ-ATP-01-60-8MX, Microfab Technologies, Inc. Plano,TX), controlling precise droplet ejection through a piezoelectric transducer. The specific piezoelectric waveform was: 0 V idle voltage, 30 V dwell voltage, -30 V echo voltage, dwell time of 20 µs, echo dwell time of 40 µs and all rise and fall times at 6 µs. Droplet ejection speed was typically 1-2 m/s, droplets are approximately 0.2 nL in volume at ejection.

The ink that was used for experimentation was a silver nanoparticle ink (Anapro, DGP 40LT-15C), with 30-35% by weight nanoparticle silver suspended in triethylene glycol monoethyl ether (TGME) solvent. With the surface tension, viscosity and density of the ink being 34.65 mN/m, 13.7 cP, and 1450 kg/m^3, respectively. The substrate used was Teflon-AF 1600 (Sigma-Aldrich, Oakville, Canada) coated glass microscope slides. Coating of microscope glass slides by Teflon-AF was achieved through spin coating at 500 rpm for 60 seconds. Teflon-AF solution was annealed at 150 ºC for 30 minutes before being translated over to the printer. The contact angle of the ink on the substrate surface was measured to be 84º. Despite the ink contact angle being < 90º, the system still exhibits significant hydrophobic tendencies as discussed in the previous chapter ; thus, the system is considered hydrophobic. The substrate preparation and inkjet printing process are shown schematically in Figure 3-2.

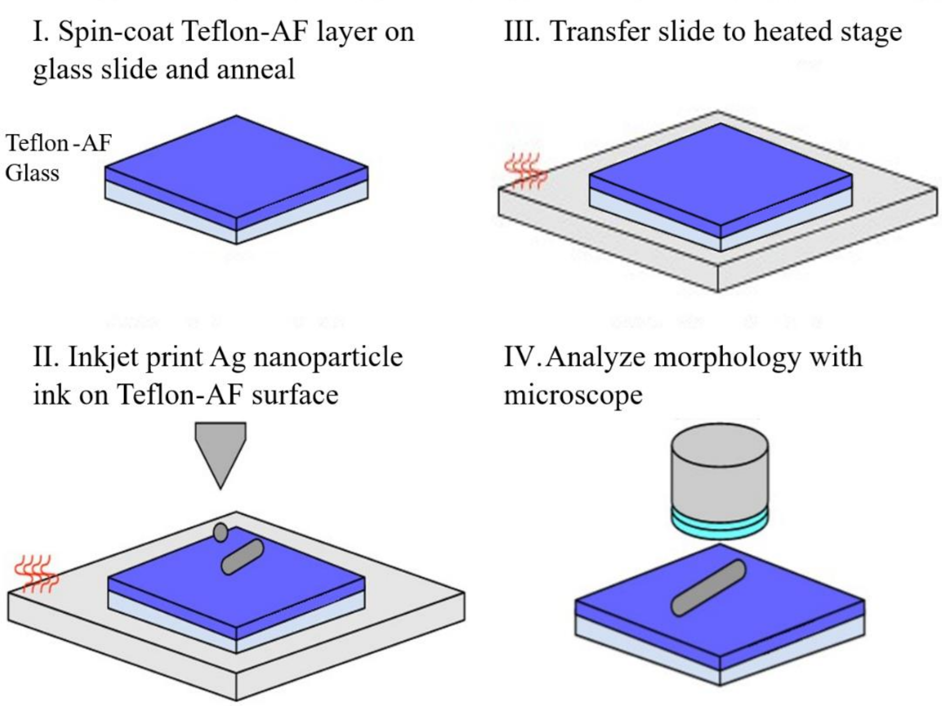

Figure 3-2. Schematics of the substrate preparation and inkjet printing process.

The independent variables used in this investigation were substrate/stage temperature (150-180 ºC), drop spacing (5-30 µm) and stage movement speed. The choice of high range of temperatures here is due to the hydrophobic nature of the substrate, since the drying time of impacting droplets is a crucial factor to consider for the success of this proposed method. Temperatures close to the sintering temperature of the silver ink recommended by the manufacturer were initially investigated and proved as an optimal starting point for investigation. Stage movement speed was varied from 5 µm/s to the maximum speed which can be achieved, limited by stage acceleration for the specific drop spacing investigated. On a fundamental level, these three variables (stage temperature, printing speed and drop spacing) have been proven to affect printed line morphology in tandem, being the fundamental three effective factors that can be directly controlled within our setup. To minimize ink evaporation within the nozzle and ensure smooth production and testing of lines, the nozzle was held approximately 1-2 cm from the substrate surface. Upon nozzle clogging, the nozzle was forward-flushed with iso-propanol (IPA) in a sonication chamber, then backflushed with IPA heated to 80 ºC. Substrate roughness, ink concentration and atmospheric pressure were assumed constant throughout printing. Additionally, it is assumed that the substrate can be considered flat, with optical profilometry data showing minimal variations in the order of 10-100 nm as seen in Figure 3-3.

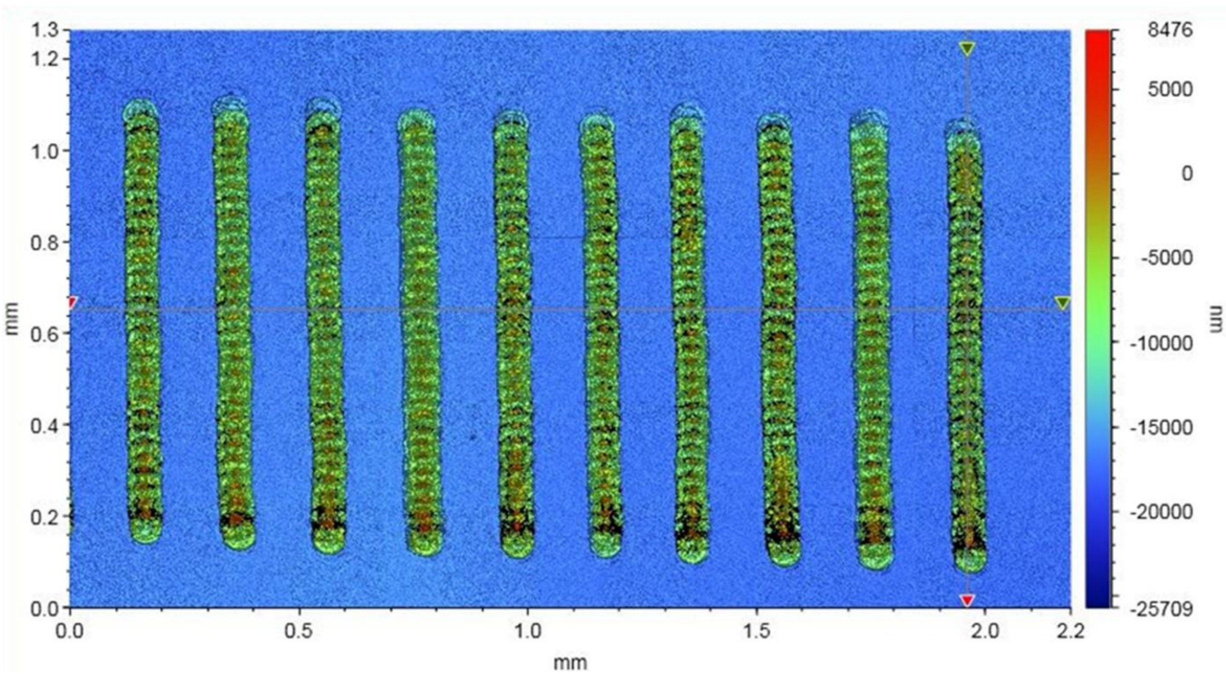

Figure 3-3. Optical profilometry example with group of 10 μm drop spacing lines.

3.3. Inkjet-printed stacked-coin line regimes

The printed lines can be categorized into several uniquely identified regimes. The identified regimes are isolated droplets, isolated groupings, broken line, true stacked-coin, and delamination. Examples of the expected morphologies present within each of these regimes are shown in Figure

3-4. Through the observation of dried ink patterns, the mechanisms which yield specific ink morphologies can be identified. These mechanisms indicate distinct changes in printability, which reflect the onset of successful line formation. Each independent variable is investigated to determine a corresponding limiting condition, e.g., instantaneous drying temperature, maximum achievable drop spacing, and onset of asymmetric droplet spreading, all of which will be touched upon later.

The isolated droplet regime is largely a temperature dependent regime (Figure 3-4a). This regime occurs when the drying time of the droplets is substantially longer than the dewetting time and droplet spacing is relatively high. Overlapping wet droplets on the surface do not dry quickly enough to prevent them from completely dewetting and drying on the previous droplet. This is due to the wettability gradient caused by the overlap of the wet droplet onto both the previously dried hydrophilic droplet and the hydrophobic substrate. This regime leaves large, isolated droplet profiles at regular intervals which is akin to the expected result when printing lines on hydrophobic surfaces at room temperature as discussed in the previous chapter; the temperature of the surface has not yet reached a state in which it can affect line morphology. This is similar to isolated droplet regimes identified for hydrophilic surfaces. In this study, the isolated droplet regime was seen for any drop spacings greater than approximately 70 µm. Figure 3-5 shows regime windows which are governed by the three interdependent factors: drop spacing, speed, and stage temperature.

The isolated grouping regime is similar to that of the isolated droplet regime (Figure 3-4b); however, the morphology of droplet groups begins to take a more ovular shape as regularly occurring groups of droplets can be observed, showing the onset of an instantaneous drying condition. While wet droplets are still affected by the wettability gradient, complete overlap onto the previous droplet is not achieved before drying. This results in an offset of the droplet to be sintered on the substrate surface. This can be seen by the repeatability of enlarged groups of droplets and their spacings remaining consistent. This predictability in the size of droplet groups indicates the specific shift of each droplet in a grouping until natural group separation occurs. The predictably regular spacings and sizes of the groupings indicates that droplet behavior is predictable and is not subject to small fluctuations or errors in printing conditions. Therefore, this is identified as a separate regime from isolated droplets. The onset of this condition is heavily dependent on droplet spacing, substrate temperature and stage speed/deposition frequency as these variables must operate efficiently in tandem to overcome wettability gradients. For a constant temperature, reducing the drop spacing or increasing the speed, leads to the transition from isolated droplets to isolated grouping regime. At a constant drop spacing, increasing both the temperature and the speed helps with the transition. And finally, at a constant speed, reducing the drop spacing and increasing the temperature will lead to the formation of isolated groupings.

The broken line regime exists as a transitional regime between isolated groupings and true stacked-coin morphology (Figure 3-4c). Droplet groupings begin displaying unpredictable behavior, with groupings of unstable lengths beginning to occur at various intervals. Within this regime, full stacked-coin lines up to 1000 μm can be produced; however, when repeating the test conditions, a different pattern of groupings is observed. This morphology can exist within conditions where the overlap, drying time and deposition rate are sensitive to system hardware and software fluctuations which can cause a line breakage, thus these regions are not identified as printable regions for true stacked-coin morphology. The presence of this regime can indicate onset conditions of stacked-coin regime.

True stacked-coin regime indicates printing conditions which yield continuous lines with stacked-coin morphology (Figure 3-4d). This is the ideal printing regime, and this study aims to discover the conditions necessary for a variety of speeds, drop spacings and substrate temperatures for which stacked-coin regimes can be achieved. Figure 3-5 maps the situations where stacked coins can be produced at different stage temperature, with varying stage speed, and drop spacing. As is evident from Figure 3-5e, increasing stage temperature expands the printability window for stacked-coin morphology; however, in microfabrication lower processing temperature is preferable. Figure 3-5a shows the occurrence of stacked-coin lines at lower temperature, but the printing speed is very low. Figure 3-5b demonstrates slightly higher temperature and very high printing speed, but the drop spacing is low which means higher volume of ink per line length. Figure 3-5c and d comprise of larger printability windows for stacked-coin lines where a wider range of speed and drop spacing is possible.

The delamination regime is the smallest identified regime occurring exclusively at low drop spacings and low stage speed and high stage temperatures (Figure 3-4e and Figure 3-5c-e). Delamination refers to printed lines partially depinning from the surface. Partial delamination is the result of tensive forces across the thickness of the line during printing, where the tail of the delaminated line begins to rise off the surface. Partial delamination occurs naturally before being transitioned into full delamination. Full delamination has also been observed on the lines. While partial delamination has been observed to correct itself and stop delaminating, the surface does not recover from full delamination once it has started. A similar phenomenon with the curling up of inkjet-printed lines has been reported,[93] with the root cause being a product of the built-up stress gradient within the silver nanoparticle ink due to the rapid drying and high stage temperature experienced by the lines. The presence of the delamination phenomenon indicates a region where true stacked-coin lines cannot be reliably produced. Full and partial delamination are shown in Figure 3-4e, i and ii, respectively.

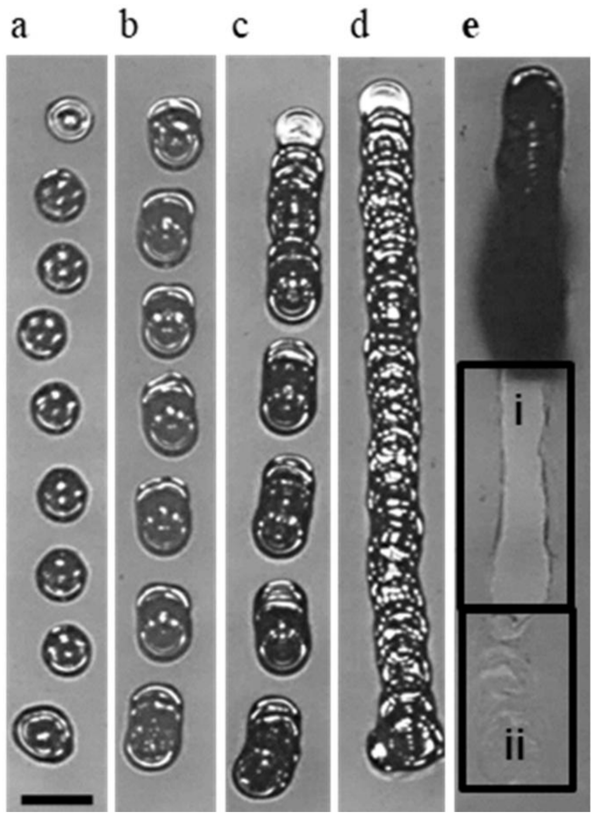

Figure 3-4. Identified line printing regimes: (a) isolated droplets, (b) isolated groupings, (c) broken line, (d) true stacked-coin, and (e) delamination regimes. Inset figures show full delamination (e, i) and partial delamination (e, ii) on Teflon-AF surface. Scale bar represents 100 µm.

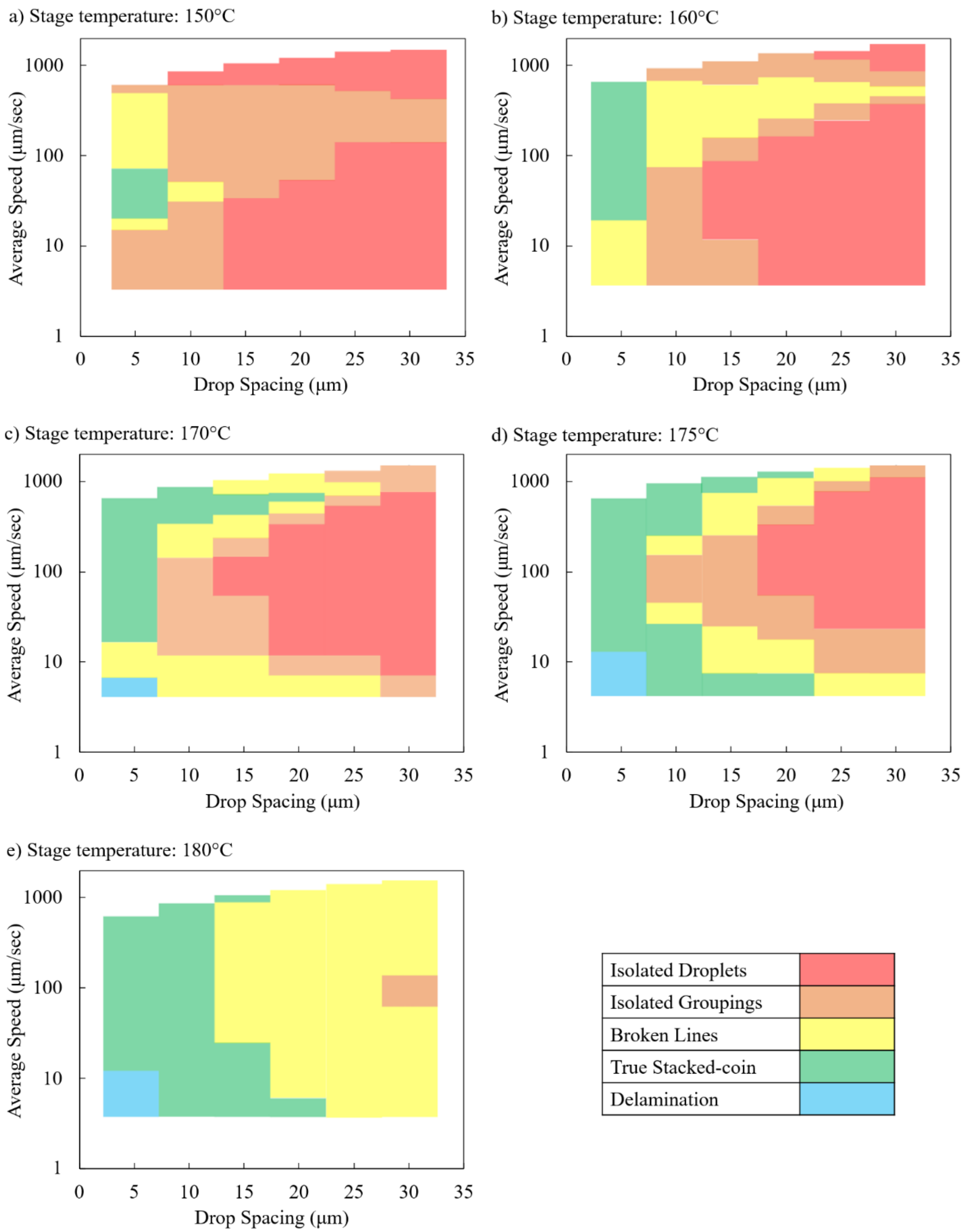

Figure 3-5. Printing behavior regime map for variable drop spacing and stage speed parameters at: (a) 150 °C; (b) 160 °C; (c) 170 °C; (d) 175 °C; (e) 180 °C.

The regime maps in Figure 3-5 clearly show that the success of this technique favors regions of high droplet overlap (low drop spacing), and high substrate temperature. Overlapping droplets are subject to lower contact angles in overlapped regions, which positively influences the printability of low drop spacings due to ink droplet pinning. At lower contact angles, it is observed that ink dries faster compared to larger contact angles.[94] The effect of increasing droplet overlap (or decreasing the drop spacing) is reflected in the regime maps, with systems printed with higher droplet overlap experiencing a larger range of conditions for true stacked-coin line formation. As drop spacing is increased, the range of stacked-coin formation decreases until reaching the system limits of 20 and 25 μm for substrate temperature of 170°C or higher (see Figure 3-5c-e). The effect of stage speed depends on the drop spacing and substrate temperature.

The critical temperature of the system is defined as 180 °C where almost only lines exhibiting true stacked-coin or broken stacked-coin behavior are recorded (Figure 3-5e). This temperature can be further identified by observations of line morphologies approaching this temperature. It is expected that increasing the hydrophobicity of the system would increase the critical temperature of the system, as drying times and the strength of dewetting of droplets are heavily influenced by droplet contact angle.[94] At lower temperatures, it is clear from the dry patterns that temperature is influential in final regime morphologies. This is evidenced by the chaotic drying patterns at lower temperatures transitioning into a predictable stacked-coin morphology at higher temperatures (Figure 3-6). Droplet coalescence is significantly influenced by spreading while sintering. As the system approaches the temperature of instantaneous drying, line morphologies begin to exhibit less evidence of wet droplet coalescence dynamics. At high temperatures impacting droplets can produce individual coffee ring morphology when drying on a pre-dried droplet. The coffee ring effect is enhanced at high temperatures, thus being an indicator that the instantaneous drying condition is met once this pattern is observed in the stacked-coin regime.[21]

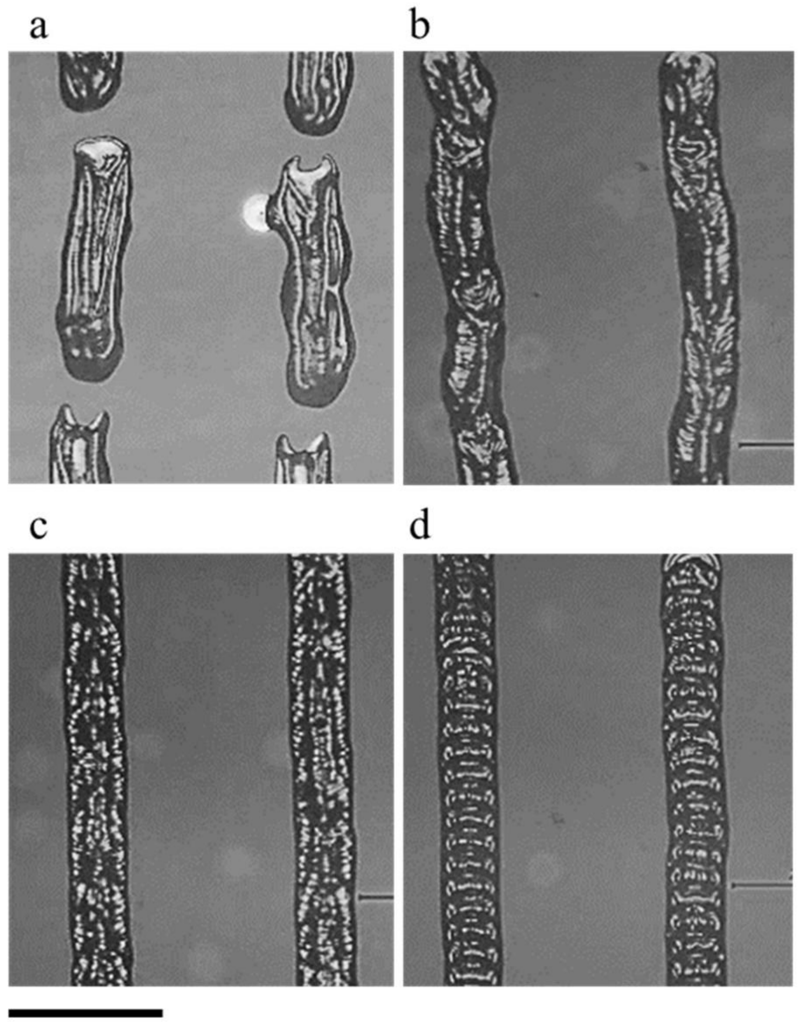

Figure 3-6. Comparison of 10 µm drop spacing lines exhibiting enhanced droplet coalescence during sintering due to spreading at the temperature of (a) 160 ºC, (b) 170 ºC, (c) 175 ºC, and (d) 180ºC. All at average stage speed 800 µm/s. Scale bar represents 200µm.

This key difference in ink behavior indicates the onset of the critical temperature, as lower temperatures possess considerable influence from droplet coalition dynamics. Upon further increasing the stage speed, line printability begins to improve across all substrate temperatures and drop spacings. This improvement is due to the asymmetric droplet impact spreading due to the stage movement at higher speeds (Figure 3-7). Asymmetric droplet impact spreading occurs when droplets impact a stage with sufficiently high speed to promote drop deformation and asymmetric spreading.[95] Typically, inkjet-printed electronics layers and devices are printed at speeds on the order of 10-100 mm/s, which is significantly faster than stage speeds used here.[96] This is due to the limitations of the apparatus which is limited to a maximum of around 1000 μm/s for the small values of drop spacing used here. Figure 3-7a shows consistent asymmetric droplet spreading across lines with a 30 μm drop spacing printed with a stage speed of 1000 μm/s (180°C). At high stage speeds, the droplet morphology appears as a connected chain. Upon further inspection, only droplets which have observable overlap to the previous droplet in the system express an asymmetric droplet profile. This suggests that while droplets will be subject to asymmetric deformation due to the high stage speeds, they will only retain this beneficial shape if they have experienced sufficient contact pinning to the previous droplet in the system. Droplet asymmetric spreading increases the length of droplets as they impact and sinter upon the surface, which can result in larger droplet overlap conditions being satisfied with subsequent overlapping droplets. With a large overlap onto the hydrophilic surface of the dried droplet, subsequent droplets can pin to the surface, thus increasing printability at higher speeds. The onset of advantageous changes in droplet regimes due to stage speed conditions occurs from 100-200 μm/s. The investigation into stage speed is limited by the acceleration capabilities of the setup. The limitations of droplet spreading is an important point of further research to identify the limitations of the throughput of this technique. Despite this, the spreading mechanisms observed at high temperatures positively influence printability and this is expected to remain true for higher speeds.

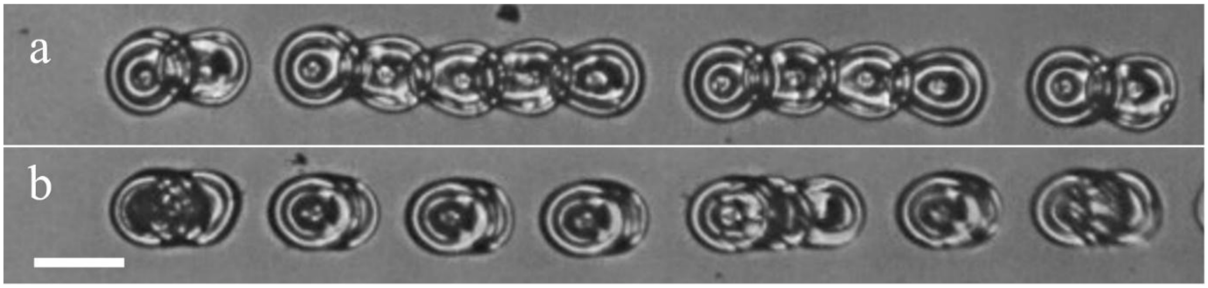

Figure 3-7. Overlapping dried droplet spreading behavior with non-overlapping isolated droplets at system critical temperature 180°C: (a) 30 μm spacing approaching 1000 μm/s, (b) 30μm spacing at 100 μm/s. Scale bar represents 50 μm.

Despite the successful production of lines, there are some notable drawbacks to this technique. The first being the technical issue of nozzle clogging. During the production of these lines, it is not uncommon for ink entrained within the nozzle to sinter due to radiative heat from the stage. The closer the printhead is to the stage, the more exposed it is to radiative heat and thus is more susceptible to nozzle clogging. Nozzle clogging is more prevalent at lower stage speeds due to the increased time between droplet jetting allowing the nozzle tip to be further influenced by the stage temperature. Regime maps at lower stage temperatures (Figure 3-5a and b) show that regimes begin to transition towards isolated droplets at high speeds after experiencing transitions towards true stacked-coin morphology at intermediate speeds. This is not reflected at higher stage temperatures within the observed limits of the experimental system. Higher stage speeds would further impact the line formation phenomenon as there may be a limit to the enhanced printability caused by asymmetric spreading. While this study has utilized stage heating to achieve a fast-drying condition, this limits the application of the technique to substrates which are not thermosensitive relative to the instantaneous drying temperature of the ink. Despite this, the intrinsic mechanisms of this technique may be applied to UV sensitive conductive ink options, overcoming the thermos-sensitivities of a substrate while ensuring instantaneous drying with UV radiation. The timescale of droplet ejection vs evaporation is a key factor for consideration for this technique, being a key factor in larger successful printability regions at lower stage speeds. The different drop spacings and stage speed values investigated here, provide a printability range for silver ink droplets on Teflon-AF surface. Varying the drop spacing and stage speed in tandem results in large differences between droplet deposition delay and evaporation time for droplets printed within each temperature regime. Compared with the regimes of printability experienced on a hydrophilic stage, there are significant differences of note. Only one successful region of printability exists for hydrophobic substrates (stacked-coin morphology), while a range of successful connected lines (including scalloped and bulged lines) can be achieved on hydrophilic substrates, with uniform being desirable.[21] Moreover, the droplet deposition delay is a more suitable factor than stage speed to define printability ranges, which is influenced by both stage speed and drop spacing. Finally, asymmetrically dried droplets are of great importance to increase the printing throughput for this technique and it can be considered as a promising direction of research.

3.4. Conclusions

This chapter defines and analyzes the successful printing regimes of stacked-coin lines on a hydrophobic surface. The effects of stage speed, drop spacing, and stage temperature have been identified as the key printing parameters controlling line printability. The mapping of printability regimes based on temperature and drop spacing can thus be used to successfully predict the onset conditions of true stacked-coin morphology. The critical temperature of the system, ensuring instantaneous drying at all applicable drop spacings was found to be 180 ºC. A maximum drop spacing of 20 μm was identified, above which true stacked-coin regime cannot be achieved. Also, speeds up to 20 μm/s are the most sensitive to rapid regime changes surrounding onset conditions. Asymmetric droplet spreading has also been identified as a key characteristic which fundamentally improves the printability of these lines. This phenomenon has shown distinct promise for the application of this technique in achieving higher printing throughputs in the future.

Chapter 4: Organic thin-film transistors with inkjet-printed electrodes on hydrophobic Teflon-AF gate dielectric

This chapter was published in the journal Organic Electronics, Copyright Elsevier.

Paria Naderi, Gerd Grau, Organic thin-film transistors with inkjet-printed electrodes on hydrophobic Teflon-AF gate dielectric with reversible surface properties, Organic Electronics, Volume 108, 2022, 106612, ISSN 1566-1199, https://doi.org/10.1016/j.orgel.2022.106612.

4.1. Introduction

In chapter 1, fundamentals of printed OTFTs were briefly discussed. In chapters 2 and 3, two methods of inkjet printing patterns on hydrophobic surfaces were explored. In this chapter, OTFTs incorporating a hydrophobic gate dielectric are presented. In the fabrication process, plasma treatment is used to render the dielectric surface wettable. However, plasma treatment affects the surface properties of the dielectric layer which are reversed after a post-annealing step to anneal the silver source and drain electrodes. The results of this chapter are very insightful for future research in solution-processed OTFTs, while they confirm the usefulness of printing methods that were demonstrated in the previous chapters.

TFTs have applications in flexible, low cost and versatile electronics and a lot of research has been carried out to improve their fabrication process and performance of the final products. Using fluoropolymers as the gate dielectric has a number of advantages. Due to their water-repellency, fluoropolymers are used in transistors as the gate dielectric or encapsulation to prevent possible doping and charge trapping in the channel[32,44]. A smoother dielectric surface leads to larger grain sizes and fewer defects in the organic semiconductor (OSC) channel[97,98]. In TFTs, since charge transport happens within a few nanometers from the semiconductor/ dielectric interface, the dielectric surface properties become very important[99–101]. However, it can be quite challenging to incorporate hydrophobic fluoropolymers in solution-processed electronic devices. To fabricate transistors with a small channel length, the source and drain electrodes are inkjet-printed and the surface is required to have high wettability. As was discussed in chapter 2, one method of increasing surface wettability is to use plasma treatment. However, plasma-etching on fluoropolymer films increases the film's roughness and alters its chemical bonds on the surface [41]. In many reports, OTFTs with hydrophobic gate dielectric are limited to vacuum processed electrodes due to the difficulty of printing electrodes and/or the OSC onto a hydrophobic dielectric [45,46]. There are examples of solution-processed electrodes in OTFTs with conductive inks such as silver and gold on surface-modified hydrophobic gate dielectrics like Teflon-AF and Cytop. To overcome the low surface energy of fluoropolymers, some reports used selective surface energy patterning combined with blanket coating of metal nanoparticle inks, which requires a mask and is difficult on heterogeneous substrates [67,102]. Another method is extrusion printing combined with plasma surface modification, however, the resolution is low [103]. Therefore, there is a need to study scalable, high-resolution printing methods such as inkjet printing to fabricate OTFT electrodes on fluoropolymers. Furthermore, the effect of surface-modification on these fluoropolymer surfaces and the OSC/dielectric interface has not been studied so far. In this thesis, in an effort to inkjet print electrodes with small separation distance (transistor channel length), the effect of plasma treatment on Teflon-AF as the transistor gate dielectric is studied and its reversible surface properties are characterized.

Hydrophobic fluoropolymers are a promising candidate for gate dielectrics in OTFTs since they have low charge trap density, electrical and chemical resistance to the environment, low dielectric constant, and water repellency.[32,44] In many reports, OTFTs with hydrophobic gate dielectric are limited to vacuum processed electrodes due to the difficulty of printing electrodes and/or the OSC onto a hydrophobic dielectric.[45,46] Other than their water-repellency and smooth surfaces, fluoropolymers have low dielectric constant, which enhances the charge transport in the semiconductor channel.[104] The strong C-C and C-F bonds are what make fluoropolymers unique. Their interesting properties such as thermal stability, chemical inertness, and low dielectric constant have made them suitable candidates for tubing and coating, cable insulation, cardiovascular grafts, and protective coating in printed circuit boards[34,105,106]. Polytetrafluoroethylene (PTFE), commercially known as Teflon, is perfluorinated polyethelyne in which all the hydrogen atoms have been replaced by fluorine. In other words, fluorine atoms cover the C-C backbone and enrich it with useful characteristics such as low surface tension (18 mN/m) and low dielectric constant (2.1)[105]. Teflon amorphous fluoropolymers (Teflon-AF) are copolymers of Teflon and 2,2-bis(trifluoromethyl)-4,5-difluoro-1,3 dioxole. They have low refractive index (~1.3), low dielectric constant (~1.9), high optical transparency (from around 200 nm to 2000 nm wavelength), and no crystallinity. Their applications range from chemical separators and sensors to platforms for biological assays.[107,108] Teflon-AF is available in two grades depending on its glass transition temperature (T_g): Teflon-AF 1600 (T_g=160 °C) and Teflon-AF 2400 (T_g=240 °C). Teflon-AF is especially useful for coating applications where surface hydrophobicity is the key requirement to encapsulate an electrical device from environmental effects [109] or as the gate dielectric in solution-processed organic thin-film transistors

(OTFTs) [44,67,77,103,110]. The chemical structure of Teflon (PTFE) and Teflon-AF are shown in Figure 4-1.

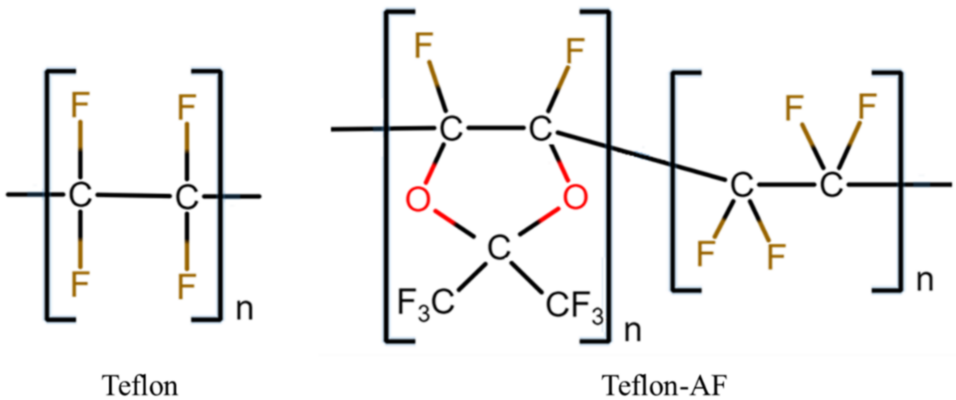

Figure 4-1. Chemical structures of Teflon (PTFE) and Teflon-AF

Teflon-AF has been used as the gate dielectric in solution-processed OTFTs[44,67,77,103,110] because of its interesting properties. However, due to their low surface energy, one cannot easily form patterns on these films through low-viscosity solution-processing techniques such as inkjet printing of electrodes. To combat this wettability issue, surface modification is often performed on these films to decrease their hydrophobicity. Plasma treatment is convenient, it changes the surface without tampering with the bulk, its effect is uniform, and it does not require the use of hazardous chemicals [36]. Some studies have investigated the nature of surface modification of fluoropolymers such as crystalline PTFE through plasma treatment [36,37,39,40,111]. In other contexts, some reports show that heat recovers the surface of different fluoropolymers after they have been modified either by plasma treatment or humidity[112]. In a solution-processed bottom-gate-bottom-contact (BGBC) OTFT, the hydrophobic gate dielectric undergoes a series of processing steps. After the dielectric film is solution-deposited, it is annealed once for its solvent to evaporate. Then, the film surface is modified to increase its wettability to prevent dewetting and improve adhesion of the next solution-processed layer. Plasma treatment can change the surface both chemically and morphologically.[41] Therefore, since the channel is only a few nanometers thick, a nanometer-scale change in the surface could alter carrier transport.[99,113] Finally, with the annealing of the next layer (electrodes or another polymer layer), the gate dielectric is also annealed at least one more time. When using fluoropolymers as the gate dielectric, this post-annealing step can reverse the effect of the plasma treatment.

In this chapter, we first show the fabrication process for OTFTs with inkjet-printed silver source and drain electrodes on a fluoropolymer gate dielectric. We study the effect of the electrode processing on Teflon-AF as the gate dielectric and take advantage of its reversible properties to engineer the OSC/dielectric interface. By varying the post-annealing temperature, the surface properties of Teflon-AF change, which causes the OSC/dielectric interface to change. It is demonstrated that the state of the Teflon-AF surface clearly affects the extracted transistor parameters such as mobility, on-current, off-current, on/off current ratio, and the threshold voltage. Our findings show that after plasma treatment, the wettability, roughness, and the percentage of reactive elements like oxygen increase on the surface of the films. However, they all decrease after post-annealing corresponding to improvements in the OTFT performance. This confirms the importance of Teflon-AF surface reversibility to engineer the OSC/ dielectric interface in a printed transistor fabrication process.

4.2. OTFT preparation

The complete OTFT fabrication process is shown in Figure 4-2. BGBC configuration was employed. The transistors were fabricated on indium tin oxide (ITO)-coated glass slides (Sigma-Aldrich, Oakville, Canada). The ITO film was used as the gate electrode. Teflon-AF 1600 was dissolved in Fluorinert FC-40 in a 1.6 wt. % solution. The solution was spin-coated in two steps at 600 rpm for 1 minute and dried at 150 °C for 15 minutes each time, resulting in an overall thickness of 450 nm. The dielectric layer was then air plasma-treated for 1 minute at 200 W with a PE-50 plasma system (50 kHz). Afterwards, the source and drain electrodes were inkjet-printed using a silver nanoparticle ink. A custom-built inkjet printer with a 60 µm diameter nozzle was used. The channel width of the devices was 1,300 µm, and the channel length was varied from 20 µm to 75 µm. The printed source and drain electrodes were dried first at 60 °C for 5 minutes to prevent the coffee ring effect and then annealed at different temperatures for the purpose of this study. The organic semiconductor poly(2,5-bis(2-octyldodecyl)-3,6-di(pyridin-2-yl)-pyrrolo[3,4-c] pyrrole-1,4(2H,5H)-dione-alt-2,2'-bithiophene) (PDBPyBT) (Ossila Ltd, Sheffield, UK) was dissolved in chloroform with 10 mg/ml concentration and was spin-coated at 3,000 rpm followed by annealing at 120 °C for 10 minutes.

To study the effect of plasma treatment directly on the OTFT performance, devices with no post-annealing condition were also tested. In this case, after annealing printed electrodes at two different temperatures (100 °C and 160 °C), the samples were plasma treated one more time.

Samples for Teflon-AF characterization were fabricated in the same way without the printed electrodes and the organic semiconductor. All devices were fabricated and tested in ambient conditions.

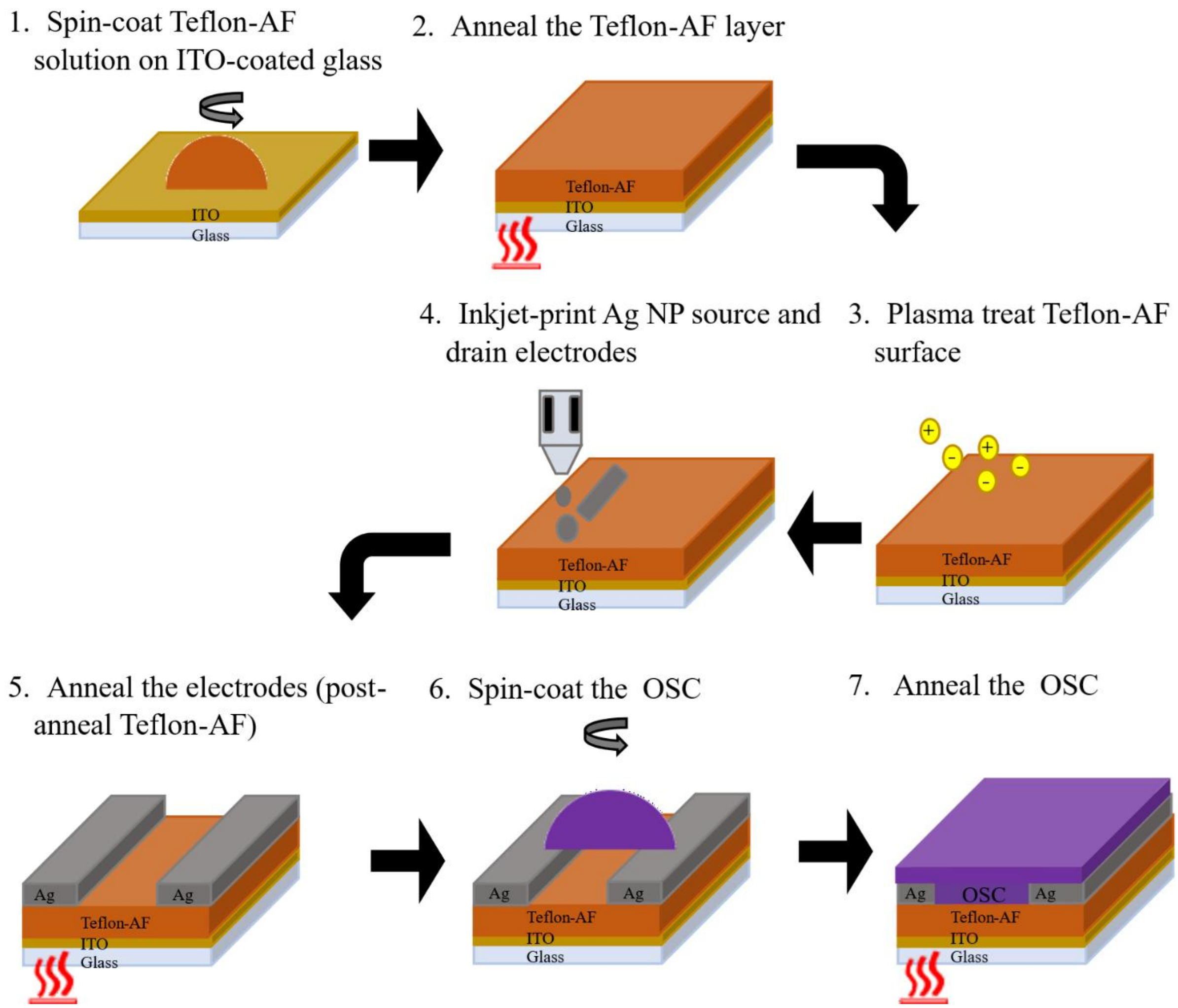

Figure 4-2. OTFT fabrication process

4.2.1. Plasma treatment of Teflon-AF

Figure 4-3a and b show the printed source and drain electrodes without and with plasma treatment. When printing silver nanoparticle ink, the ability of the ink droplets to wet the surface is crucial for the formation of continuous, conductive lines. Before plasma treatment, due to the low surface wettability of Teflon-AF, the ink droplets do not spread out or wet the surface properly. As can be seen in Figure 4-3a, the droplets bead up instead, making it impossible to form fine, continuous lines through inkjet printing. Air plasma treatment significantly alters the surface characteristics of Teflon-AF. After plasma treatment, the wettability of Teflon-AF surface increases. See Figure 4-3b. The ink droplets now spread out and coalesce into fine lines upon printing, allowing for the formation of high-resolution, conductive patterns.

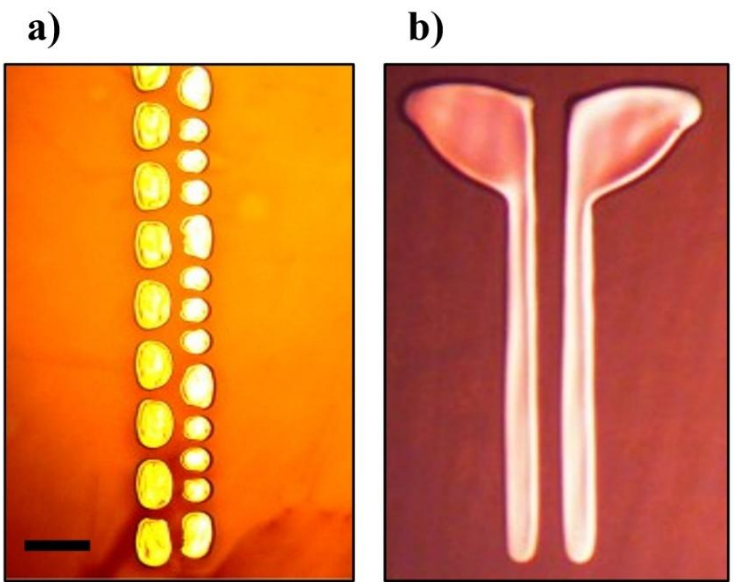

Figure 4-3. Optical micrographs of printed source and drain electrodes (a) without plasma treatment, (b) with plasma treatment. Scale bar represents 200 μm.

4.3. OTFT performance

The fabricated transistors were characterized using a semiconductor parameter analyzer (Keithley 4200, Tektronix). As was discussed in the introduction chapter, two I-V measurements are required to analyze the performance of the devices: transfer characteristics (I_dV_g) and output characteristics (I_dV_d). Transfer characteristics are used in this section to extract transistor parameters. Figure 4-4 shows the transfer characteristics (I_dV_g) at V_d = -120 V for 20 μm channel length devices without and with different post-annealing temperatures in forward gate voltage sweeping condition. As can be seen from Figure 4-4, the on-current values and the slope of the square root of the drain current are higher for post-annealing temperatures of 120 °C, 140 °C, and 160 °C. The devices below and above this range show clear deterioration in performance. Figure 4-5 shows the performance trend versus the post-annealing temperature for the following metrics: average and maximum saturation field-effect mobility (μ_{sat}), average and maximum linear field-effect mobility (μ_{lin}), average and maximum on-current (I_{on}) normalized by channel width and length, log of off-current ($Log(I_{off})$), threshold voltage (V_t), saturation subthreshold swing (SS), and log of on-off current ratio ($Log(\frac{I_{on}}{I_{off}})$). These parameters were averaged over the whole range of channel lengths from 20 μm to 75 μm.

The saturation field-effect mobility is calculated from the slope of the square root of the drain current versus gate voltage from I_dV_g characteristics in the saturation regime:

$$\mu_{sat} = \frac{2L}{C_{ox}W}\left(\frac{\partial\sqrt{I_d}}{\partial V_g}\right)^2 \qquad 4\text{-}1$$

where W and L are the channel width and length of the transistor channel, and C_{ox} is the dielectric capacitance per unit area. Devices with no post-annealing step have low performance. The devices post-annealed at 160 °C have the highest mobility (average: 0.12 cm^2/V.s and maximum: 0.19 cm^2/V.s), and the devices post-annealed at 120 °C have the highest on/off current ratio (average:

5.5×10^5 and maximum: 3.4×10^6). The saturation and linear field effect mobility and the on-current are highest at post-annealing temperatures between 120 °C and 160 °C. The other parameters are initially constant with post-annealing temperature up to 160 °C. At this point, V_t abruptly starts becoming more negative, SS and I_{off} increase and I_{on}/I_{off} decreases. Two different regimes can be observed. At low post-annealing temperatures, on-state performance increases as the post-annealing modifies the Teflon-AF dielectric. At high post-annealing temperatures, both on- and off-state performance deteriorate.

In Figure 4-4, for post-annealing temperatures above 160 °C, the gate-induced drain leakage increases for positive V_g. For $V_g > 0$, the OSC traps electrons which attracts the holes accumulated at the gate side of the dielectric, leading to an increase in leakage current.[114] However, the bulk characterization in section 4.7 shows that Teflon-AF capacitance does not change when the film is exposed to higher annealing temperature.

Therefore, it is important to identify the optimal post-annealing temperature. It is worth noting that other transistors reported using this OSC (PDBPyBT) or other DPP derivatives, have used evaporated source and drain contacts and inert atmosphere processing conditions for the OSC [46,115,116]. The transistors fabricated here, despite having inkjet-printed contacts and ambient atmosphere processing for the OSC, show comparable performance to transistors with the same device structure and otherwise same OSC processing conditions.

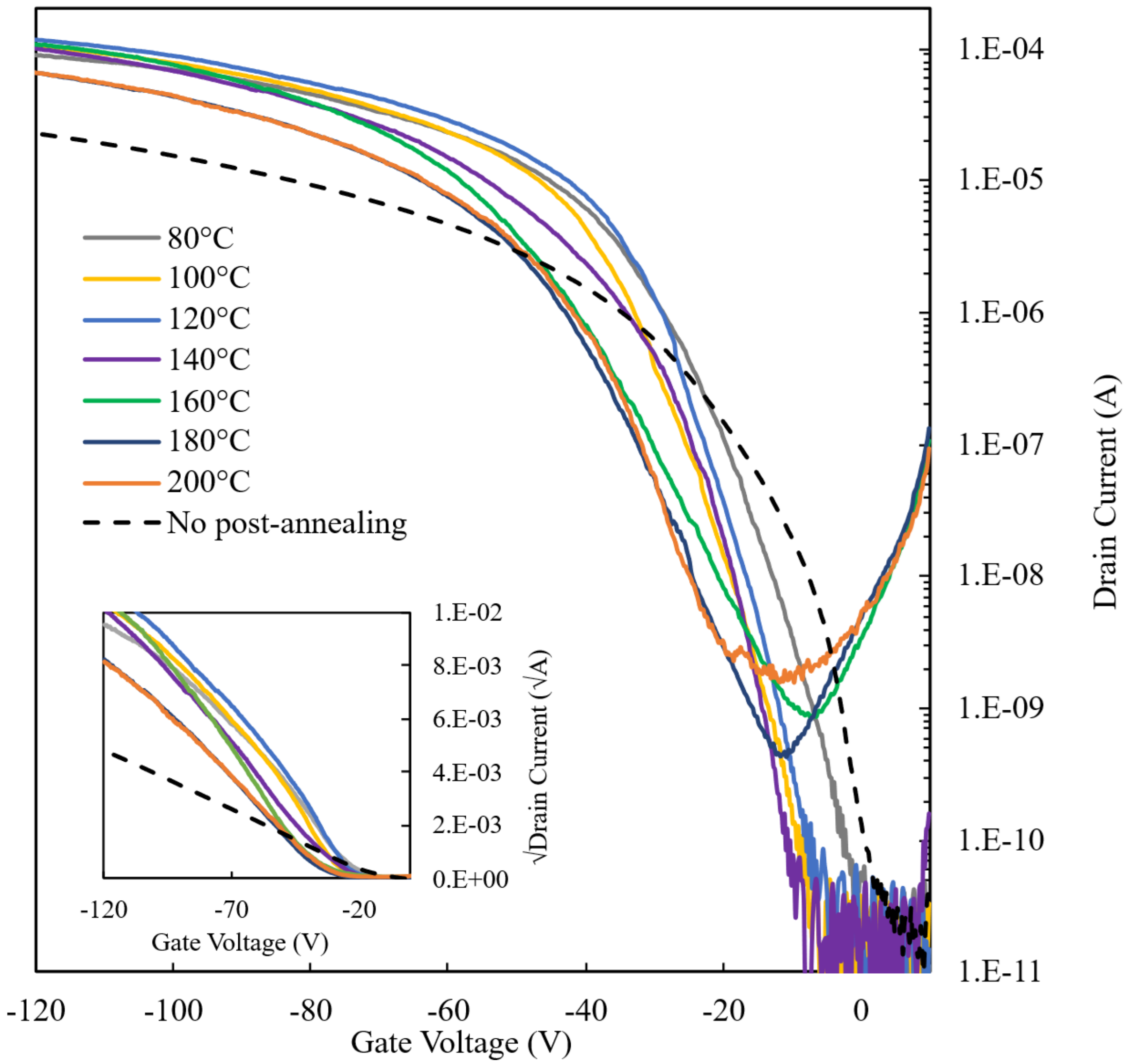

Figure 4-4. Transfer characteristics (I_dV_g) at V_d = -120 V of 20 μm channel length devices without and with different post-annealing temperatures. Inset shows the square root of drain current versus post-annealing temperature.

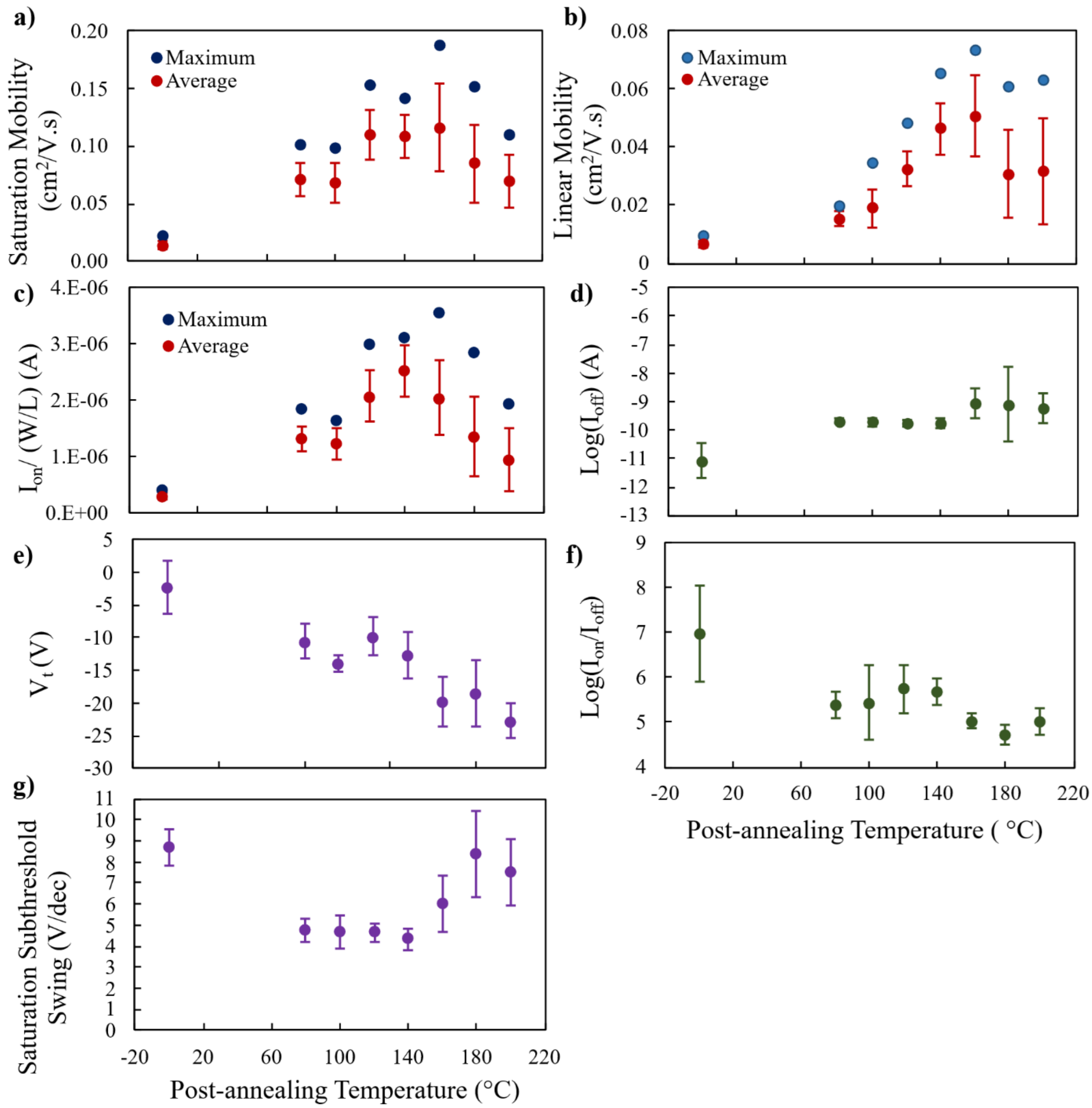

Figure 4-5. Graphs of (a) average and maximum saturation field-effect mobility extracted at V_d = -120 V, (b) average and maximum linear field-effect mobility extracted at V_d= - 20 V, (c) Average and maximum width and length normalized on-current, (d) log of off-current, (e) threshold voltage, (f) log of on-off current ratio, and (g) saturation subthreshold swing.

4.3.1. Contact resistance measurements

As shown in Figure 4-5, a clear trend is observed between all OTFT parameters and Teflon-AF post-annealing temperature with different regimes. There are different phenomena affecting the performance of organic transistors. For instance, controlling the OSC/ dielectric interface with the aim of minimizing the trap density in the channel can lead to high mobility devices [117,118]. At the same time, it is well-known that organic field-effect transistors suffer from limitations caused by contact resistance [28], and since the post-annealing temperature is, in fact, the silver source and drain annealing temperature, it may affect the contact resistance. To understand the effect of contact resistance, two methods were used, the transmission line method (TLM) and the Y-function method (YFM). Both methods were discussed in chapter 1.

5.2.2.4. Extracting contact resistance using TLM

For TLM, the output characteristics are used. Figure 4-6 shows the output characteristics (I_dV_d) of a 20 μm channel length device with electrodes post-annealed at 160 °C. First, the total resistance was extracted from the inverse of the slope of the output characteristics in the linear regime. For TLM, it is necessary to vary the channel length and then plot the total resistance versus channel length. Figure 4-7 shows three transistors with three different channel lengths: 20 μm, 50 μm and 75 μm. For the contact resistance calculations, transistors with channel lengths of 20, 30, 40, 50, 60 and 75 μm were used. The width normalized contact resistance and channel resistance per channel length were extracted from the y-intercept and the slope of the plots. The results are shown in Figure 4-8a and b.

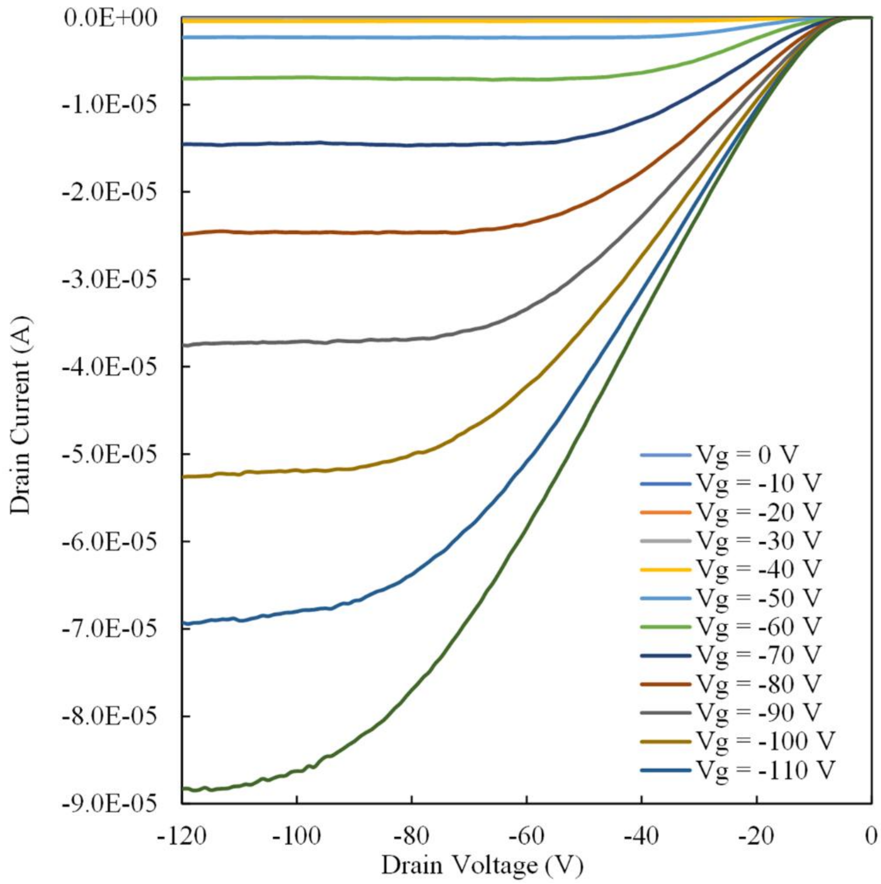

Figure 4-6. Output characteristics (I_dV_d) of a 20 µm channel length device post-annealed at 160°C

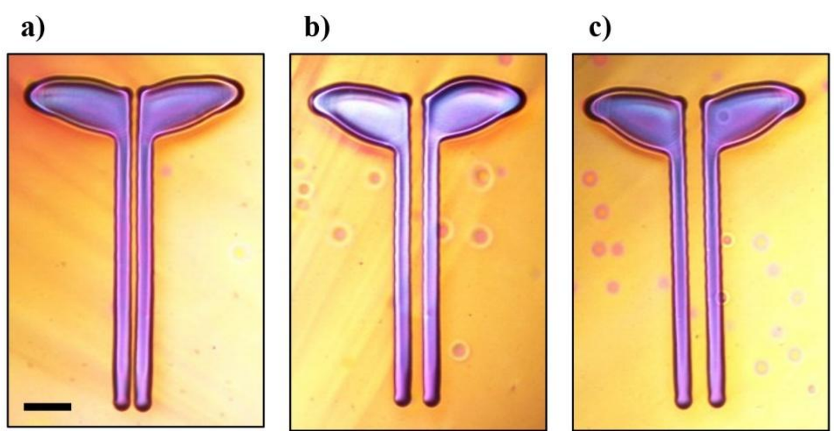

Figure 4-7. The final device with (a) 20 µm, (b) 50 µm and (c) 75 µm channel length, with the OSC spin-coated on top. Scale bar represents 200 µm.

5.2.2.5. Extracting contact resistance using YFM

Next, YFM was used to calculate the low-field mobility and the contact resistance ($R_c = R_{sd}/2$) for all the post-annealing temperatures. The results are shown in Figure 4-8c and d. Low-field mobility is the intrinsic carrier mobility of the transistor, which is not affected by contact resistance. The YFM technique is introduced in detail in Ref. [28]. In the YFM, the transfer characteristic (I_dV_g) in the linear regime is used. The extraction process was discussed in detail in the introduction chapter. Using the current equation in the linear regime, the Y function is defined as:

$$Y = \frac{I_d}{\sqrt{g_m}} = \sqrt{\frac{W}{L} C_{ox}\mu_0 V_d} \times (V_g - V_t) \qquad 4\text{-}2$$

where g_m is the transconductance, W and L are the channel width and length of the transistor, C_{ox} is the dielectric capacitance per unit area, μ_0 is the low-field mobility, V_d is the drain current (here -20 V), and V_t is the threshold voltage. From the slope of Y versus V_g, μ_0 is obtained and from the x-intercept, V_t is extracted. To calculate contact resistance, mobility attenuation factor θ was extracted, which gives us contact resistance:

$$\theta = \theta_0 + \theta^* = \theta_0 + G_m \times R_{sd} \qquad 4\text{-}3$$

where θ_0 (≈ 0), G_m and R_{sd} are the mobility reduction coefficient, transconductance parameter, and the source-drain contact resistance, respectively. In the next step, we plot $\frac{1}{\sqrt{g_m}}$ versus $V_g - V_t$, using the below equation:

$$\frac{1}{\sqrt{g_m}} = \frac{1+\theta(V_g - V_t)}{\sqrt{\frac{W}{L} C_{ox} \mu_0 V_d}} \qquad 4\text{-}4$$

From the x-intercept, we extracted θ, from which we can obtained contact resistance.

5.2.2.6. Analysis of the results extracted from the two methods

The low-field mobility changes with post-annealing temperature with the maximum value at 160 °C (Figure 4-8d) and it exhibits the same trend as the saturation field-effect mobility shown in Figure 4-5a.

The contact resistance values extracted from the two methods (Figure 4-8a and c) are very close to each other and follow the same trend, which confirms the reliability of both methods in proving that the contact resistance is independent of post-annealing temperature.

Furthermore, channel resistance and low-field mobility exhibit the same trends as well as comparable values when converting between them (Figure 4-8b and d). Therefore, here with contact resistance not changing and μ_0 and channel resistance changing with post-annealing temperature, we conclude that the main factor contributing to the change in transistor performance is the change in the OSC/dielectric interface. This interface is where the organic semiconductor material comes into contact with the gate dielectric—Teflon-AF in this case. It is at this critical juncture that the majority of the device performance characteristics are determined. The channel resistance and low-field mobility are two fundamental parameters that characterize the performance of transistors, and they are interrelated. Channel resistance ($R_{channel}$) quantifies the resistance offered by the semiconductor material of the channel to the flow of charge carriers when a voltage is applied across it. This resistance is influenced by the channel length (L), channel width (W), material properties, and the interface quality between the semiconductor and the dielectric. TLM is employed to determine $R_{channel}$ by fabricating a series of devices with varying channel lengths and measuring their total resistances. Low-field mobility (μ_0) represents the rate of charge carrier movement per unit electric field under low electric field conditions, where the carrier velocity is directly proportional to the applied electric field. It provides an indication of how readily charge carriers can traverse the semiconductor material. The correlation between channel resistance and low-field mobility stems from the fundamental operation of a field-effect transistor (FET). The drain current (I_d) in the linear region is simplified as (equation 1-5 in Chapter 1):

$$I_d = \mu_{lin} C_{ox} \left(\frac{W}{L}\right)\left(V_g - V_t\right)V_d$$

where μ_{lin}, C_{ox}, W, and L are the linear field-effect mobility, the gate oxide capacitance per unit area, channel width, and channel length, respectively.

Rearranging this equation to solve for channel resistance yields:

$$R_{channel} = \frac{1}{\mu_{lin} C_{ox} \left(\frac{W}{L}\right)\left(V_g - V_t\right)} \qquad \text{4-5}$$

While μ_{lin} can be expressed in terms of μ_0 using θ [28]:

$$\mu_{lin} = \frac{g_m}{\left(\frac{W}{L}\right)\left(V_g - V_t\right)V_d} = \frac{\mu_0}{[1 + \theta\left(V_g - V_t\right)]^2} \qquad \text{4-6}$$

These expressions reveal that channel resistance is inversely proportional to low-field mobility; as mobility increases, channel resistance decreases, assuming all other factors are held constant. This inverse relationship can be observed in Figure 4-8b and d.

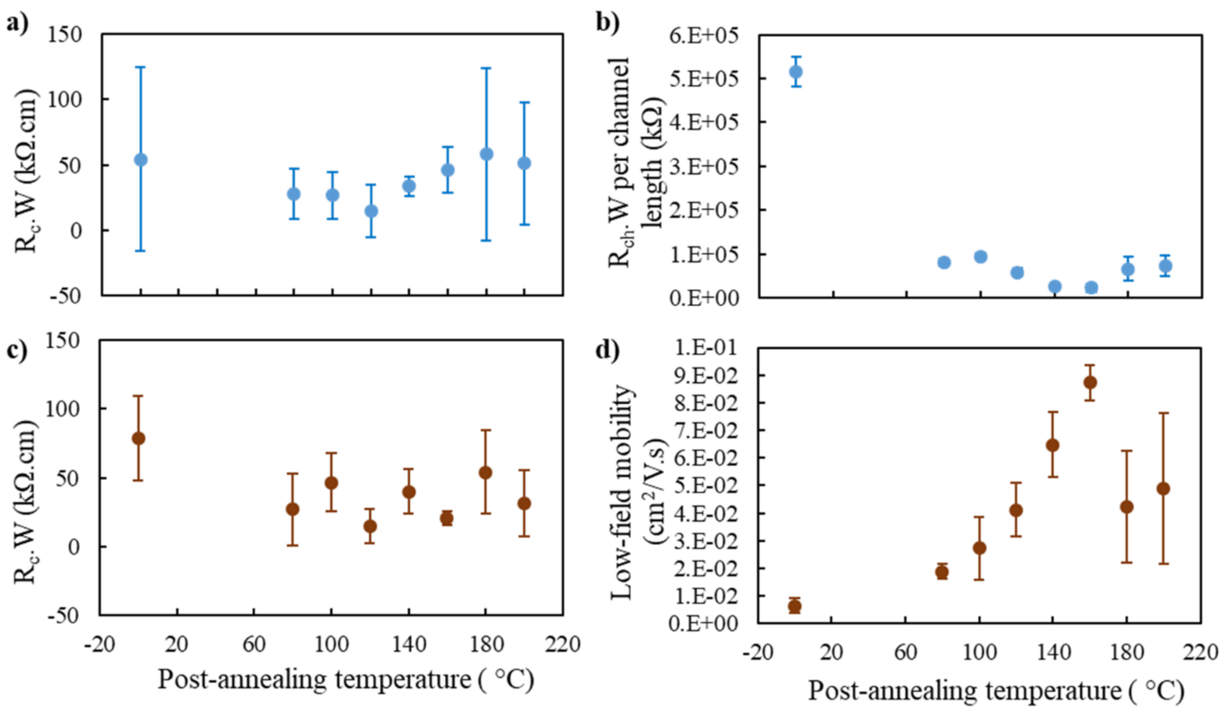

Figure 4-8. Width normalized (a) contact resistance, and (b) channel resistance per channel length calculated using TLM. (c) Width normalized contact resistance, and (d) low-field mobility calculated using YFM. The contact resistance values extracted from the two methods are very close to each other and show that the contact resistance is independent of post-annealing temperature.

In practice, both TLM and YFM provide complementary information. TLM can separate the channel resistance from contact resistance, giving a direct measure of the channel's inherent resistance. YFM, on the other hand, provides insight into how easily charge carriers move within the channel under a low electric field, which is influenced by the channel resistance including the quality of the semiconductor and the interface with the dielectric layer. When both methods are applied, a complete picture of the transistor's electrical behavior can be ascertained.

After rejecting contact resistance as a major factor here and consequently the possible effect of post-annealing on the electrodes, the focus will be directed to the OSC/ dielectric interface. Hence, in the following sections, the effect of the post-annealing on the Teflon-AF surface wettability, morphology, and chemistry are studied. It is also worth noting that the devices with no post-annealing were tested with two different silver annealing temperatures (100 °C and 160 °C) that performed very similarly to each other.

4.4. Wettability: water contact angle measurements on Teflon-AF films

The advancing and receding contact angles (CA), along with the contact angle hysteresis of deionized (DI) water droplets on Teflon-AF films before and after air plasma treatment and after the post-annealing step, are presented in Figure 4-9. The contact angle of DI water was measured using a Kruss DSA10 contact angle measurement system. Each error bar was calculated using 12 to 14 data points. The advancing CA before plasma treatment is 118.4°, which indicates the hydrophobicity of the surface. The receding contact angle is slightly lower and is equal to 109.7°. Therefore, the contact angle hysteresis is just below 10°. After plasma treatment, the advancing and receding contact angles drop to 101.7° and 36° respectively (still considered as hydrophobic), causing the CA hysteresis to increase to 66°. After post-annealing the films at 80 °C, the advancing CA increases to 118.1°. For higher annealing temperature, it increases further at a slow rate up to 121° at 200 °C. Conversely, the receding CA is still low at 80 °C (66°) and has a higher rate of increase to 109.7° at 200 °C. Thus, the CA hysteresis decreases from 66° to 10.3°. The receding CA changes most dramatically following the plasma treatment and post-annealing steps. Figure 4-10a-d show the difference in the receding CA for 80 °C and 200 °C post-annealing temperatures, while their advancing CAs are not very different. The high CA hysteresis and overall lower CA at lower post-annealing temperature are indicative of two possible causes: a rougher surface caused by plasma treatment or/and the presence of reactive elements caused by plasma treatment which results in liquid sorption and wetting of the surface. Likewise, the low CA hysteresis and higher CA at higher post-annealing temperature can be explained by lower roughness or/and lower percentage of reactive elements, which prevent the wetting of the surface. Both roughness and surface chemistry of the dielectric/ OSC interface can affect transistor behavior. Additionally, changes in dielectric CA can affect the thickness of the solution-processed OSC and potentially OTFT performance. These different phenomena are investigated in the next sections.

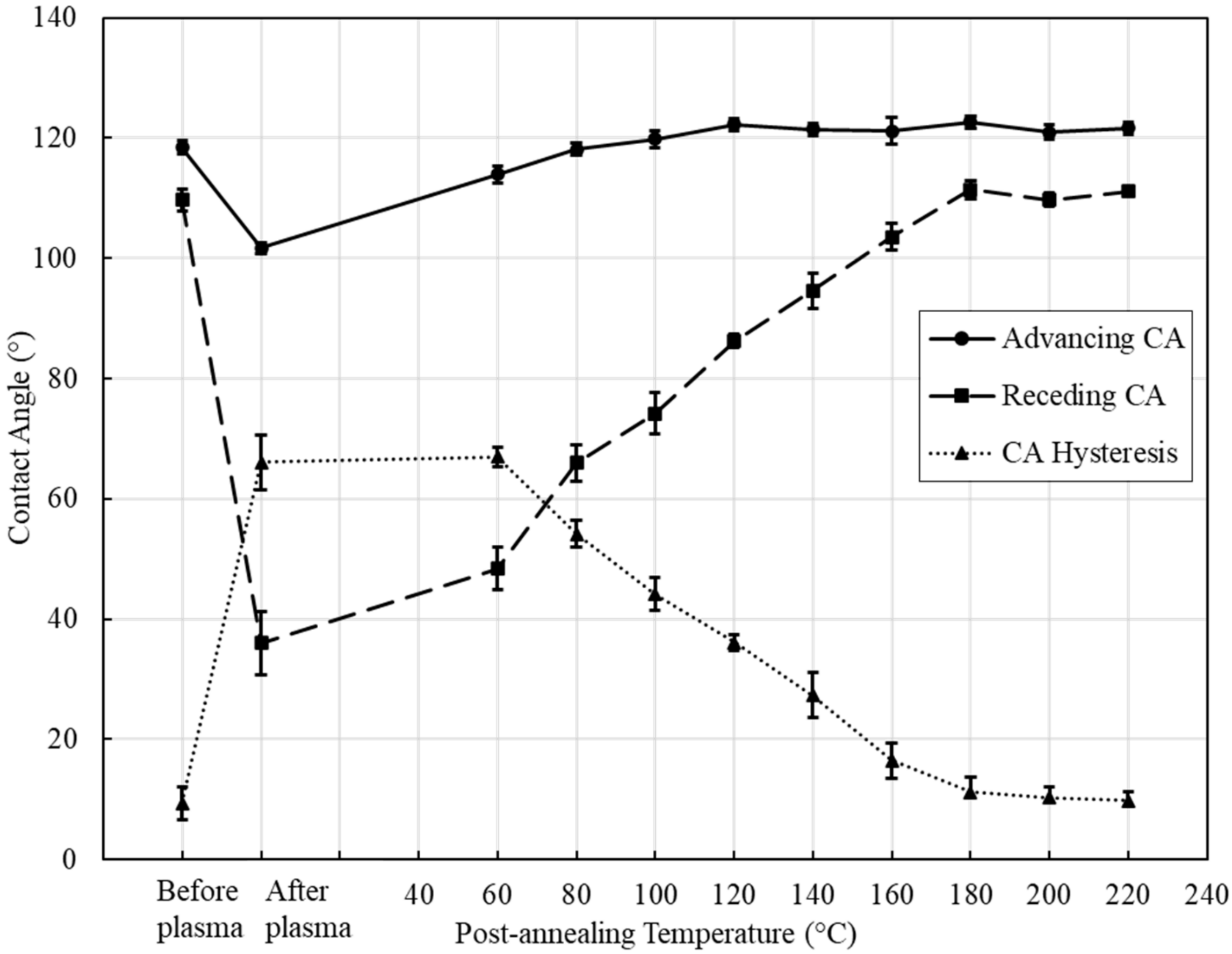

Figure 4-9. Advancing and receding CA, and CA hysteresis of DI water on Teflon-AF films before and after air plasma treatment and after post-annealing. Both advancing and receding CA decrease after plasma treatment and recover with post-annealing. The decrease in receding CA is much larger than for advancing CA resulting in increased CA hysteresis after plasma treatment.

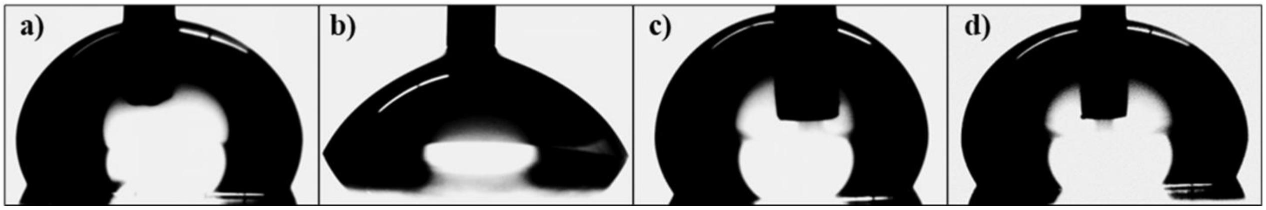

Figure 4-10. Images of droplets on films post-annealed at 80 °C are shown in (a) for advancing and (b) receding mode. Similarly, droplets on films post-annealed at 200 °C are shown in (c) for advancing and (d) receding mode. The receding CA for samples post-annealed at 80 °C and 200 °C are very different, while the difference for advancing CA is smaller.

4.5. Organic semiconductor

Figure 4-11 shows the OSC thickness versus Teflon-AF post-annealing temperature. At 180 °C and 200 °C, the OSC preferentially wets the source and drain electrodes and channel. It dewets from the Teflon-AF dielectric in other areas due to the low CA hysteresis. This increase in the OSC thickness can explain the increase in the transistor off-current (Figure 4-5d) beyond 160 °C. For lower Teflon-AF post-annealing temperatures, the OSC thickness varies less strongly but still increases with temperature due to the changing surface wettability. To confirm whether the changes in OTFT electrical characteristics with post-annealing temperature up to 160 °C are due to changes in the Teflon-AF surface properties or the OSC thickness, another set of devices was fabricated with a post-annealing temperature of 120 °C and a lower spin speed (2,000 rpm compared with 3,000 rpm for all other samples). The average OSC thickness expectedly increased from 114 nm to 182 nm, which is comparable to the 160 °C post-annealed devices with the best on-state performance. This thickness increase caused the off-current to increase from 1.8×10^{-10} A to 5.2×10^{-10} A. By decreasing the spin speed to 2,000 rpm, the interface-dependent parameter threshold voltage only changes marginally from -9.8 V to -9.3 V. The average saturation mobility and on-off current ratio decreased from 0.11 cm^2/V.s to 0.08 cm^2/V.s, and from 5.5×10^5 to 1.9×10^5, respectively. Therefore, it can be concluded that OSC thickness cannot explain the improvement in OTFT performance with post-annealing.

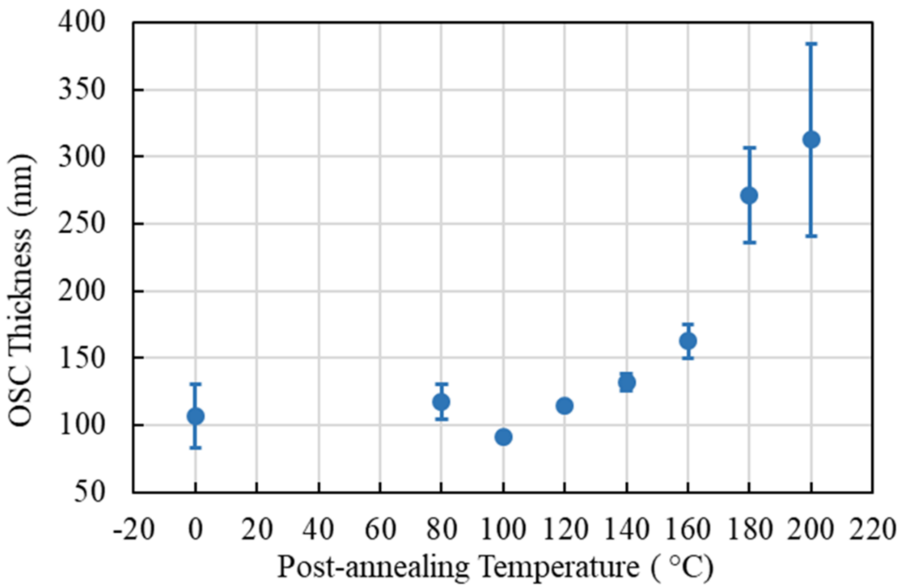

Figure 4-11. OSC thickness versus post-annealing temperature shows an increasing trend with increasing temperature.

4.5.1. Testing another OSC: TIPS-pentacene

To show the generality of the effect of post-annealing of Teflon-AF on device performance, transistors with another OSC, 6,13-Bis (triisopropylsilylethynyl) pentacene (TIPS-pentacene) as the OSC were also fabricated. TIPS-pentacene was dissolved in Hexane in a 10mg/ml solution. TIPS-pentacene solution was drop-cast on the post-annealed devices, and it was annealed at 40 °C for 10 minutes. TIPS-pentacene quickly forms into relatively large crystals after deposition. Figure 4-12 shows the transfer characteristics of two representative OTFTs post-annealed at 80 °C and

160 °C. Table 4-1 shows their average OTFT parameters. Device performance is low as the process was not optimized and all fabrication steps were performed under atmospheric conditions. As can be seen in Table 4-1, the device performance is better for the devices post-annealed at 160 °C, which is in agreement with our results obtained from OTFTs with PDBPyBT.

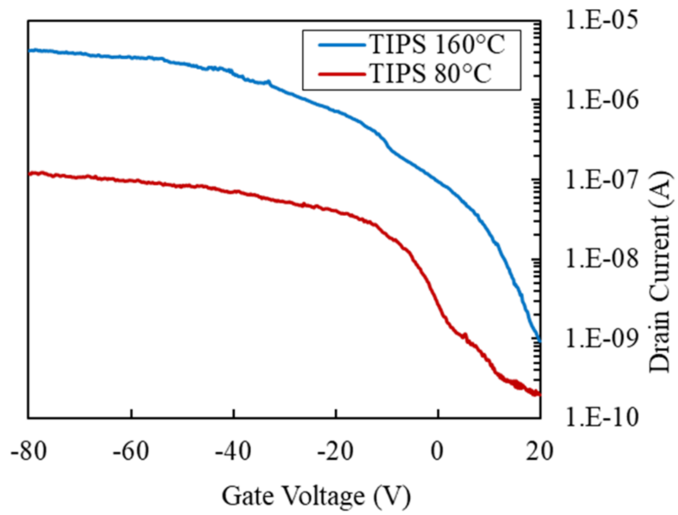

Figure 4-12. The transfer characteristics of two devices post-annealed at 80 °C and 160 °C at V_d = -120 V. The channel length and dielectric thickness were 20 µm and, and 300 nm, respectively.

Table 4-1. The average TIPS-pentacene OTFT parameters for devices post-annealed at 80 °C and 160 °C. The results are in agreement with data obtained from OTFTs with PDBPyBT.

Post-annealing Temperature (°C)	Saturation Mobility (cm^2/V.s)	Ion/(W/L) (A)	Ioff (A)	Ion/Ioff
80	4.26E-04	2.15E-09	1.79E-10	8.87E+02
160	7.07E-03	7.61E-08	4.13E-08	5.14E+03

4.6. Surface morphology: roughness measurement through atomic force microscopy (AFM)

Wettability is a factor that needs to be characterized alongside roughness [119]. Contact angle hysteresis is mainly the result of surface roughness. The roughness size can be in the micrometer [120] or nanometer range [121]. Experiments and simulations show that even atomic-scale roughness can lead to contact angle hysteresis [122]. Both peak-to-peak and average roughness (root mean square (RMS)) of the Teflon-AF films before and after plasma treatment and after post-annealing were measured and are presented in Figure 4-13. The roughness of the Teflon-AF films and the thickness and roughness of the OSC layers were measured with a Multimode 8 scanning probe microscope (SPM). The imaging mode was ScanAssist-air. Each error bar was calculated using 12-18 data points obtained from different samples and different spots on the same sample. Both roughness measurements increase after plasma treatment from 0.63 nm to 1.25 nm and from 4.61 nm to 8.28 nm for average and peak-to-peak roughness, respectively. They decrease after post-annealing at 80 °C to 1.1 nm and 7.97 nm for the average and peak-to-peak roughness, respectively. They continue to decrease slowly to 0.67 nm and 4.97 nm, respectively, at 200 °C. Both these roughness values help build a better understanding of how the surface morphology of the films changes through the plasma and post-annealing steps. To have a complete understanding of the surface roughness, the AFM images representing each step are shown in Figure 4-14. Interestingly, after post-annealing the films, grain-like structures appear on the surface, and then by increasing the temperature, this grain-like structure disappears and the films become smooth again. The films start smoothing at 160 °C, which is the glass transition temperature (T_g) of the material. The decreasing surface roughness may explain the gradual increase in the on-current and saturation field-effect mobility with increasing post-annealing temperature (Figure 4-5a and c).

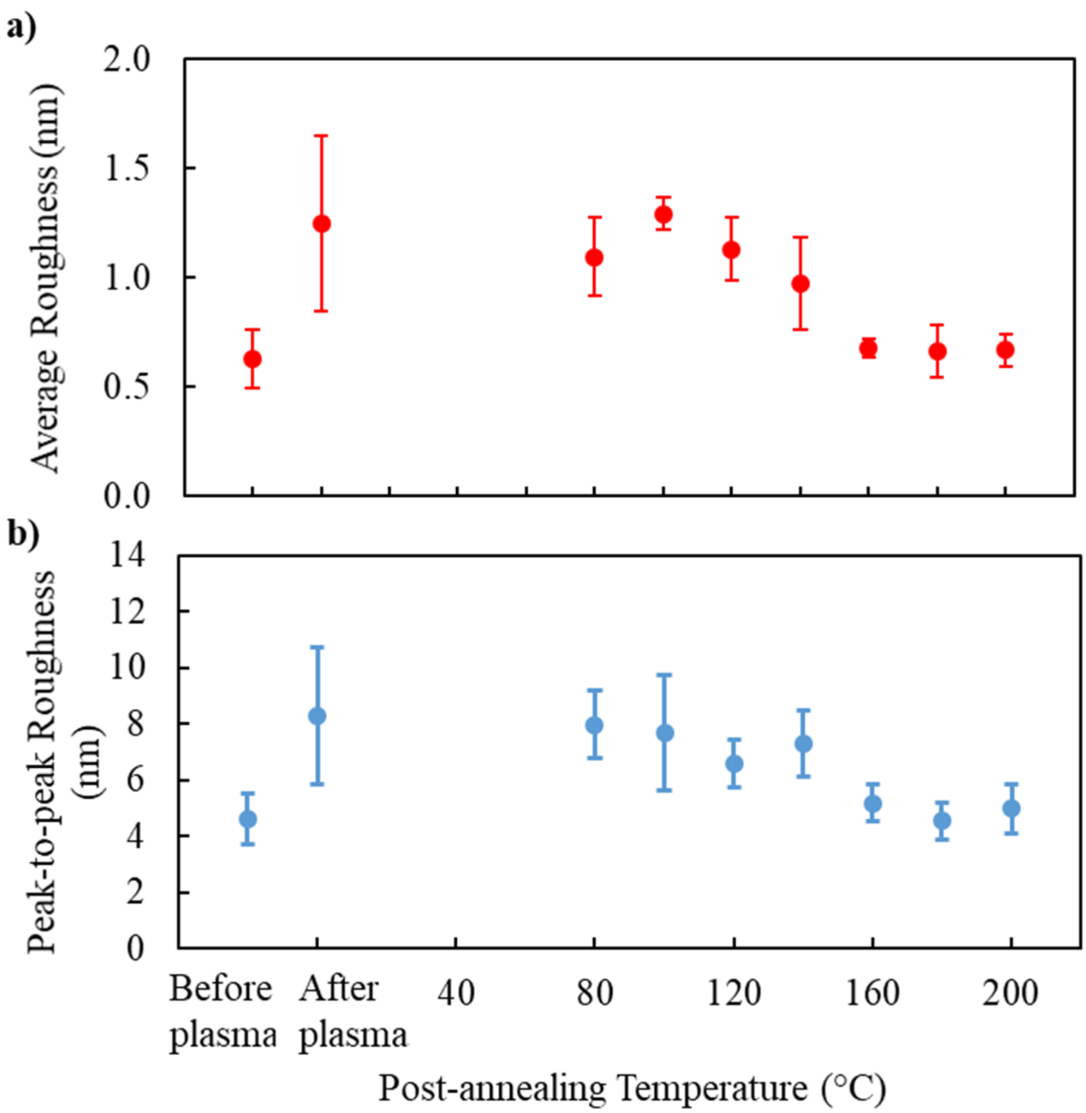

Figure 4-13. (a) Average and (b) peak-to-peak roughness of Teflon-AF films before and after plasma treatment and after post-annealing. Both roughness values increase after plasma treatment and decrease after post-annealing. At 200 °C, they approach their value before plasma treatment.

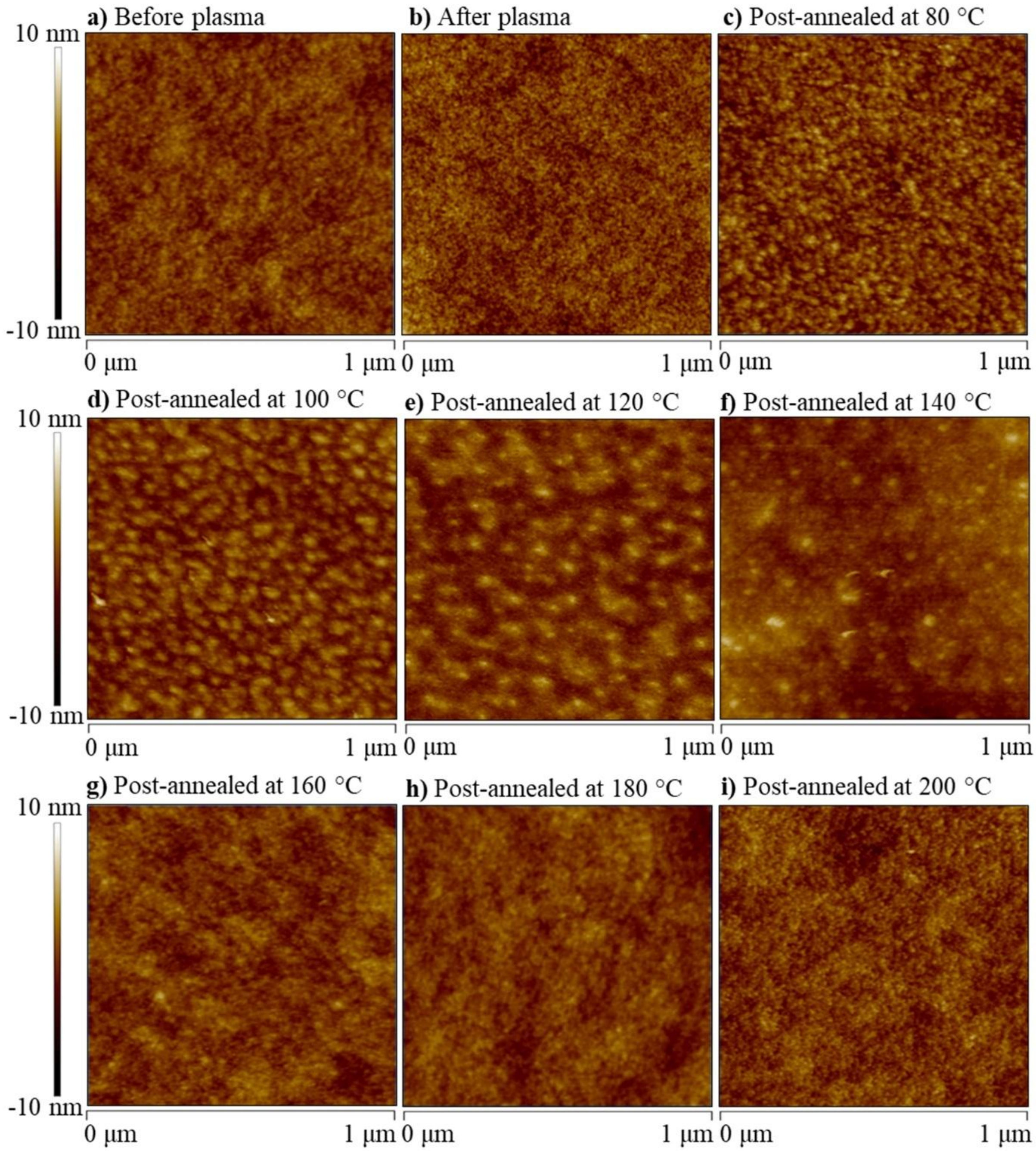

Figure 4-14. AFM images of the Teflon-AF films (a) before plasma, (b) after plasma, post-annealed at (c) 80 °C, (d) 100 °C, (e) 120 °C, (f) 140 °C, (g) 160 °C, (h) 180 °C, and (i) 200 °C.

It is well known that higher roughness causes a disordered structure in the OSC at the interface [123]. A smoother dielectric surface causes the formation of larger OSC grains at the interface, which leads to improved charge transport and field-effect mobility [124,125]. The average roughness data and AFM images of the OSC for different post-annealing temperature are shown in Figure 4-15 and Figure 4-16, respectively. The OSC roughness increases with increasing post-annealing temperature which indicates the increase of OSC grain size. The decrease in the CA hysteresis at high post-annealing temperatures with decreasing roughness matches well with theory. According to the Wenzel model, on hydrophobic surfaces, when the droplet is receding, larger roughness pins the contact line trying to stop the liquid from retracting, therefore, leading to a larger CA hysteresis [126–128]. However, the decrease in advancing contact angle after plasma cannot be understood in terms of surface roughness and the chemistry of the surface needs to be considered.

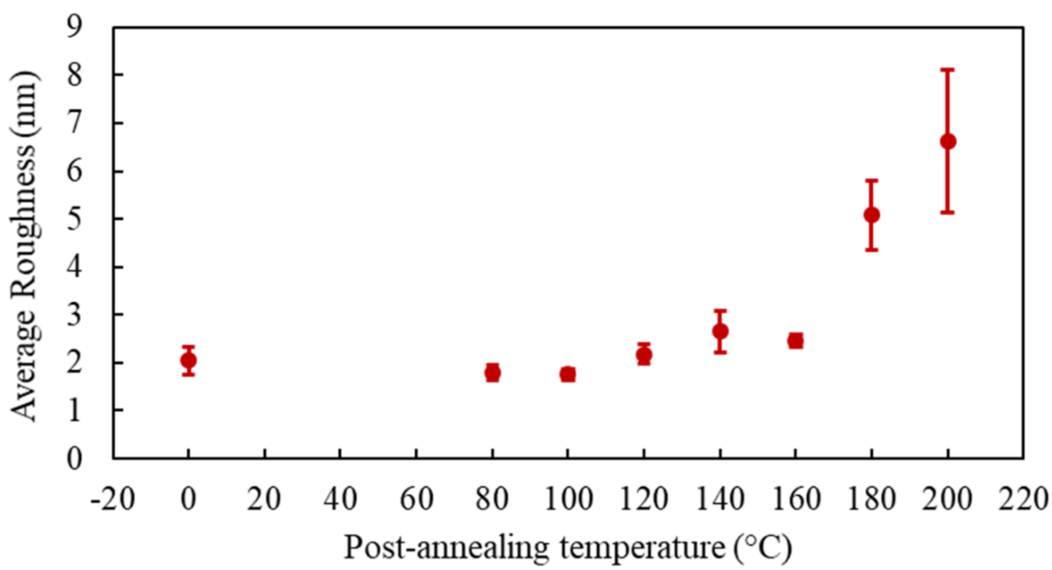

Figure 4-15. Organic Semiconductor (OSC) average roughness (RMS) versus post-annealing temperature. It shows an increasing trend.

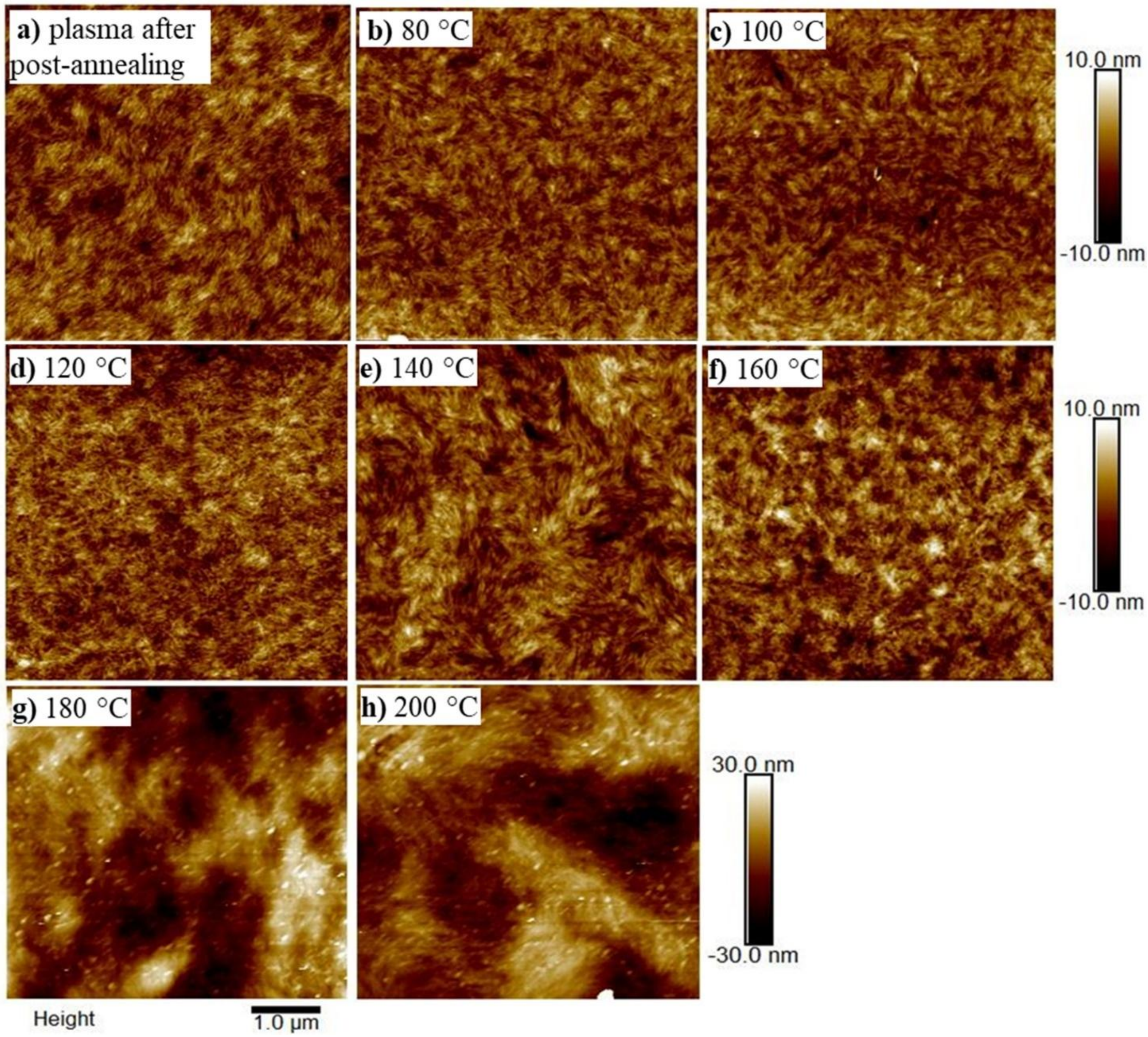

Figure 4-16. AFM images of the organic semiconductor on Teflon-AF (a) plasma treated after post-annealing (0 °C), post-annealed at (b) 80 °C, (c) 100 °C, (d) 120 °C, (e) 140 °C, (f) 160 °C, (g) 180 °C, and (h) 200 °C. Note that the scale of the scans is larger for 180 °C and 200 °C due to the dewetting and large roughness of the OSC.

4.7. Bulk chemistry

This section delves into the evaluation of the bulk dielectric properties of Teflon-AF as a function of post-annealing temperature, utilizing metal-insulator-metal (MIM) capacitors as the test structure, and FTIR spectroscopy.

4.7.1. Dielectric evaluation

First, MIM (metal-insulator-metal) capacitors were fabricated to evaluate the dielectric properties of Teflon-AF. MIM capacitors are a classic structure used to assess the dielectric properties of materials. These capacitors consist of two metal electrodes separated by an insulating layer, which in this case is Teflon-AF. Capacitance values of Teflon-AF post-annealed at different temperatures are measured to study the performance of the material as an insulator in electronic devices.

The geometry of the MIM capacitors, breakdown electric field, and capacitance versus frequency are shown in Figure 4-17. The breakdown electric field shows the maximum electric field the dielectric can withstand before it fails, which is indicative of the material's robustness and reliability.

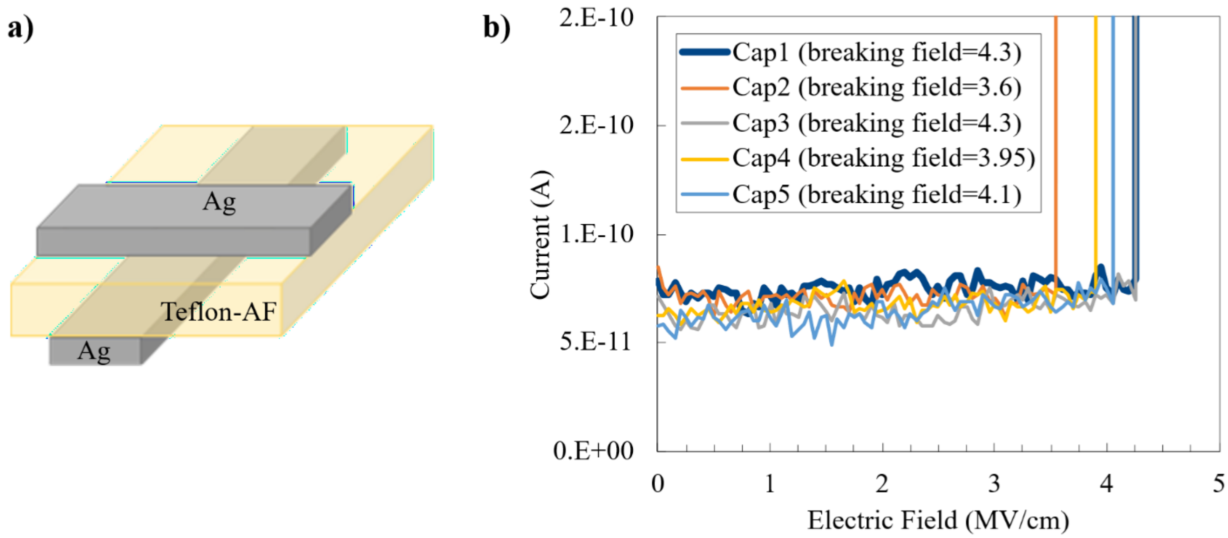

Figure 4-17. (a) Capacitance schematics, and (b) current versus electric field, the breakdown electric field is around 4 MV/cm.

Figure 4-18 shows capacitance versus log of frequency for post-annealing temperatures of 80 °C, 120 °C and 200 °C. Therefore, the dielectric capacitance of Teflon-AF does not change with post-annealing temperature. The results, as depicted in the figures, show that the average capacitance and the dielectric constant remain constant at about 3.5 nF/cm² and 1.83 ± 0.07, respectively, across all post-annealing temperatures. This indicates that the bulk dielectric properties of Teflon-AF, specifically the dielectric constant, are stable across the range of temperatures investigated. This stability is crucial for applications where the dielectric layer needs to perform consistently under different thermal conditions.

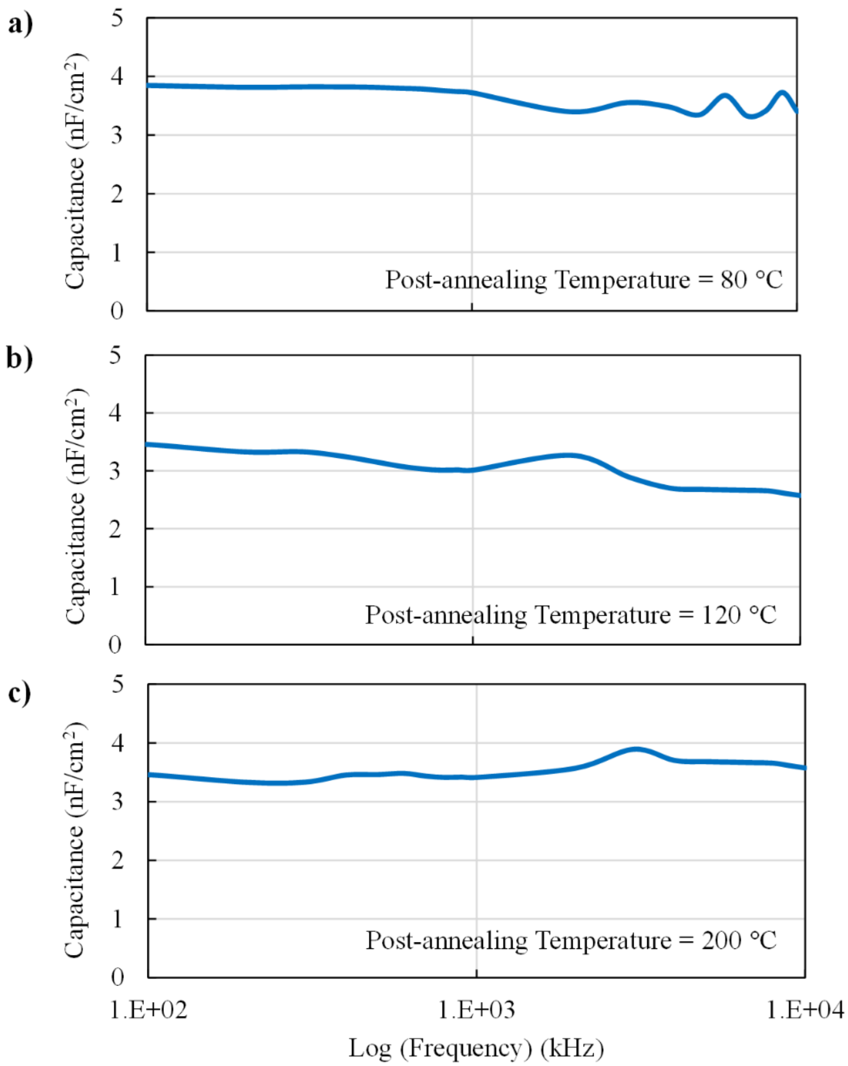

Figure 4-18. Capacitance versus log of frequency for post-annealing temperatures of 80 °C, 120 °C and 200 °C.

4.7.2. FTIR spectroscopy

Next, FTIR spectroscopy is used to investigate the possible effect of post-annealing temperature on the dielectric bulk properties. Attenuated total reflection (ATR) is a powerful analytical technique used to determine the molecular composition and chemical bonding in materials. In this context, ATR-FTIR spectroscopy was employed to examine the Teflon-AF samples, utilizing a Vertex 70v FTIR spectrometer. The measurements were conducted in absorption mode, meaning the instrument measures the intensity of the IR radiation absorbed by the sample at various wavelengths, converting it into a spectrum representing molecular vibrations. The spectra are studied to ascertain whether any changes in the bulk material occurred, which would be indicated by shifts or changes in intensity of the characteristic absorption peaks.

The spectrum for the Teflon-AF solution is presented in Figure 4-19a. The main peaks at 1094 cm^{-1}, 1241 cm^{-1}, 1268 cm^{-1}, and 1305 cm^{-1} represent the fluorinated dioxole group and the peak at 725 cm^{-1} shows the amorphous structure of the material [129,130]. Figure 4-19b-e show the spectra for Teflon-AF films before and after plasma-treatment, post-annealed at 120 °C and 200 °C, respectively. These two specific temperatures represent samples post-annealed below and above the glass transition temperature (Tg). The film spectra have the perfluoromethyl end-group -CF3 peaks at 981 cm^{-1}, which does not appear in the solution spectrum [37,129]. This -CF3 end-group has been reported to appear in the spectra for amorphous Teflon-AF powders and films that are not too thin [129]. The lack of significant changes in the characteristic peaks across the film spectra suggests that the plasma treatment and subsequent annealing at 120 °C and 200 °C, below and above Tg of Teflon-AF, did not alter the bulk structure of the polymer. This observation is consistent with previous findings indicating the good thermal stability of Teflon-AF 1600 below 400 °C [131].

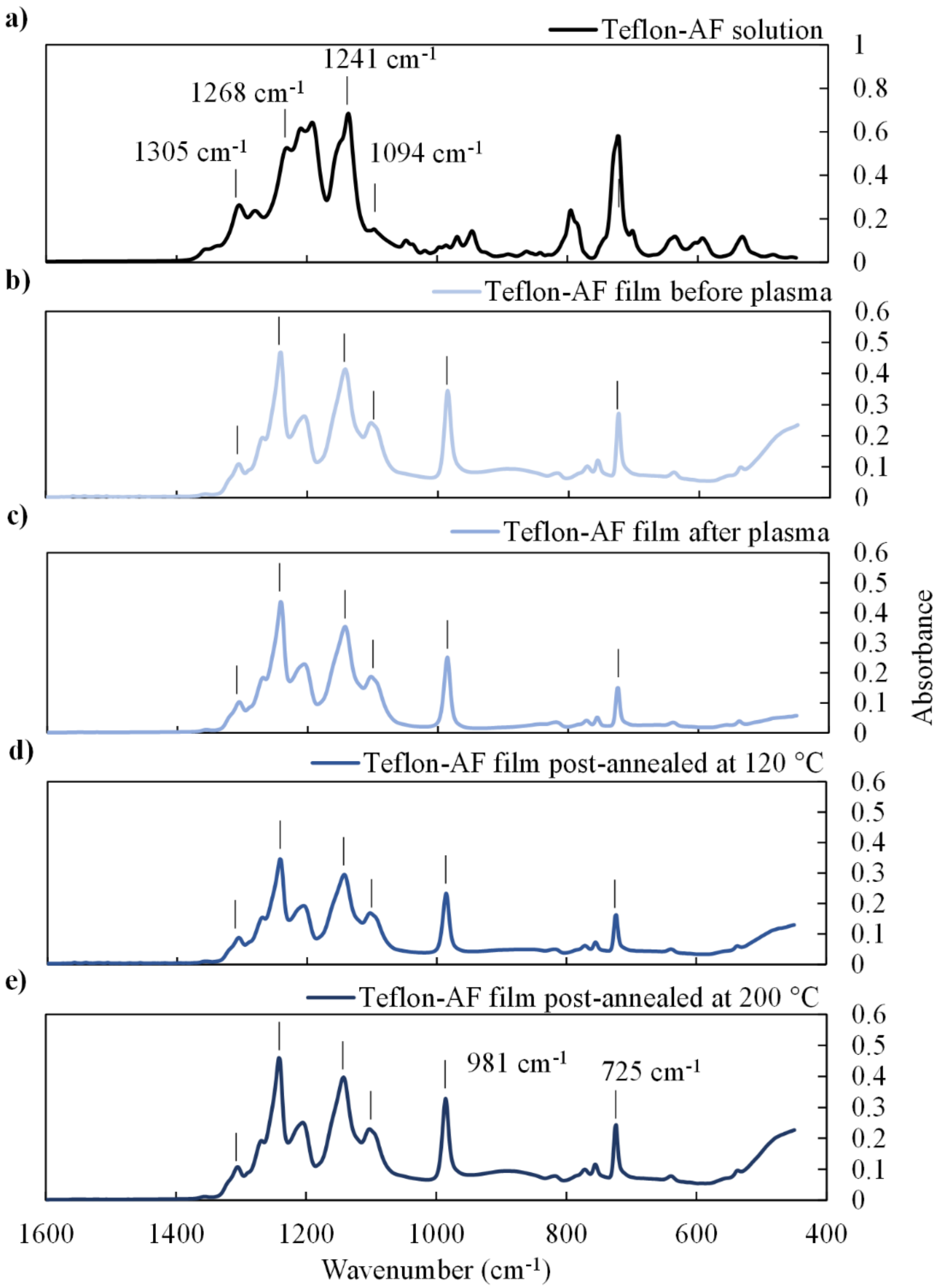

Figure 4-19. FTIR spectra for Teflon-AF samples (a) in solution form, and as a film (b) before plasma, (c) after plasma, and post-annealed at (d) 120 °C, and (e) 200 °C. Film spectra do not show significant differences for different treatments.

4.8. Surface chemistry: XPS measurements

Another explanation for the change in contact angle hysteresis after plasma treatment and after post-annealing could be changes in the surface chemistry of the Teflon-AF films. In this section, the chemical composition of the surface is investigated using XPS to identify the chemical bonds that are intensified or weakened in each post-annealing step. The survey spectra were obtained from a K-Alpha XPS spectrometer. They were also repeated with ESCALAN 250Xi. The energy scale was adjusted to place the carbon main peak (C-C) at 285 eV. The survey spectra include F 1s, O 1s, C 1s, and N 1s (weak) regions. Table 4-2 shows the change in the atomic percentage of the different elements. The total atomic percentages of fluorine atoms decrease after plasma treatment but increase after post-annealing. Conversely, the atomic percentages of oxygen, carbon, and nitrogen atoms increase after air plasma treatment but decrease after post-annealing.

Table 4-2. Atomic percentages of O, F, C, and N before and after plasma and with annealing.

Atomic %					
	Before Plasma	After Plasma	80 °C	160 °C	200 °C
O 1s	10.6	11.9	11.6	10.7	10.8
F 1s	58.0	55.6	55.8	57.5	57.6
C 1s	31.4	32.5	32.6	31.7	31.5
N1s	0.0	0.4	0.3	0.1	0.0

The XPS results are explained by looking at higher-resolution scans for different regions observed in the survey spectrum for the Teflon-AF surface. See Figure 4-20.

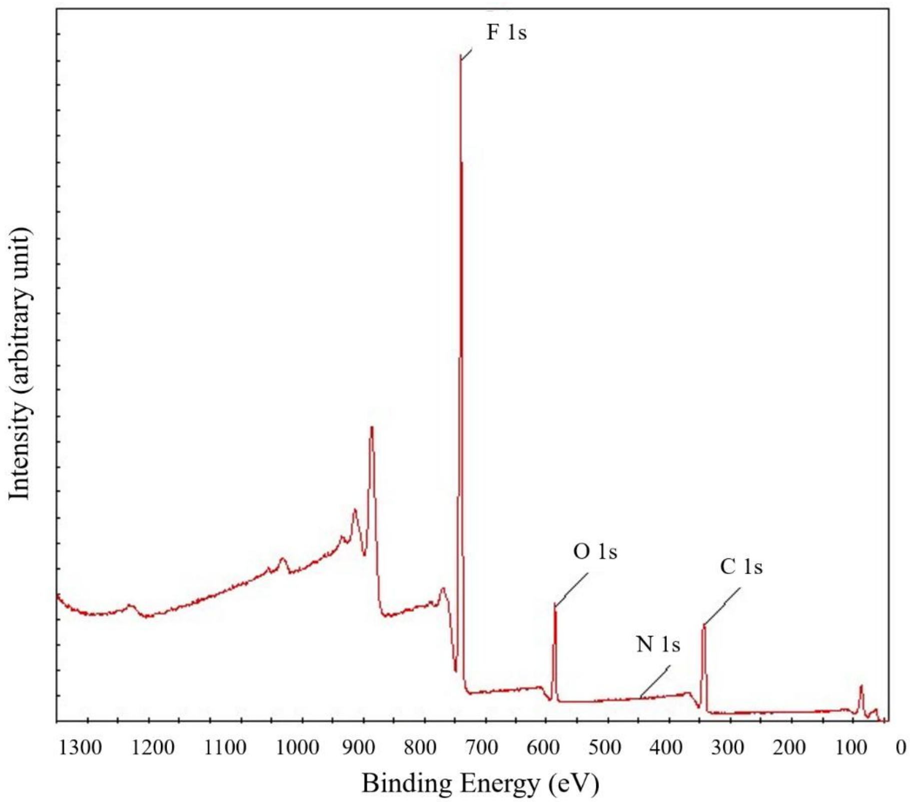

Figure 4-20. XPS survey spectrum for Teflon-AF after plasma treatment

C 1s Region:

The C 1s region represents the binding energies of the core electrons in the carbon atoms. The core-level peaks in the C 1s region occur at the binding energies of 292 eV, 294.3 eV, 295.2 eV, 282 eV, 286.9 eV and 288.6 eV. These binding energies correspond to the following bonds:

- CF2 Bonds (292 eV)[41,132,133]: The peak at 292 eV corresponds to the carbon atoms bonded to two fluorine atoms. This is a characteristic peak of the fluoropolymer backbone.

- CF3 Bonds (294.3 eV)[41,132–135]: The peak at 294.3 eV is indicative of carbon atoms bonded to three fluorine atoms, typically found at the end of a polymer chain.
- O-C-O Bonds (295.2 eV) [136]: The presence of a peak at 295.2 eV suggests the existence of O-C-O bonds within the polymer or on the surface after plasma treatment.
- C-C[132,135]/C-H[132,133] Bonds (282 eV, 286.9 eV): These peaks are attributed to carbon-carbon (C-C) or carbon-hydrogen (C-H) bonds, indicative of non-fluorinated regions or contaminants.
- C-O Bonds (288.6 eV)[135]: The peak at 288.6 eV represents carbon-oxygen single bonds, possibly due to the introduction of alcohol or other oxygen-containing groups during plasma treatment.
- CF-CF Bonds (288.6 eV)[133]: This peak indicates the presence of carbon-fluorine bonds which is part of the Teflon-AF polymer structure.

F 1s Region:

The F 1s region is specific to the binding energy of core electrons in fluorine atoms. The F 1s region of the spectra for the different conditions reveal the following bonds for the core-level peaks at 689.1 eV and 691.1 eV:

- C-F Bonds (689.1 eV)[135]: A peak in this region signifies the presence of single carbon-fluorine bonds.
- CF2-CF2 Bonds (691.1 eV)[137]: A peak here points to a difluorinated carbon adjacent to another difluorinated carbon, a characteristic structure within the Teflon-AF polymer.

O 1s Region:

The O 1s region reflects the binding energy of core electrons in oxygen atoms. In the O 1s region, the peaks at 533.4 eV, 536.1 eV, 531.6 eV, and 537.3 eV represent the following bonds:

- C-O Bonds (533.4 eV)[135]: This peak suggests the presence of carbon-oxygen single bonds.
- O-CFx Bonds (536.1 eV)[41]: This peak likely represents oxygen atoms bonded to carbon atoms that are also bonded to fluorine, indicative of the fluoropolymer surface that has been oxidized or modified.
- C-O-O Bonds (531.6 eV)[135]: The peak at this energy is associated with peroxide or other similar oxygen-oxygen linkages.
- O-C-O Bonds (537.3 eV)[138,139]: This is another indication of the presence of O-C-O bonds on the surface.

N 1s Region:

Finally, in the N 1s region, the peaks correspond to the binding energy of core electrons in nitrogen atoms. The weak peak at 402.5 eV in the N 1s region indicates the appearance of the following bond after plasma treatment:

- C-N bonds (402.5 eV)[140]: The appearance of this peak post-plasma treatment suggests the introduction of nitrogen-containing groups, possibly from the air plasma, as nitrogen is a major component of air.

The C 1s, O 1s and F 1s spectra for the different conditions are shown in Figure 4-21. The main peaks being distinguished with dashed lines specifying the main peaks at 292 eV and 294.3 eV for C 1s, 536.1 eV for O 1s, and 689.1 eV for F 1s regions. For all the three regions, plasma treatment and post-annealing cause shifts to the peak positions while at the highest post-annealing temperature (200 °C) the peaks return to their position before plasma treatment.

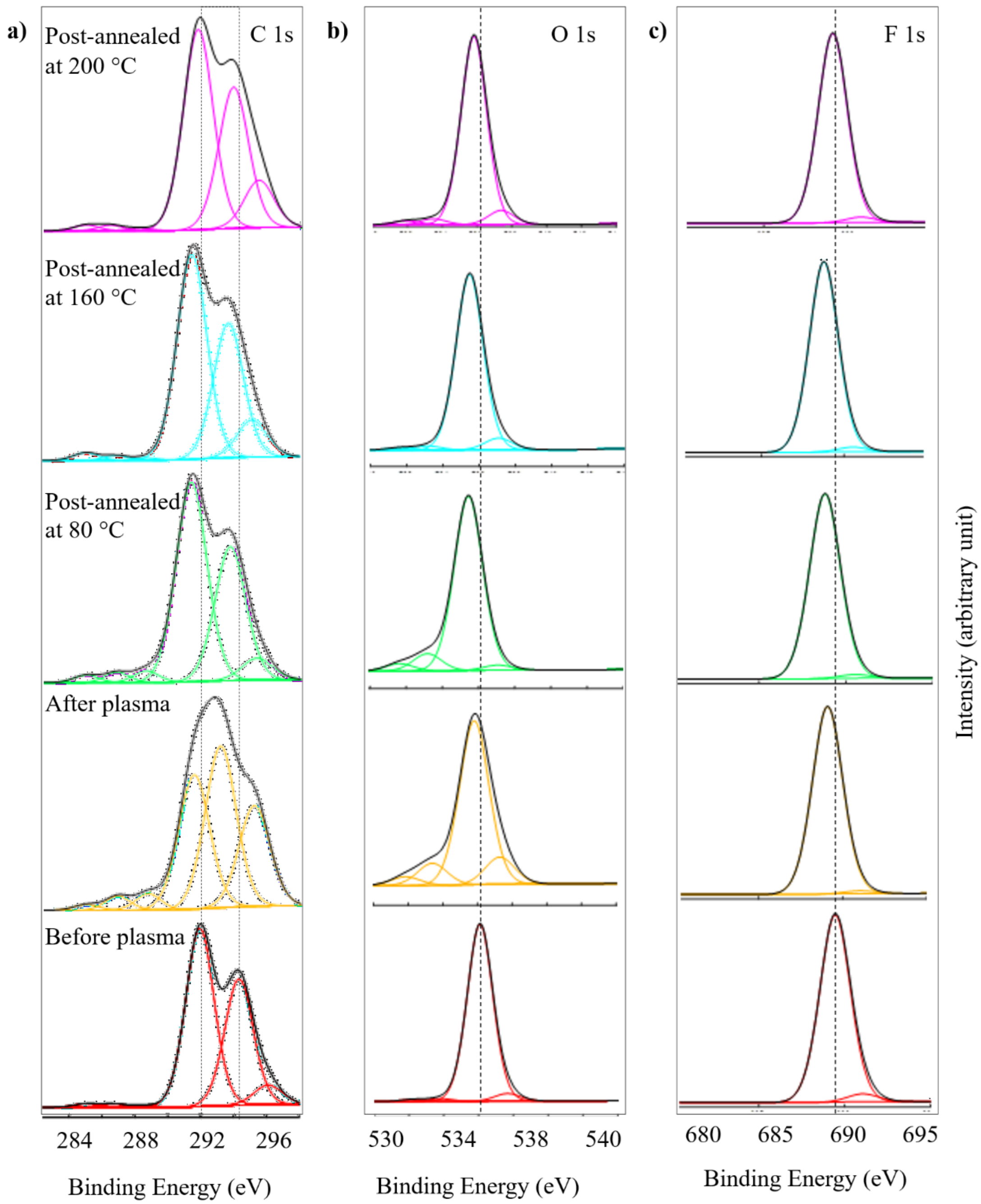

Figure 4-21. XPS survey spectra for (a) C 1s, (b) O 1s, and (c) F 1s regions for different conditions, with the dashed lines specifying the main peaks at 292 eV and 294.3 eV for C 1s, 536.1 eV for O 1s, and 689.1 eV for F 1s regions.

The changes in the concentration of the main bonds are plotted in Figure 4-22, to show the clear trend of chemical change on the Teflon-AF surface. Table 4-3 provides the atomic percentage of different elements corresponding to the bonds present on the surface. The percentage of fluorine-containing CF2 (292 eV) and C-F (689.1 eV) bonds decreases after plasma treatment and increases again after post-annealing, while the percentage of oxygen-containing O-C-O (295.2 eV) and C-O (533.4 eV) bonds follows the opposite trend.

The change in the concentration of elements after plasma treatment and after post-annealing could be explained with two complementary scenarios. One, bonds containing oxygen and nitrogen form after plasma treatment. After post-annealing, these plasma-produced bonds dissociate, and fluorine-containing bonds reform [131]. Two, as has been suggested by Ref. [135], an overlayer containing air-plasma-produced oxygen and nitrogen atoms appears after plasma treatment, which covers the fluorinated surface of Teflon-AF, and reduces photoemission from the film underneath. Here, this overlayer is removed after the subsequent post-annealing step through a mechanism called surface adaptation. Surface adaptation, which is the continuous motion of the polymer chains from the surface to the bulk, has been observed in the ageing of PTFE films [36]. Both of these scenarios could explain the elemental percentage changes observed here. Bonds such as CF2 (292 eV), show a higher percentage change from 16.8% to 10.2% after plasma treatment and back to 15.7% after post annealing, also O-C-O (295.2 eV), which changes from 1.8% to 7.7% and back to 3.7%. The change in some other bonds is smaller. For instance, C-F (689.1 eV) decreases from 55.6% to 54.7% after plasma treatment and increases back to 56% after post-annealing (Figure 4-22c). The shift in V_t with increasing post-annealing temperature (Figure 4-4b and Figure 4-5e) can be explained by the change in the oxygen content on the Teflon-AF surface. Oxygen plasma treatment shifts the threshold voltage to more positive values by introducing electron trapping sites at the interface [141,142]. Right after plasma treatment, V_t is -2 V, and it becomes more negative after post-annealing reaching -22 V at 200 °C. The post-annealing reverses the positive V_t shift due to the oxygen plasma. It is true that fluorine atoms have high electronegativity, and they can cause the trapping of electrons on the dielectric surface [110], but here we do not see a corresponding positive V_t shift with post-annealing.

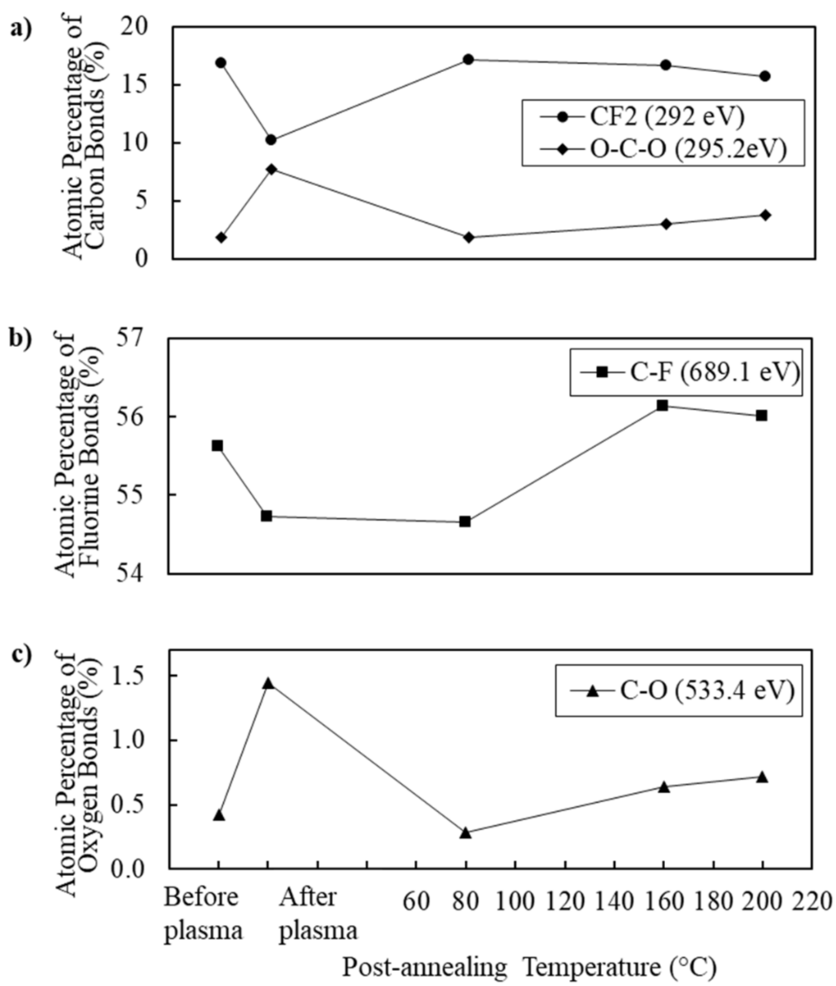

Figure 4-22. The change in the percentages of the CF2, O-C-C, C-F, and C-O bonds.

Table 4-3. Percentages of chemical bonds measured by XPS

			Atomic %				
Element	**Bonding Type**	**Binding Energy (eV)**	**Before Plasma**	**After Plasma**	**80 °C**	**160 °C**	**200 °C**
C 1s	CF2	292	16.81	10.23	17.13	16.67	15.74
	CF3	294.3	11.93	12.30	11.48	10.95	11.08
	O-C-O	295.2	1.83	7.67	1.88	3.01	3.72
	C-C or C-H	282	0.31	0.36	0.53	0.52	0.38
	C-O	286.9	0.29	0.87	0.71	0.32	0.36
	CF-CF	288.6	0.18	1.02	0.82	0.17	0.17
F 1s	C-F	689.1	55.62	54.72	54.66	56.14	56.01
	CF2-CF2	691.1	2.33	0.83	1.09	1.31	1.54
O 1s	C-O	533.4	0.42	1.44	0.28	0.64	0.71
	O-CF_x	536.1	9.86	8.77	9.87	9.66	9.55
	C-O-O	531.6	0.12	0.47	0.43	0.14	0.21
	O-C-O	537.3	0.17	1.19	0.99	0.23	0.30
N 1s	C-N	402.5	0.00	0.10	0.30	0.40	0.00

We believe that the post-annealing step at elevated temperature resembles an accelerated ageing process where surface adaptation along with reformation of bonds at the surface cause the reversibility of films after post-annealing. The increase in advancing CA and decrease in CA hysteresis with post-annealing temperature shown in Figure 4-9 is therefore explained by the decrease in the percentage of reactive elements such as oxygen and the increase in the percentage of hydrophobic fluorine content on the surface. The lower percentage of reactive elements ensures a better OSC/dielectric interface with fewer trap sites, hence better OTFT performance. This also partly explains the improved OTFT performance for devices post-annealed below 180 °C, above which the OSC accumulates non-uniformly between the electrodes.

4.9. Conclusions

In this chapter, OTFTs with inkjet-printed electrodes on hydrophobic fluoropolymer gate dielectric were fabricated. Plasma treatment was used to increase the wettability of the fluoropolymer. However, printing and annealing of the electrodes add complications to the gate dielectric/ OSC interface that have not been studied before. We show that surface reversibility of Teflon-AF changes the morphological and chemical properties on the surface after plasma treatment and after subsequent post-annealing at different temperatures. The contact angle hysteresis and surface roughness increase and reactive elements appear on the surface after plasma treatment. However, after post-annealing, the opposite trend is observed. The reactive elements disappear and the random roughness on the surface changes to ordered grain-like structures with increasing post-annealing temperature from 80 °C to 140 °C. At 160 °C, the surface starts smoothing and at 200 °C it changes back to the state before plasma treatment. Hence, at the right temperature, the desired wettability, roughness, and percentage of chemical bonds can be achieved. At this temperature

(160 °C), OTFT parameters such as field-effect mobility and on-off current ratio are maximized. To prove that the OSC/ dielectric interface is the dominant factor rather than contact resistance, we extracted the contact resistance and low-field mobility. The low-field mobility that is independent of contact resistance shows a clear trend with post-annealing temperature. Low-field mobility is increased by a factor of approximately five from 80 °C to 160 °C post-annealing temperature, leading to improved transistor performance. Overall, the analysis indicates that the post-annealing step functions akin to an accelerated aging process for Teflon-AF films. It facilitates the recovery of the surface's hydrophobic characteristics and reversibility after plasma treatment, enhancing the quality of the OSC/dielectric interface and thereby improving the performance of OTFT devices. These insights into the relationship between surface chemistry and electrical properties are crucial for the development of robust and reliable electronic components.

Printing conductive inks on inherently hydrophobic surfaces like Teflon-AF is challenging due to poor wetting and adhesion. This problem was tackled by using plasma treatment to temporarily increase the surface energy of Teflon-AF, improving the adhesion and wetting of the printed ink. Post-annealing was shown to influence the morphology and roughness of the layers, which in turn affects the device performance. The study managed to use post-annealing to reduce the roughness and improve the morphology of Teflon-AF.

By addressing these challenges, the study contributed to advancing the field of printed electronics, particularly in the fabrication of OTFTs, by demonstrating control over the physical and chemical properties of materials through treatment processes, thus improving device performance and reliability. In the next chapter, another printed electronics challenge will be addressed by depositing and engineering carbon nanotubes in the channel of TFTs though inkjet printing.

Chapter 5: Inkjet-printed transistors with coffee ring aligned carbon nanotubes

This chapter was published in Flexible and Printed Electronics journal, Copyright IOP Publishing.

Naderi P, Grau G. Inkjet-printed transistors with coffee ring aligned carbon nanotubes. Flexible and Printed Electronics. 2024 Mar 1;9(1):015001, https://doi.org/10.1088/2058-8585/ad1ccf.

5.1. Introduction

In the previous chapter, transistor source and drain electrodes were inkjet-printed on a plasma treated hydrophobic surface. Their annealing imposed a second annealing step on the dielectric surface which caused changes in the OSC/dielectric interface. In this chapter, inkjet printing is used to deposit and engineer the channel material in TFTs.

Inkjet printing is widely considered as a promising technique to deposit CNT inks for the channel of TFTs.[47,48] As-grown CNTs have a large number of metallic tubes, whereas CNT inks with high semiconducting percentage have been successfully formulated.[55,56] CNT inks have been deposited as thin films using inkjet printing to make TFTs[10,48–50], strain and chemical sensors[51,52], and conductive films[53,54]. When choosing the proper deposition technique for CNTs in TFT channels, one usually needs to compromise between high mobility and high on-off current ratio. High-density solution processing techniques such as drop casting[60] and spin-coating[61] lead to high field-effect mobilities and low on-off current ratio, while low-density techniques such as spray-coating[8,62] and inkjet printing,[63,64] in general, lead to higher on-off current ratio at the cost of lowering the field-effect mobility. Additionally, it is difficult to maintain both high transistor current and low leakage current with any deposition technique.[59] The performance of CNT TFTs improves by regulating CNTs inside the TFT channel using solution processing techniques. [57–59] With inkjet printing, CNTs can be aligned on droplet edges as a result of capillary flow.[53,69] Tilted drop-casting causes the CNTs to exhibit liquid crystal behavior in the vicinity of the receding contact line, which causes regulated bundles of CNTs to form due to the high local concentration of CNTs.[57] Modulating the density of CNTs by inkjet printing fewer number of layers in the channel region closer to the source and drain electrodes lowers the energy barrier for injection of electrons.[59]

Generally, film thickness non-uniformity is avoided when a layer is solution-processed for a device.[23,24] The coffee ring effect is a major challenge when forming films from solutions. The coffee ring is the ring-shaped pattern that is left around the edge of printed patterns after the solvent evaporates. During the evaporation process, the edge of the droplet evaporates faster. The contact line, which is the interface of the solid, liquid and the surrounding vapor, is pinned. The contact line tends to stay pinned, therefore, the loss of solvent is compensated by liquid flowing from center to the edges. As a result, this capillary flow takes most of the solute to the edges.[22] In the case of lines, the pattern will be linear instead of circular. Researchers have been working on removing the coffee ring effect in CNT TFTs, since it causes the aggregation of the tubes on the edges of the printed pattern.[143,144] One way to eliminate it is by eliminating the pinning, for instance by using a non-wetting substrate[65], or reversing the capillary flow by using a mixed solvent system.[66–68] At the same time, careful control over squeezing CNTs at desirable locations can help regulate their position and film morphology in the TFT channel. The performance of CNT TFTs improves by regulating CNTs inside the TFT channel using solution processing techniques. [57–59]

As coffee ring effect naturally happens after the film has formed, utilizing it will obviate the requirement for surface treatment[28] or the use of multiple solvents to reverse capillary flow[36]. Therefore, it is more convenient and agrees well with the nature of inexpensive solution processed printed electronics to engineer and utilize this effect.

In this chapter, we present CNT TFTs with an inkjet-printed CNT channel. With drop-on-demand (DOD) inkjet printing, lines with controlled morphologies were printed on a Si/SiO_2 wafer. Inkjet printing parameters were varied to manipulate the formation of coffee ring effect in the channel of the TFTs. When separate lines are printed, due to the coffee ring effect, thicker edges are formed while connected lines dry uniformly with random puddles formed in the pattern. Transistor I-V characteristics and contact resistance at the CNT/metal interfaces are studied. Thickness profiles and atomic force microscopy (AFM) images of the printed CNT channels show tube configurations in the CNT networks that explain the device behavior.

5.2. CNT TFT fabrication process

Before presenting the results and discussion, first, the transistor fabrication process is described in multiple steps: substrate preparation, inkjet printing of the CNT channel, and the inkjet printing of the source and drain electrodes. In the next section, the formation and control of the coffee ring effect in the printed CNT channels are discussed.

5.2.1. Substrate preparation

P-type silicon wafers with a 300 nm oxide layer (University Wafers, Inc., South Boston, USA) were used as substrates with the p^{++} silicon as the gate electrode. The silicon wafers were cut and sonicated in isopropanol, acetone, and deionized (DI) water each for 10 min. Next, they were dried with air and were plasma treated at 50 W for 1 min. Prior to CNT printing, the surface was functionalized by drop-casting Poly-L-Lysine (0.1% w/v in water, Sigma Aldrich, Canada) for 5 min, followed by rinsing with DI water, drying with air, and storing in a desiccator for 20 min. Poly-L-Lysine (PLL) is commonly used to increase the adhesion of solution processed carbon nanotubes to the surface of silicon dioxide (SiO_2).[12,145–147] PLL is a biocompatible polymer with a positive charge. When it is applied to an SiO_2 surface, it forms a stable layer by adsorbing to the negatively charged SiO_2 present on the surface. The interaction between the positively charged amino groups in PLL and the negatively charged oxide groups on SiO_2 leads to the formation of a self-assembled monolayer (SAM) or surface coating. CNTs often tend to agglomerate or not adhere well to surfaces due to their unique physical properties. The positively charged PLL can interact with the negatively charged portions of CNTs, improving their adhesion to the modified SiO_2 surface while ensuring an even adhesion of the CNTs to the surface. After CNT deposition, we rinse the samples to remove excess CNTs and only leave a thin CNT layer for optimal device performance. Without PLL, this would not be possible and all CNTs would be washed off.

5.2.2. Inkjet printing CNT channel

The CNT solution with a 1 mg/mL concentration and 99.9% semiconducting tubes (Isonanotubes-S, NanoIntegris Technologies, Inc., Quebec, Canada) was used as purchased without further dilution. A custom-built inkjet printer with a 60 µm diameter nozzle (Microfab Technologies, Inc. Plano, TX) was used. Next, they were rinsed with DI water, dried and finally annealed at 100 ºC for 30 min. In the case of two-pass prints, after this step, a second pass was printed with lines offset by half the line spacing to ensure the coffee ring was located between the coffee ring lines of the first pass printed lines, followed by rinsing and annealing in the same way. As a control, the CNT solution was also drop-cast on the as-cleaned and functionalized silicon substrates for 2 hrs. Then, they were rinsed also, dried and annealed at 100 ºC for 30 min. The printed patterns were stored in a desiccator for 24 hrs.

5.2.2.1. CNT waveform

Dimensionless numbers such as We number and Z number were briefly discussed in the introduction chapter. Z number is used to understand the influence of viscosity on droplet formation. For viscous inks, the Z value is too low, and droplets do not eject from the orifice since viscous forces are dominant over surface tension forces. For low viscosity inks such as the CNT ink used in this work, Z number tends to be high which leads to the formation of satellite droplets. High Z values mean higher inertia forces, indicating that the liquid jet is more prone to breakup due to inertia. Thus, lowering the Z number could contribute to a more stable liquid jet or droplet formation, potentially reducing satellite droplet formation. From equation 1-3,

$$Z = \frac{Re}{We^{1/2}} = \frac{(\gamma \rho a)^{1/2}}{\eta}$$

Often, there are challenges with inkjet printing low-viscosity and high-surface tension inks, like water-based CNT inks. These difficulties can be addressed by optimizing nozzle dimensions, ink properties and waveform parameters.[14,148] The CNT ink used in this work has nanotube concentration of 0.01 mg/mL in a water-based solution. For water, γ, ρ, and η are 72 mN/m, 10^3 kg/m^3, and 10^{-3} Pa.s, respectively. Therefore, with $a = 30\ \mu m$, Z number is roughly 4.6 which is close to the lower limit according to [[149]] that defines the range of $4 < Z < 14$ for printable inks.

For nozzle design, using a smaller nozzle orifice diameter increases capillary pressure to overcome resistance due to surface tension forces of the ink. This helps with the controlled ejection and break-off of ink droplets. However, here we use a 60 µm Microfab nozzle. And since we aim to use a specific ink, ink properties such as viscosity and surface tension also stay unchanged. As a result, the focus is on controlling the ejection parameters through waveform optimization. It is possible to regulate the previously mentioned dimensionless parameters and minimize satellite droplet formation during inkjet printing by adjusting the waveform. The goal is to ensure that the forces contributing to droplet ejection are in a balanced state, promoting stable droplet formation and minimizing the creation of unwanted satellite droplets.

Regarding waveform parameters, the voltage amplitude and pulse duration are critical factors.[14,148] Adjusting the voltage amplitude, typically within the range of 10 V to 30 V, can influence the force applied to the ink meniscus at the nozzle. Higher voltage can assist in overcoming the ink's surface tension, aiding in more reliable droplet formation. Additionally, the pulse duration, which might range from microseconds to a few milliseconds, is crucial.[14,148] Longer pulse durations can provide sufficient energy to break off the droplets consistently, mitigating issues related to high surface tension ink. Adjusting these parameters allows for more precise control over the droplet ejection process, ensuring uniform droplet formation for printing purposes. Figure 5-1 shows three waveforms along with their resulting jetting for CNT ink. In Figure 5-1a and b, a high pulse voltage and a long duration has led to stable jetting. A pulse with a voltage of 23 V, rise and fall time of 12 µs, and dwell and echo time of 40 µs was used to jet the droplets. In Figure 5-1c and d, the duration is reduced to 8 µs which causes the formation of tiny satellite droplets. Finally, Figure

5-1e and f show a waveform and corresponding droplet jetting with 12 μs rise and fall time, but a relatively low pulse voltage, which fails to produce stable ink jetting.

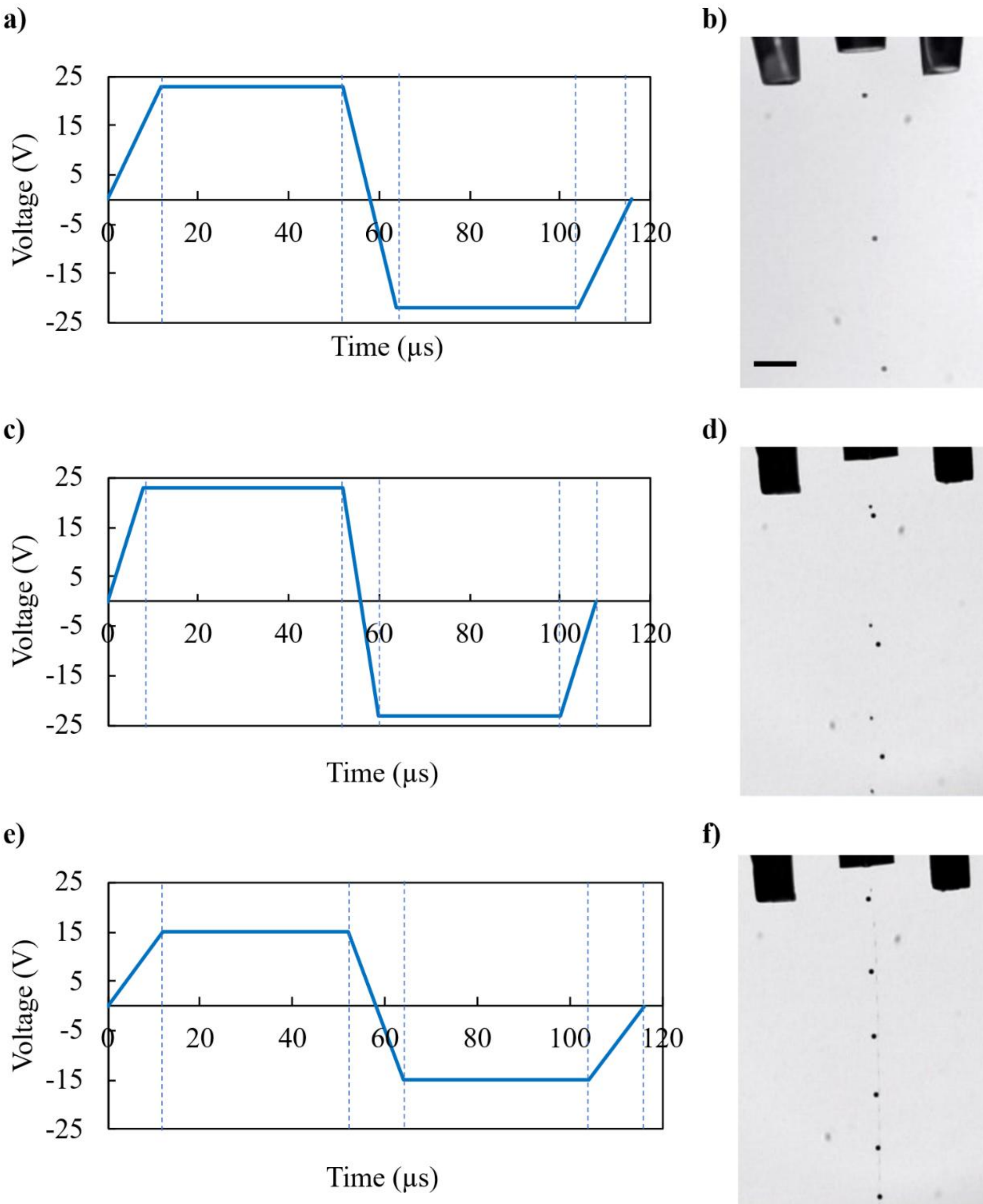

Figure 5-1. Three waveforms along with their resulting jetting for CNT ink. An optimized (a) waveform and (b) its corresponding stable jet. A high pulse voltage and duration has led to a stable

jetting. (c) Waveform with low rise and fall time and (d) its corresponding jetting with satellites. The duration is reduced to 8 μs which causes the formation of tiny satellite droplets. (e) A waveform with 12 μs rise and fall time, but a relatively low pulse voltage, and (f) its corresponding unstable jet with satellite droplets.

5.2.2.2. Inkjet printing CNT line patterns

Parallel lines of the CNT solution were inkjet-printed in the channel of a TFT with a bottom-gate-top-contact device configuration. The reason for adopting a top-contact configuration was that to print the CNT lines and engineer the coffee ring effect in the printed lines, it was necessary to have a flat surface on which the capillary flow has its natural direction toward the edges of the pattern. While in a bottom-contact configuration, the silver electrodes add thickness, roughness, and surface energy variation to the surface, which would disrupt the formation of the CNT coffee ring patterns. During the printing process, the line spacing, number of layers, and the stage speed were varied for each experiment, while the drop spacing was kept constant (90 μm) for all the experiments. The line spacing changes the overall concentration of CNTs inside the channel and it was kept constant for a given number of layers. Figure 5-2 shows the device fabrication process in the following steps: functionalization of the SiO_2 surface with PLL, printing CNT ink in three different patterns (one-pass connected, one-pass separate, and two-pass separate lines), rinsing and annealing of the ink solvent and additives, and printing source and drain electrodes with silver nanoparticle ink. In one-pass connected lines, there is no separation between the lines and no defined coffee ring is formed across the lines, instead a layer with non-uniform thickness forms (Figure 5-2, first row). In the one-pass separate lines pattern, lines are printed with a line spacing between them (Figure 5-2, second row). This spacing was chosen to be the minimum before the lines would merge. The coffee ring effect can be seen in the thickness profiles of printed CNT solution in separate lines (Figure 5-2, second row, inset figure). To achieve two-pass separate lines, after the one-pass separate lines were rinsed and annealed, a second pass of lines was printed with an offset of half the line spacing, followed by rinsing and annealing of the patterns (Figure 5-2, third row). After rinsing and annealing of the ink, the CNTs remain on the surface. The channel length and width of the devices are 80 μm and 1300 μm, respectively.

The CNT concentration for one-pass connected and two-pass separate lines is 4.2×10^{-5} mg/cm^2 after printing before rinsing, while the one-pass separate lines pattern has half the concentration. The following formula was used to calculate CNT concentration per cm^2 printed in the transistor channel:

$$\text{CNT concentration} = \frac{\text{V}_{droplet}\ (\text{mL}) \times \text{CNT concentration} \left(\frac{\text{mg}}{\text{mL}}\right) \times \text{NL}}{\text{DS(cm)} \times \text{LS(cm)}} \qquad 5\text{-}1$$

Where $\text{V}_{droplet}$, NL, DS, and LS are droplet volume, number of layers, drop spacing, and line spacing, respectively. And in the case of two-pass printed lines, $\text{V}_{droplet}$= 1.13×10^{-7}mL, CNT concentration = 0.01 mg/mL, NL = 3, DS = 90 μm, and LS = 180 μm. With the pattern printed twice, CNT concentration becomes 4.2×10^{-5}mg/cm^2. In the case of a one-pass connected line pattern, the line spacing is half (90 μm), therefore resulting in the same value.

5.2.3. Inkjet printing source and drain electrodes

Source and drain electrodes were inkjet-printed on top of the CNT layer on a heated stage (stacked-coin[21]) at 120 ºC using silver nanoparticle ink (ANP DGP 40LT-15C, Advanced Nano Products, Co., Sejong, Korea) with a 60 μm diameter nozzle (Microfab Technologies, Inc. Plano, TX). The silver nanoparticle source and drain electrodes were printed with a length of 2 mm (Figure 5-2, third row, inset figure) while the width of the printed channels is 1300 μm in order to minimize leakage currents.

As was mentioned in the fabrication process, the annealing temperature for the CNT layer is 100 °C. While as is mentioned here, to print the source and drain electrodes, the stage temperature at the time of printing the electrodes is set to120 °C which is not much higher than the CNT annealing temperature. Heating the stage is necessary to stop the silver ink from spreading nonuniformly on the previously deposited CNT network. In fact, it has been shown that CNT exposure to high temperature further removes the solvent and surfactant causing a resistance barrier reduction in the CNT network which leads to higher conductivity and transparency.[150] Not to mention that thermal annealing of CNT layers can also increase their mechanical stability.[151] Therefore, if the heated stage has had an effect on the CNT layer, it would have probably been toward further solvent removal and increasing conductivity.

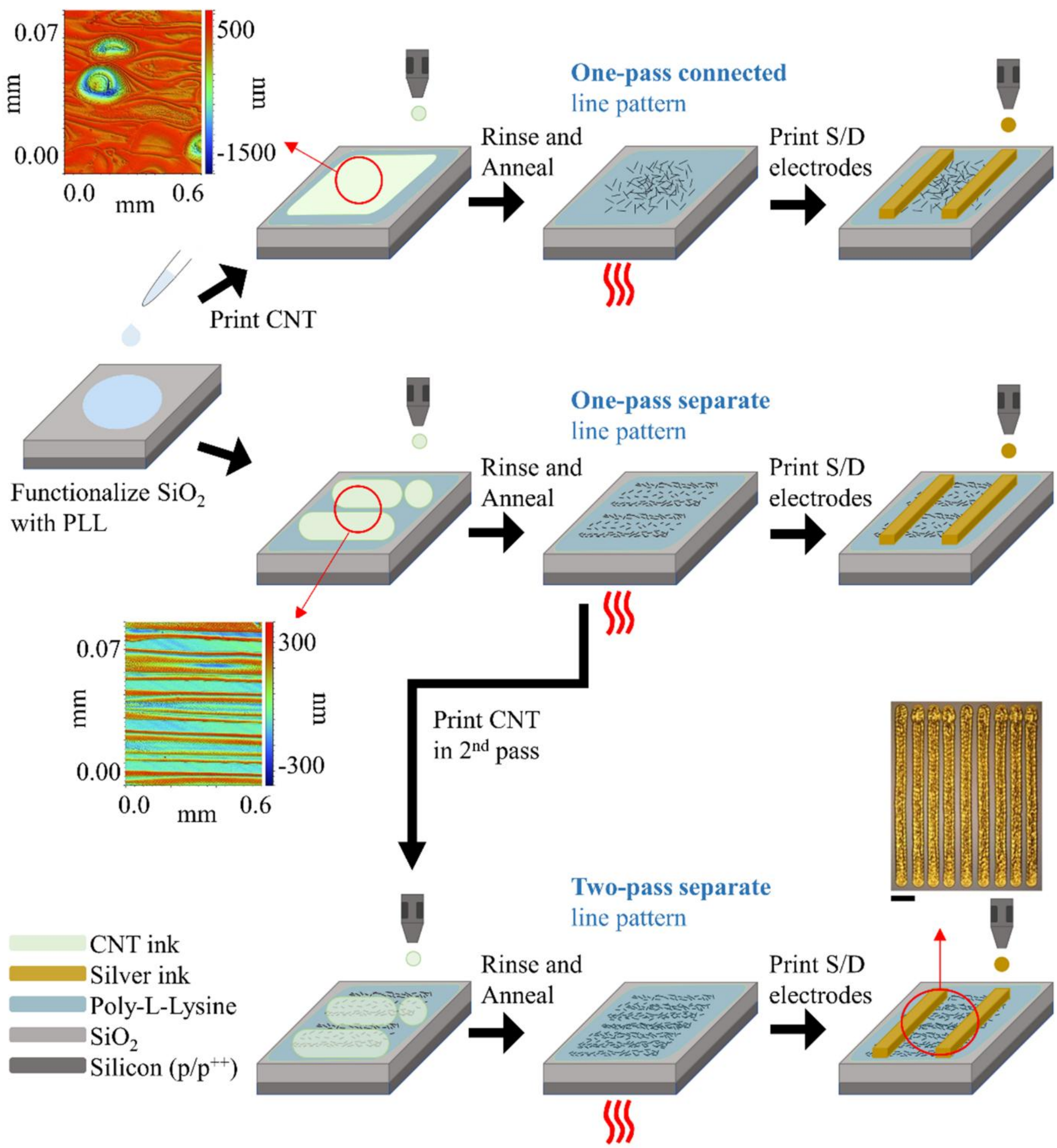

Figure 5-2. The transistor fabrication process in the following steps: functionalization of the SiO2 surface with Poly-L-Lysine, printing CNT ink in three different patterns (one-pass connected, one-pass separate, and two-pass separate lines), rinsing and annealing of the ink solvent and additives, and printing source and drain electrodes with silver nanoparticle ink. In one-pass connected lines,

there is no separation between the lines and no defined coffee ring is formed across the lines. In two-pass separate lines, after the one-pass separate lines are rinsed and annealed, a second pass of lines are printed with an offset of half the line spacing. Inset figures: thickness profiles of printed CNT solution in connected lines (first row) and in separate lines (second row), and optical micrograph of TFTs with channel lengths of 60 and 80 µm (third row) where the scale bar represents 200 µm.

5.2.4. Inkjet printing accuracy

The Microfab inkjet printing nozzle used here has a diameter of 60 µm and the thinnest printed lines (consisting of one layer) have a width of around 100 µm. To print a second layer of a pattern, the printing stage moves back to the origin defined in the printer software. The registration error mainly depends on the accuracy of the motion stages of the printer and the camera system. To experimentally quantify the registration error, top-gate top-contact OTFT electrodes were printed, which are more easily visible than CNTs (Figure 5-3). The average alignment error and standard deviation over seven devices were calculated, while aiming for the gate electrode to lie exactly halfway between the source and drain electrodes. The average error and standard deviation are 1.4 µm and 0.9 µm, respectively. This experiment demonstrates the high accuracy of the printer setup, which allows the precise printing of multi-layer CNT lines.

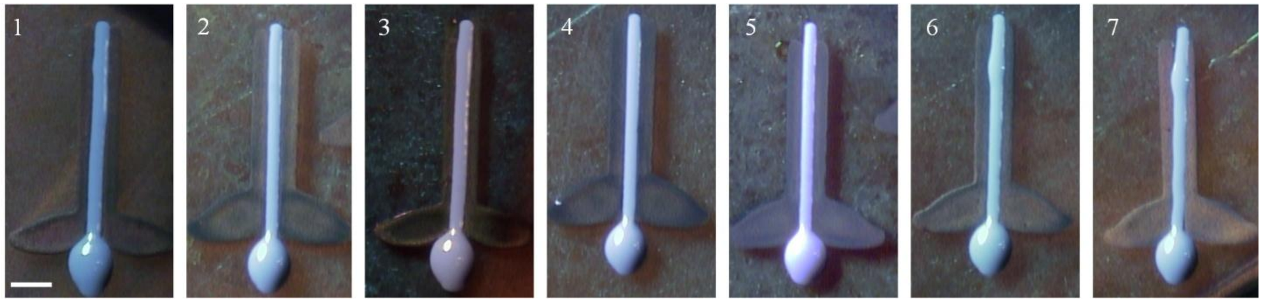

Figure 5-3. Optical micrographs of top-gate bottom-contact transistors presented here for the purpose of calculating printing alignment accuracy. The gate electrode alignment has a 1.4 μm average error with a 0.9 μm standard deviation over seven devices. The scale bar represents 200 μm.

5.3. Coffee ring effect engineering

Two factors, number of layers and printing speed, which controls delay between adjacent droplets, were used to adjust the intensity of the coffee ring effect. Figure 5-4 shows the 3D thickness profiles of lines printed in two different conditions, with two sets of factors. In Figure 5-4a, there is one layer of CNT printed at high speed (1000 μm/s). When the speed is high, the droplet deposition delay is shorter than droplet drying duration. As a result, as was discussed in the introduction chapter, with the right drop spacing, a smooth line morphology can be achieved. Whereas, in Figure 5-4b, the printing speed is lower (400 μm/s), and the droplet deposition delay is longer than the droplet drying duration. In this case, coffee ring effect occurs, and the ink is pushed to the line edges. Finally, in Figure 5-4c, the printing speed is the lowest (200 μm/s), and droplet deposition delay is much longer than droplet drying duration, therefore droplets dry individually, and as a result they form the stacked-coin morphology discussed extensively in chapter 3. At low speed, due to the longer delay in printing between subsequent droplets, the droplets are dried and pinned before the next droplet hits the substrate while the intersection of the two adjacent droplets redissolves as the second drop is printed. In contrast, at higher speed, each incoming droplet promptly merges with its predecessor, resulting in a larger liquid ink amount, an increased capillary flow toward the pattern edges, and a stronger coffee ring effect. Thickness profiles were taken with a Contour CT-K optical profiler (Bruker Nano, Inc., Arizona, USA).

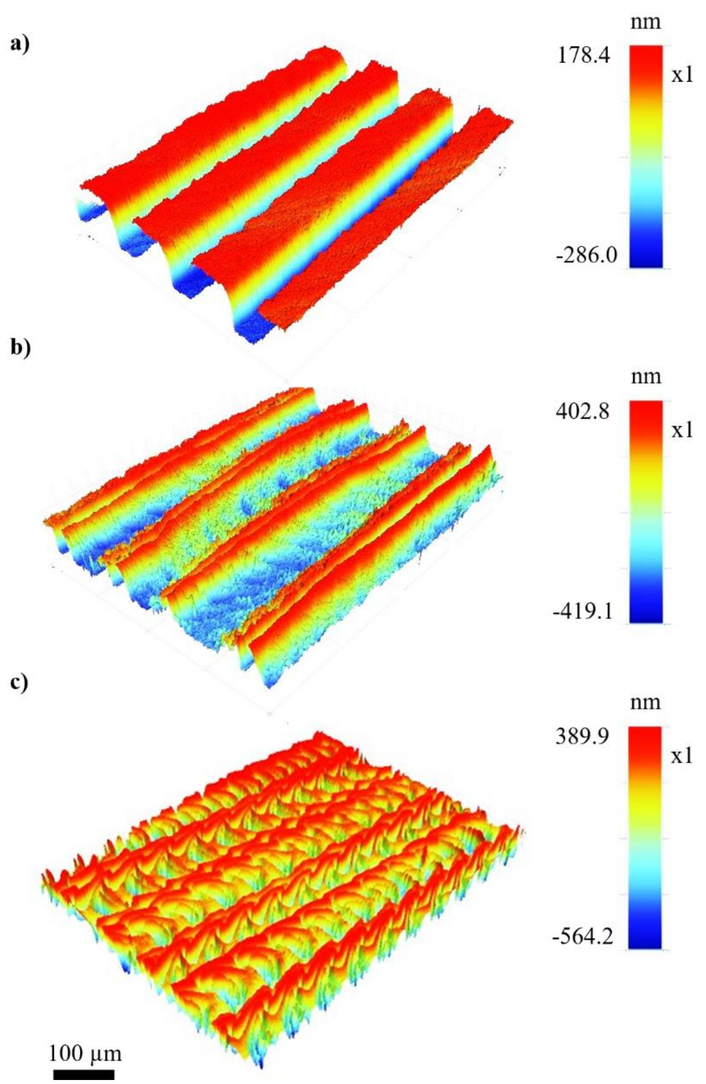

Figure 5-4. The 3D thickness profiles of lines printed with (a) one layer and speed of 1000 μm/s formed as uniform lines, (b) three layers and speed of 400 μm/s formed as lines with coffee ring

effect on the edges, and (c) two layers and speed of 200 µm/s, forming coffee ring effect on droplet edges which results in lines resembling stacked-coin morphology.

Figure 5-5a shows 2D optical thickness profiles of CNT lines printed without separation (connected lines). One-pass connected lines result in a random distribution of the CNT solution on the substrate with the formation of occasional puddles. Figure 5-5b shows separate lines printed with low speed (100 µm/s).

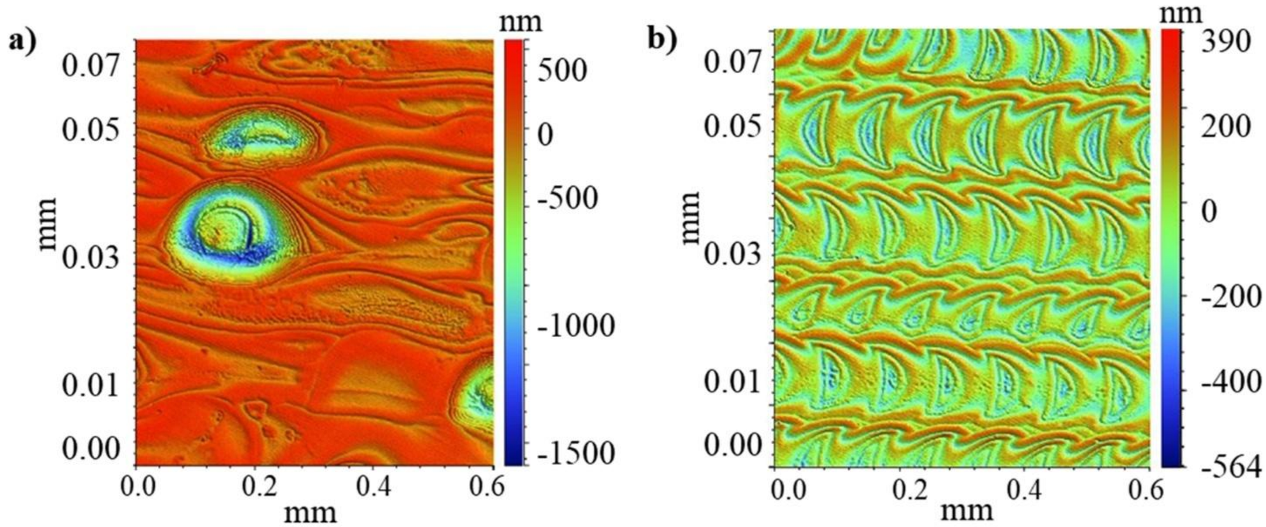

Figure 5-5. 2D optical thickness profiles of (a) lines printed without separation (connected lines), (b) separate lines printed at low speed (100 µm/s)

The addition of more layers to the pattern serves to amplify the coffee ring effect in the same manner. Figure 5-6 shows separate lines printed with one, two, three and four layers of CNT solution, all printed with a speed of 400 µm/s, along with their corresponding 1D thickness profiles across the printed lines in the y-direction for the different number of layers. The thickness variation across each line in Figure 5-6a is negligible for one layer, while for three and four layers, there is larger thickness at the edges compared to the center of the lines, i.e., a coffee ring was formed. In the fabrication process of two-pass separate lines patterns, the acquisition of a thickness profile, which is amplified by the presence of the fillers, binders, and additives of the ink, to demonstrate the two-pass profile is not possible since the first pass of printed CNTs is rinsed before printing the second pass. AFM images of the lines shown in Figure 5-6 are presented in Figure 5-7. The AFM images were obtained from the boundary between the edge and the area right next to it toward the center where the thickness decreases. All the thickness profiles were taken before rinsing and annealing of the patterns, with fillers, binders, and additives of the ink still present, which makes it challenging to observe individual nanotubes in the AFM images but optical profilometry and AFM show the same trends.

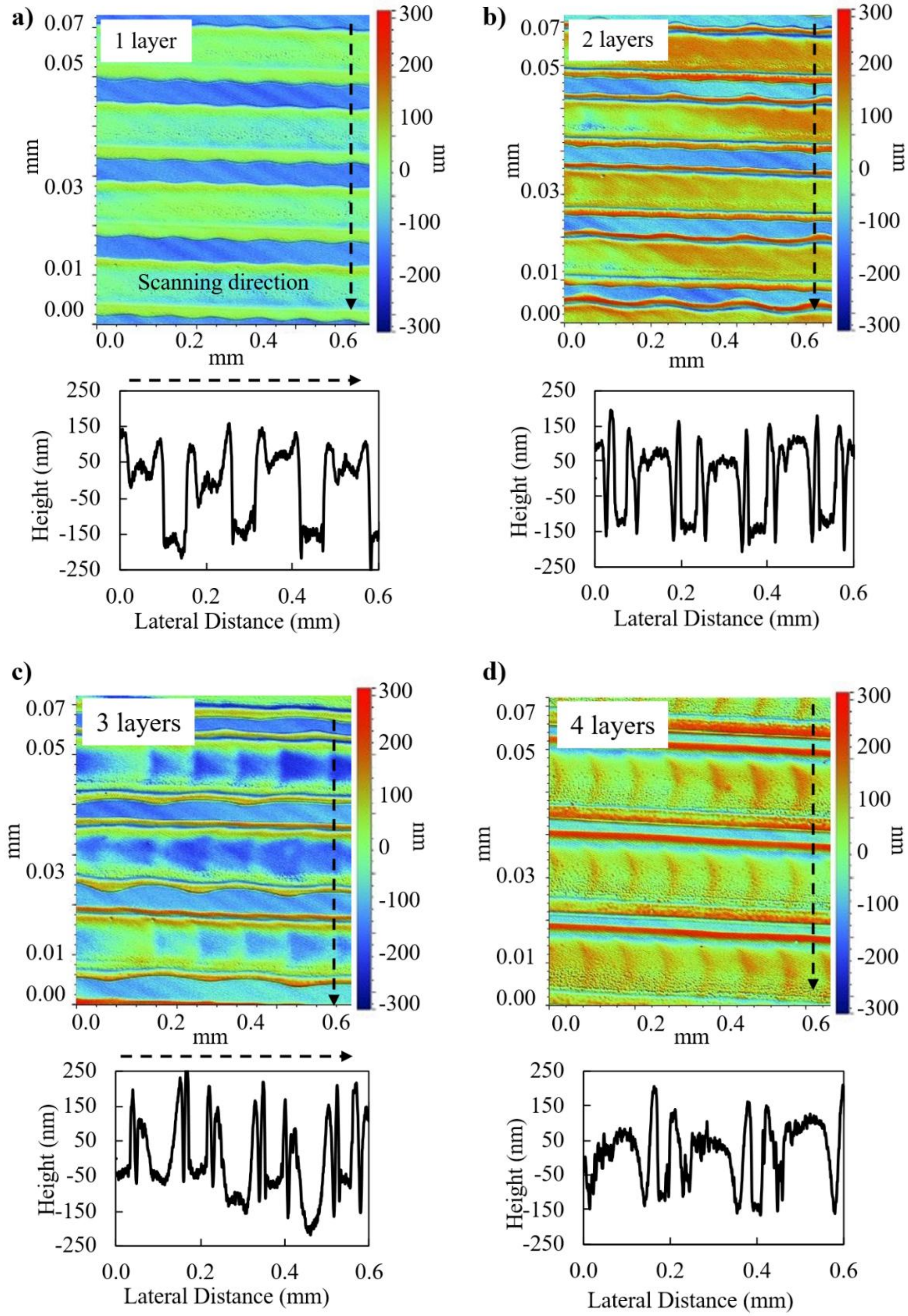

Figure 5-6. (a) Optical thickness profiles of printed separate lines with one, two, three, and four layers from left to right printed with a speed of 400 μm/s. (b) The corresponding 1D thickness

profiles across the lines for lines in (a). Dashed lines in 2D images show the scanning direction where the x-z coordinates were extracted from the 2D optical profile images. The coffee ring effect is most intense in films with three layers.

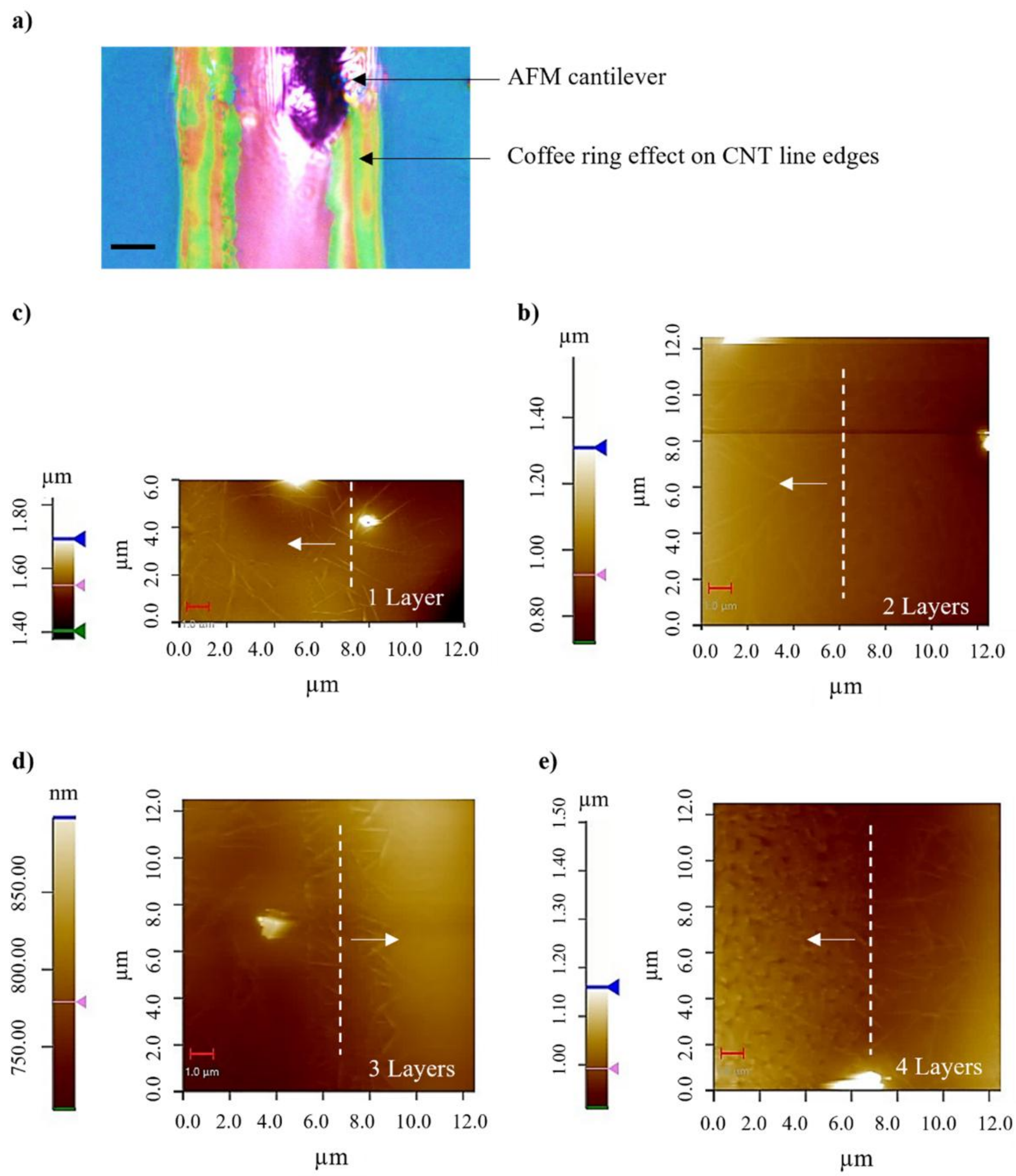

Figure 5-7. AFM images of CNT coffee ring lines after printing and drying before rinsing of excess tubes. (a) A 3-layer CNT line captured by the AFM microscope where the tip of the AFM probe

and the line with coffee ring edges can be seen. Scale bar represents 200 μm. AFM images of (b) one layer, (c) two layers, (d) three layers, and (e) four layers of printed CNT lines. The dashed lines show the boundary between the coffee ring edge (on the arrowhead side) and the area of the line toward the center. For one layer, the coffee ring intensity is low, but it increases for two layers as the color difference between the two sections is more pronounced. The most intense coffee ring effect is observed in lines with three layers. Finally, for four layers, while coffee ring intensity increases, CNT ink covers the center of the line as well.

Figure 5-8a shows plots of two transistor metrics, the on-off current ratio and the field-effect mobility versus the number of layers for transistors printed at 400 μm/s. In all the plots, the metrics were extracted from linear transfer characteristics (I_dV_g) of devices measured at V_d = -5 V. Increasing the number of layers improves the device performance up to a certain point and after that point (from four layers) the performance deteriorates. This can be explained by the optical thickness profile of printed lines with four layers in Figure 5-6. For a larger number of layers, thicker line edges are formed, however the center of the lines are not depleted of material as it is the case in lines with three layers. This means that enhanced performance is due to the coffee ring effect and not simply the overall CNT concentration in the channel. Figure 5-8b shows plots of the same device properties versus printing speed for transistors printed with three layers. Increasing printing speed enhances the coffee ring effect and this improves device properties. However, the direct speed-performance relationship breaks down at high speed. The reason is that at higher printing speed, while material is pushed to the line edges, it is also pushed to the ends of the lines, ultimately reducing the CNT concentration in the channel. Figure 5-9a shows optical thickness profile of CNT lines printed at the speed of 1000 μm/s, with a line spacing of 180 μm. Figure 5-9b shows the micrograph of the ends of those lines. It can be seen from the bulges at the line ends that some of the printed material flows to the ends of the printed lines at larger speeds (>400 µm/s) although the coffee ring effect increases. Figure 5-9c and d show optical thickness profile and micrograph of CNT lines printed at the speed of 1000 µm/s, without spacing between the lines (connected lines).

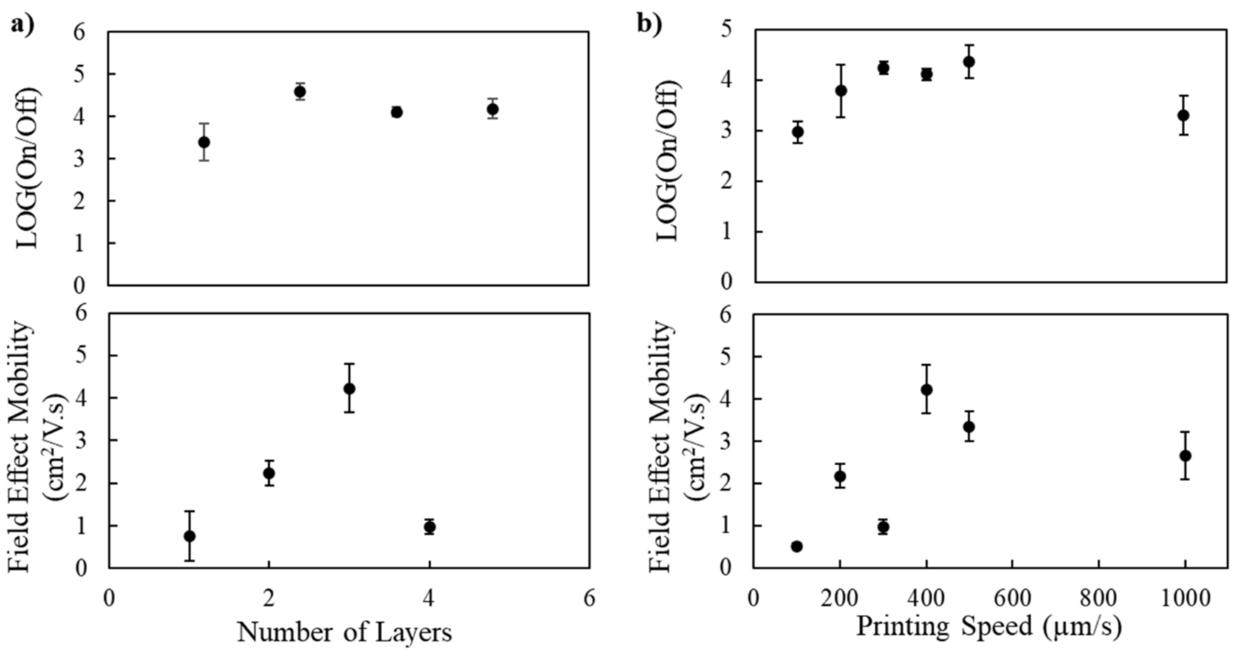

Figure 5-8. Log of on-off current ratio and field-effect mobility measured at V_d = -5 V (a) versus number of printed lines at 400 µm/s, and (b) versus printing speed for printed lines with three layers.

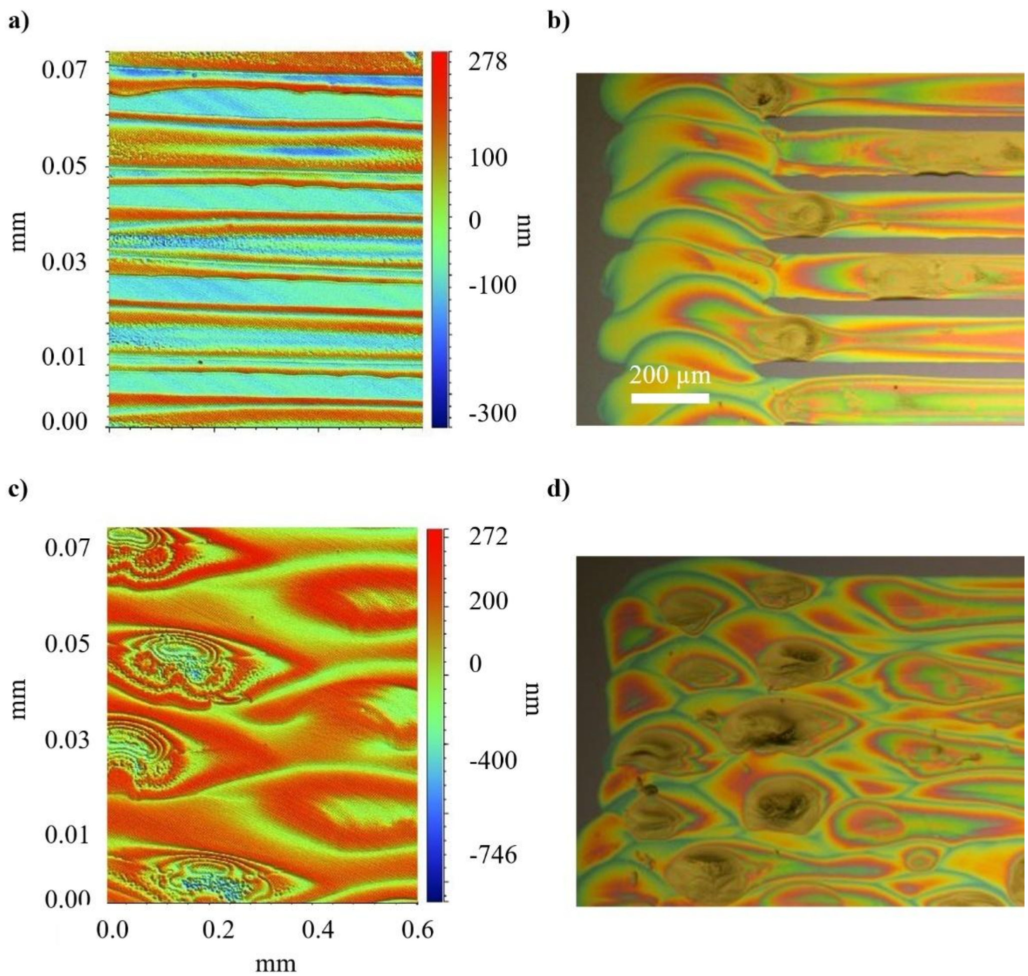

Figure 5-9. (a) Optical thickness profile and (b) micrograph of CNT lines printed at the speed of 1000 µm/s, with a line spacing of 180 µm. (c) Optical thickness profile and (d) micrograph of CNT lines printed at the speed of 1000 µm/s, without spacing between the lines (connected lines). It can be seen from the bulges at the line ends that some of the printed material flows to the ends of the printed lines at larger speeds (>400 µm/s) although the coffee ring effect increases.

5.4. TFT performance based on CNT printing patterns

After exploring the factors affecting the coffee ring effect, transistors with the most pronounced line edges (printed with three layers and at 400 μm/s) were compared with a connected pattern without a gap between the lines. Such a connected pattern is conventionally used in printed CNT TFTs and does not exhibit clearly defined coffee ring lines in the channel.[48,49,145,152]

Figure 5-10a and b show the transfer characteristics (forward sweep) for two-pass separate, one-pass separate, and one-pass connected line patterns measured at V_d = -2 V on logarithmic and linear scales, respectively. The transistor I-V characteristics were obtained using a semiconductor parameter analyzer (Keithley 4200, Tektronix). From one-pass connected and one-pass separate and to two-pass separate line patterns, a shift of threshold voltage (V_t) toward negative gate voltage is observed, and V_t changes from 11.4 V to 12 V to 8.4 V. The separate-line patterns result in devices with better performance. From one-pass connected to one-pass separate to two-pass separate lines, the field-effect mobility increases from 1.1 to 1.5 to 5.7 cm^2/V.s and the on-off current ratio changes from 2.3×10^5 to 8.2×10^5 to 3.6×10^5 at V_d = -2 V. These performance metrics are summarized in Table 5-1. One-pass separate lines have the highest on-off current ratio due to lower concentration of CNTs. With this coffee ring methodology, with equal overall concentrations of CNTs (from one-pass connected to two-pass separate), the device properties improve remarkably. However, the off-current and the gate leakage current increase slightly as well although the CNT concentration remains unchanged from one-pass connected to two-pass separate lines. Figure 5-11 shows the output characteristics (I_dV_d) of one-pass connected, one-pass separate and two-pass separate line patterns from top to bottom, respectively. The curvature in I_dV_d characteristics at low V_d in the one-pass connected line pattern is an indication of a non-ohmic contact,[153] while the drain current does not saturate at high V_d. Conversely, in devices with two-pass separate line patterns, the linear regime has a constant slope, and the drain current almost saturates at high V_d. Devices with one-pass separate line pattern also exhibit improved behavior compared to one-pass connected lines.

Two-pass separate lines pattern has an equal concentration of CNTs compared to one-pass connected pattern. However, it demonstrates higher field-effect mobility and current transporting capacity. To investigate the device behavior further, we studied the channel and the contacts by calculating low-field mobility and contact resistance. Using the Y-function method (YFM), the width normalized contact resistance and the low-field mobility of the three printing patterns (two-pass separate, one-pass separate and one-pass connected) were extracted. Low-field mobility is the intrinsic carrier mobility (μ_0) and field-effect mobility (μ_{fe}) is the carrier mobility in the presence of an electric field which is influenced by contact effects. The Y-function is defined as:

$$Y = \frac{I_d}{\sqrt{g_m}} = \sqrt{\frac{W}{L} C_{ox} \mu_0 V_d} \times \left(V_g - V_t\right) \qquad 5\text{-}2$$

Where g_m, W, L, C_{ox}, and μ_0 are transconductance, transistor width and length, dielectric capacitance per unit area (here SiO_2), and low-field mobility, respectively. Using the transfer characteristics in the linear regime (V_d = -2 V) and from the slope and the y-intercept of Y versus V_g, μ_0 and V_t are extracted. [28,35] Later, using equation (5-3), and by extracting the x-intercept of $\frac{1}{\sqrt{g_m}}$ versus $V_g - V_t$, θ is extracted.

$$\frac{1}{\sqrt{g_m}} = \frac{1 + \theta(V_g - V_t)}{\sqrt{\frac{W}{L} C_{ox} \mu_0 V_D}} \qquad 5\text{-}4$$

and,

$$\theta = \theta_0 + \theta^* = \theta_0 + G_m \times R_{sd} \qquad 5\text{-}5$$

Where $\theta_0(\approx 0)$, G_m and R_{sd} are the mobility reduction coefficient, the transconductance parameter and the total source and drain resistances which in the case of identical electrodes is defined as:

$$R_{sd} = 2 \times R_c \qquad 5\text{-}6$$

Where R_c is the contact resistance associated with one electrode. The Y-function allows the extraction of contact resistance from individual devices. The results in Figure 5-12a and b show a remarkable increase of both field-effect (derived from the transfer characteristics) and low-field mobilities and the decrease of contact resistance in the two-pass separate lines pattern compared to the other patterns. The low-field mobility increases from 1.2 to 1.5 to 7.3 cm^2/V.s, while the width normalized contact resistance changes from 2.6 to 1.9 to 0.3 kΩ.cm for one-pass connected, one-pass separate and two-pass separate lines, respectively.

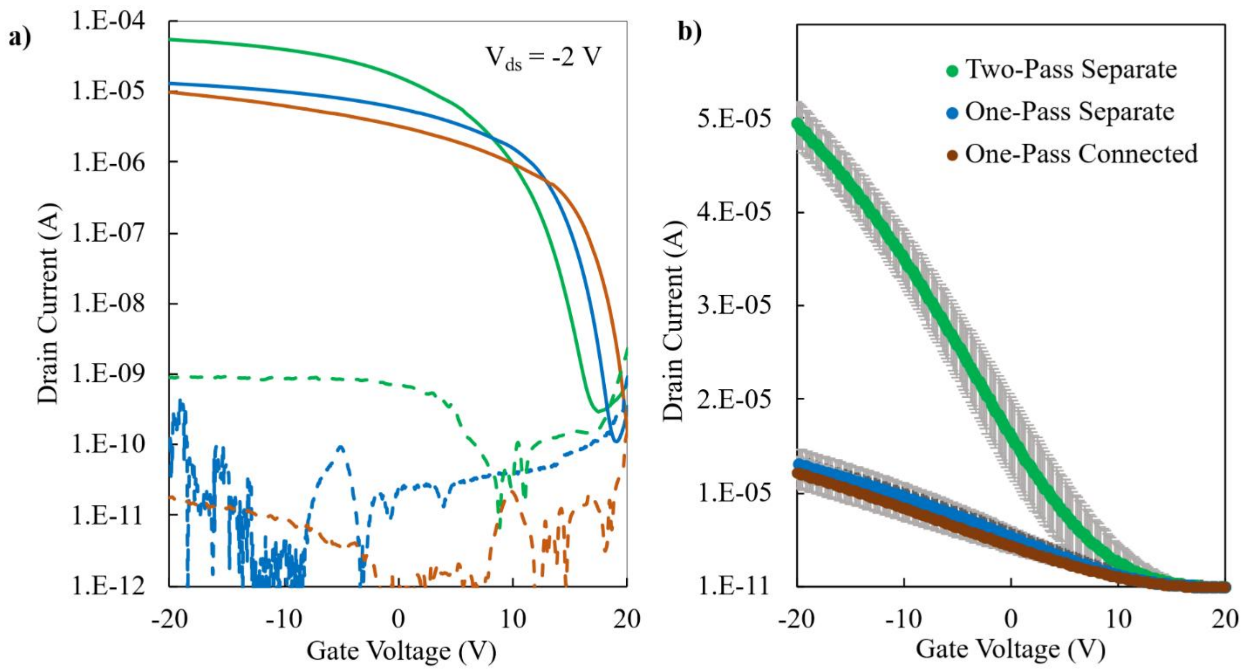

Figure 5-10. (a) Transfer characteristics of the three printing patterns at V_{ds} = -2 V on a log scale. Dashed curves are gate current for each printing pattern and colors are the same as in (b). (b) The same transfer characteristics on a linear scale with error bars representing 8 to 11 devices.

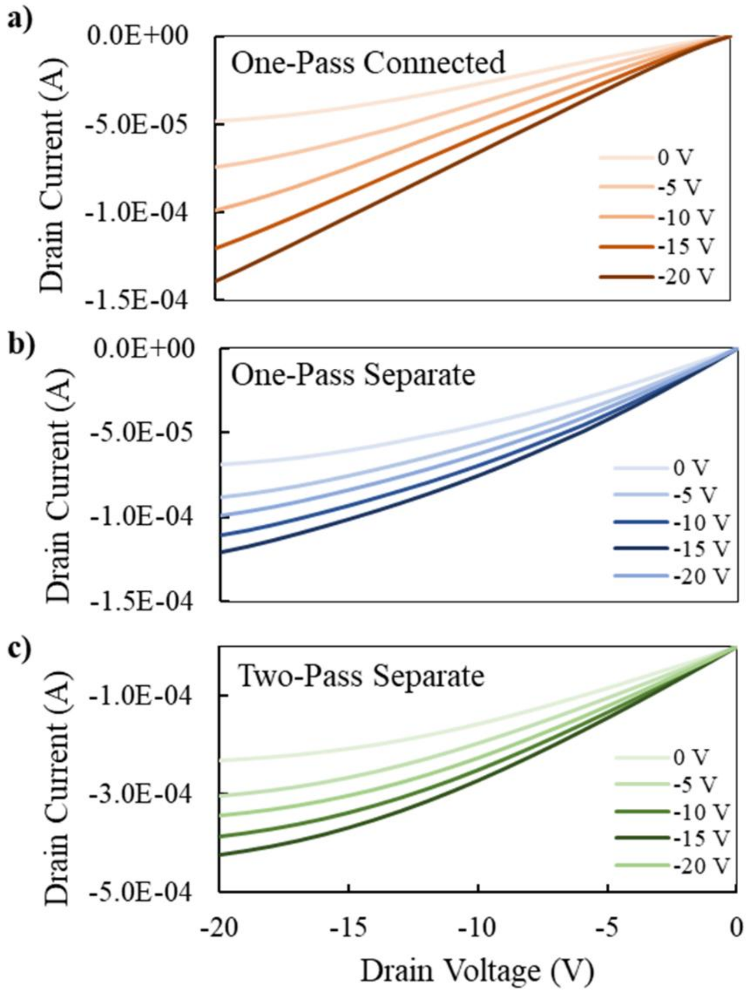

Figure 5-11. Output characteristics of a representative transistor for each pattern: (a) one-pass connected, (b) one-pass separate, and (c) two-pass separate lines.

Table 5-1. Transistor performance metrics for different CNT deposition patterns in the channel.

Pattern	**μ_{fe} (cm^2/V.s)**	**I_{on} (A)**	**V_t (V)**
One-Pass connected	1.1	1.2×10^{-5}	11.4
One-Pass Separate	1.5	1.6×10^{-5}	12
Two-Pass Separate	5.7	4.9×10^{-5}	8.4

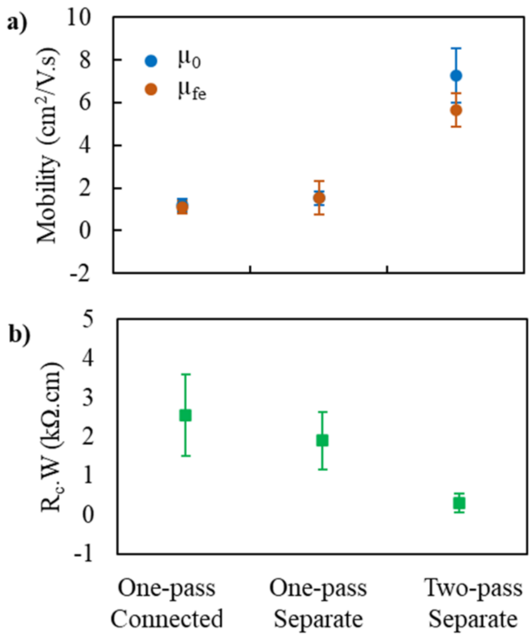

Figure 5-12. (a) Field-effect (μ_{fe}) and low-field (μ_0) mobilities and (b) width normalized contact resistance (R_cW) for the three patterns. The two-pass separate line pattern improves the devices in two ways: increasing the low-field mobility of the carriers in the channel and decreasing the contact resistance.

For the purpose of comparison, devices with drop-cast CNTs were also fabricated and characterized. Figure 5-13 demonstrates drop casting and inkjet printing CNT ink schematically. Inkjet printing is an efficient way of increasing on-off current ratio compared to non-patterned solution deposition techniques such as drop-casting. However, it has been reported that the mobility usually decreases due to the decrease in the CNT concentration. Here, both criteria have been achieved. Non-patterned drop-cast devices exhibit a mobility of 7.5 cm^2/V.s, and an on-off current ratio of 8.2×10^2, at V_d = -5 V, while for two-pass separate line patterns, these figures are 5.7 cm^2/V.s and 3.6×10^5, respectively. Not to mention that for unpatterned drop-cast devices, the maximum gate leakage current is 7.6×10^{-5}A as opposed to the much lower gate leakage current of 2.18×10^{-10}A achieved with printed two-pass separate lines.

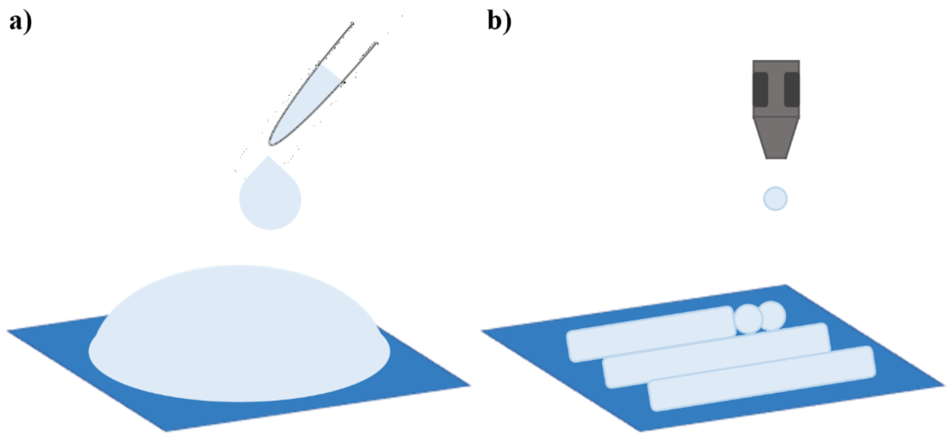

Figure 5-13. Two different solution deposition methods to deposit CNT ink: (a) drop casting, and (b) printing (here, in separate lines)

5.5. CNT bundles

To investigate the device behavior microscopically, AFM images of the channels of four printed patterns were taken with a Multimode 8-HR scanning probe microscope (Bruker, Germany). The imaging mode was ScanAssist-air. The thickness profiles previously shown in Figure 5-6 represent the printed CNT channels before rinsing off the additives in the ink. The un-rinsed profiles show the solute distribution across the printed lines. After rinsing and annealing of the samples, the CNTs remain on the surface as shown in Figure 5-14 with a thickness of a few nanometers as the surface functionalization with Poly-L-Lysine ensures the adhesion of a thin layer of tubes to the surface[154]. Figure 5-14a shows the randomness of the tubes in the channel in a one-pass connected pattern with no coffee ring in the channel. Figure 5-14b shows one-pass separate lines printed at low speed (100 μm/s), which has caused random high and low concentrations of CNTs, while CNTs are not drawn to line borders at the edges, as there is no well-defined coffee ring. Blue arrows point to the line edges in each image. The improved performance of one-pass separate lines printed at higher speed (400 μm/s) can be explained by the formation of distinguished lines of interwoven CNTs in Figure 5-14c where the tubes are connected. Figure 5-14d shows AFM images of two-pass separate lines, which doubles the overall concentration of CNTs compared with one-pass separate line patterns (Figure 5-14c) and exhibits wider paths of interwoven CNTs. These images along with results in Figure 5-10, Figure 5-11, and Table 5-1, demonstrate a direct relationship between the intensity of the coffee ring effect and transistor performance.

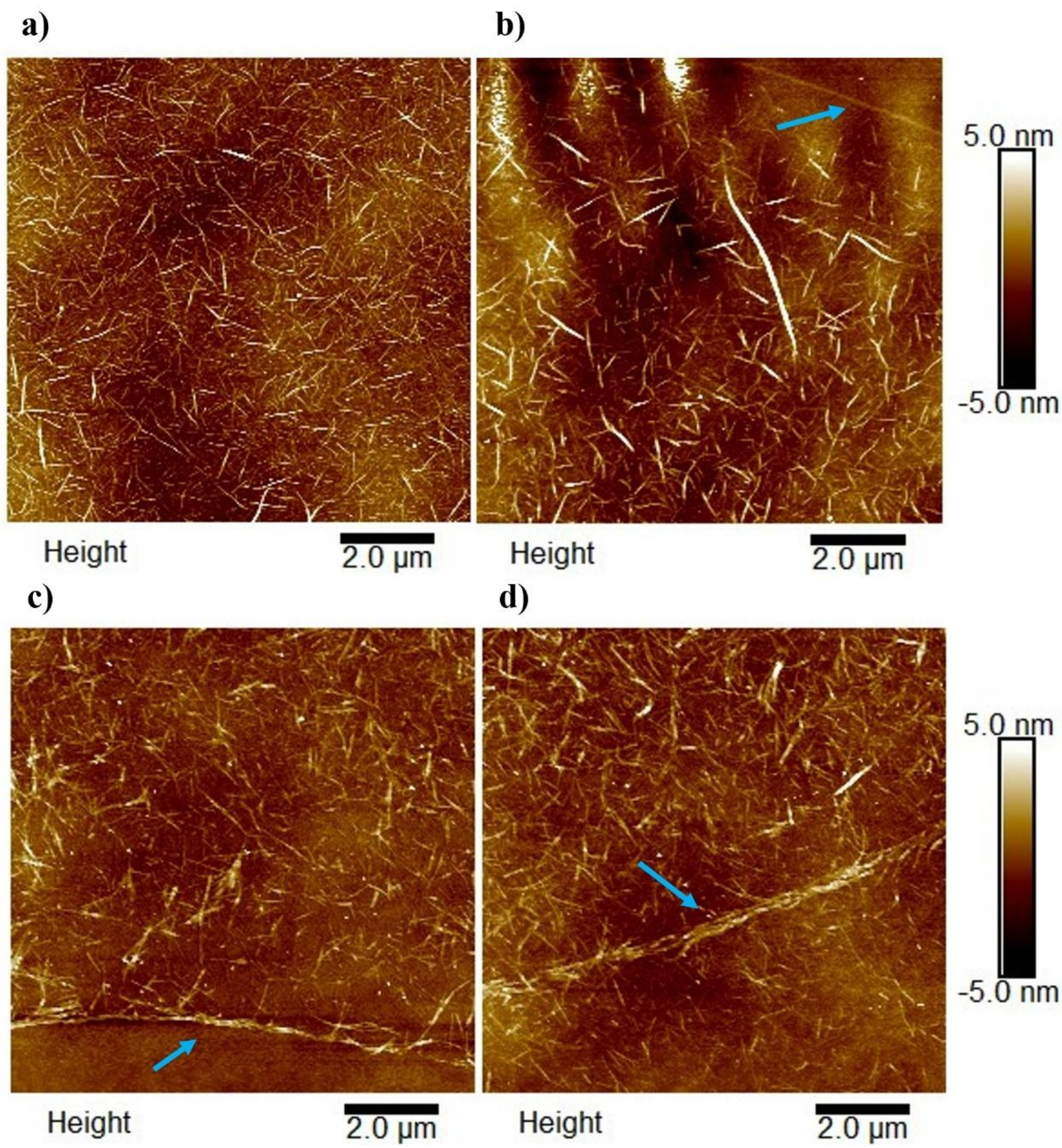

Figure 5-14. AFM images of printed patterns of (a) one-pass connected lines, (b) one-pass separate lines printed at 100 μm/s, c) one-pass separate lines printed at 400 μm/s, and (d) two-pass separate lines printed at 400 μm/s. A blue arrow shows the printed line edges in (b), (c) and (d). In (c) and (d), interwoven tubes can be observed on the line edges.

Having nanotubes with different diameters means having different regions with different intrinsic mobility. In a nanotube network, different lengths, diameters and chiralities determine the intratube transport and they all contribute to the average electronic properties. Moreover, the junctions have a tremendous effect on the carrier transport between the tubes, which manifests itself as tube-to-tube resistance.[155] Tunneling between two tubes apart from their energy band gaps also depends on the angle of the junction.[156] The angle determines the atomic structure at the junction, and when the tubes are in-registry, the junction resistance is low. Certain junction angles cause the tubes to be in-registry.[157] When coffee ring effect happens, as AFM images demonstrate, the tubes form paths by getting entangled on the edge, in other words, they get knit together forming paths with lower resistance. This can increase the probability of tubes having an in-registry configuration, therefore leading to a decrease in tube-to-rube resistance and eventually the channel resistance. The macroscopic manifestation of this effect is the increase of mobility and decrease of contact resistance measured through IV characteristics of the device.

It is noteworthy that in the one-pass connected line pattern (random network) the drain current does not saturate at high drain voltages. This behavior is characteristic of random network CNT transistors, mainly due to the presence of metallic tubes.[145,158] However, the devices with coffee ring induced alignment show an improved level of drain current saturation. In fact, linear output curves at low V_d and drain current saturation at high V_d have been previously reported with spin-aligned CNTs in solution-processed CNT transistors.[147] Here, CNT alignment is achieved in bundles by printing the CNT ink in separate lines with coffee ring. The alignment of tubes along the channel length leads to an effective shortening of the channel as each tube crosses a larger portion of the channel. Furthermore, the formation of CNT bundles decreases the tube-to-tube resistance since there will be a higher probability of tubes having an in-registry configuration where the tube-tube junction angle is low[157]. Therefore, both on-current and off-current increase in the two-pass separate line patterns (Figure 5-10). However, this does not deteriorate drain current saturation (Figure 5-10c bottom). The reason is that the alignment of CNTs along the channel increases the percolation threshold[159–162] because it reduces the probability of the tubes, both semiconducting and metallic, connecting with each other (see schematics Figure 5-2, line patterns in second and third rows). Since the concentration of metallic tubes is significantly lower than the concentration of semiconducting tubes (99.9% semiconducting tubes in the ink), this increase in percolation threshold affects metallic tubes more strongly than semiconducting tubes, which leads to an improvement in current saturation, which is deteriorated by metallic tubes in the random network. Therefore, the simultaneous effects of alignment and bundling of the CNTs along the channel lead to a decrease in the resistance whilst improving drain current saturation in the devices.

The inkjet printing with controlled speed that induces the coffee ring effect not only changes the low-field mobility in the channel, which is independent of contact effects, it also improves the contact resistance. Devices with connected line patterns exhibit a Schottky barrier at the contacts, which is evident from the non-linear output characteristics at low drain current (Figure 5-10), while the aligned patterns are more linear. As was discussed previously to explain the high field effect mobility, the interwoven CNTs have a more in-registry configuration compared to random networks allowing better contact between metal coated CNTs and the channel. Better alignment with the channel also means that more CNTs are in contact with the source and drain electrodes lowering contact resistance. Therefore, their contact with the electrodes becomes more ohmic[147]. This leads to better current injection from the electrodes to the aligned CNTs which is observed as a decrease in contact resistance.

5.6. Conclusions

In this chapter, it was shown that with inkjet printing of the CNT transistor channel, the CNT concentration is reduced, but the randomness of their distribution can be manipulated. While ensuring both high mobility and high on-off current ratio with inkjet printing is difficult, separating the printed lines in the pattern and forming a coffee ring results in considerable improvement in all transistor properties. The coffee ring effect, which can be controlled by printing speed and number of layers, regulates the CNT network in the channel. By changing one-pass connected lines to one-pass separate lines and to two-pass separate lines, the field-effect mobility extracted at the drain voltage of -2 V increases from 1.1 to 1.5 to 5.7 $cm^2/V.s$, and the on-off current ratio changes from 2.3×10^5 to 8.2×10^5 to 3.6×10^5. The YFM shows a higher low-field channel mobility and lower contact resistance caused by the coffee ring induced regulated tubes compared with a random CNT network. These results can be explained by the lower tube-to-tube resistance of CNTs in the thicker line edge regions with interwoven CNTs for separate line patterns compared to connected lines. With these capabilities, inkjet printing is a promising technique to form CNT channels in TFTs.

Chapter 6: Conclusions and future work

In this thesis, inkjet printing was used as a fundamental tool to produce thin films of material. Parameters and conditions for engineering patterns in general and on challenging surfaces were investigated. Inkjet-printed lines of functional inks were utilized as channel material and electrodes in thin-film transistors.

6.1. Conclusions

Two approaches were demonstrated that have the ability to form micro-patterns on hydrophobic surfaces. Chapter 2 introduces a novel printing method capable of forming micro-patterns on surfaces with low wettability without necessitating surface modification: a sequential printing and drying method. Utilizing an energy minimization model, this method accurately predicts the shape of inkjet-printed micro-patterns based solely on the ink's contact angle, confirming the dominant role of surface tension forces in pattern formation. The varying ink volume between anchors influences the width of line segments, where an optimal volume yields a smooth, consistent line. This strategy demonstrates its potential applicability for creating longer lines and even corners, showcasing a successful approach to overcome the challenge of printing on surfaces with low wettability. The impact of varying ink volumes on line segment formation and the power of the simulations to predict the volume and shape of the printed patterns, offer a promising strategy for inkjet printing on hydrophobic surfaces. Finally, the energy minimization-based simulations were used to predict the required ink to produce dry lines and triangles with smooth edges. Both experimental and computational simulations successfully extend to more complex shapes, such as triangles, demonstrating the utility of the Printability Factor (PF) in forecasting the final printed features and reducing material waste.

Chapter 3 further delineates the stacked-coin approach as a robust method for inkjet printing on hydrophobic surfaces. It identifies the interplay between stage speed, droplet spacing, and stage temperature as critical parameters dictating the printability of stacked-coin lines. Through precise mapping of these parameters, the method facilitates the prediction and realization of the true stacked-coin morphology, with a significant temperature threshold of 180 ºC for instantaneous drying, contributing to an enhanced throughput of printed lines. The following regimes were identified: isolated droplets, isolated groupings, broken line, true stacked-coin, and delamination. The relationship between substrate temperature, drop spacing and droplet deposition delay controls the printability window of true stacked-coin morphology and its surrounding regimes. These strategies showcased the potential to create precise micro-patterns on challenging hydrophobic surfaces.

In chapter 4, the focus shifts to the fabrication of OTFTs with inkjet-printed electrodes on a hydrophobic fluoropolymer gate dielectric. Source and drain electrodes were inkjet-printed on Teflon-AF with a minimum channel length of 20 μm. The annealing of the inkjet-printed electrodes changes the morphology and the surface chemistry of the Teflon-AF gate dielectric underneath, thus reversing the effect of the plasma treatment on Teflon-AF. The work meticulously explores the effects of plasma treatment and post-annealing on the Teflon-AF surface, revealing how these processes modulate wettability, surface roughness, and chemical composition. The findings elucidate a temperature-dependent optimization of the OSC/dielectric interface, leading to improved transistor performance, as evidenced by the maximized field-effect mobility and on-off current ratio at an optimal post-annealing temperature of 160 ºC. The transistor parameters such as mobility, on/off current ratio, and threshold voltage all follow a trend explained in this thesis by the properties of the Teflon-AF surface. Increasing the post-annealing temperature to just below complete surface reversibility decreases surface roughness and trap-sites created after plasma treatment leading to optimized device performance. The Teflon-AF surface was characterized with contact angle measurement, roughness measurement, Fourier transform infrared spectroscopy (FTIR), and x-ray photoelectron spectroscopy (XPS). This understanding of the reversibility of the Teflon-AF surface helps achieve optimal performance of devices and systems incorporating fluoropolymers. This thorough investigation shows the importance of interface engineering and layer deposition order in solution-processed OFETs. The findings underscore the critical role of surface treatment in defining the performance of OTFTs. By manipulating the Teflon-AF surface properties through plasma treatment and controlled post-annealing, one can engineer the OSC/dielectric interface to enhance device performance. This study highlights the potential of reversible surface treatments as a powerful tool for optimizing printed electronics, particularly in applications where the interface between different materials is pivotal to device operation.

Finally, chapter 5 presents a method for inkjet printing of carbon nanotube (CNT) transistor channels. By harnessing the coffee ring effect through control over printing speed and the number of layers, a significant enhancement in transistor properties is achieved. Printing properties were studied to manipulate capillary flow and form thicker line edges, which ultimately enhance current transport in the CNT network. It was shown that inkjet-printed devices can have both high field-effect mobility and on-off current ratio by utilizing coffee ring in the channel. A two-pass printing pattern with separate lines improves the field-effect mobility five times compared to a pattern with connected lines that has no defined edges. The field-effect mobility increases from 1.1 to 5.7 $cm^2/V.s$ at a drain voltage of -2 V. These findings underscore the potential for controlled inkjet printing methods to significantly enhance transistor properties and performance. This technique allows for the precise manipulation of CNT distribution, achieving high mobility and on-off current ratios. The study demonstrates the potential of inkjet printing in forming CNT channels for TFTs, paving the way for advanced electronic device fabrication.

6.2. Future work

A range of inks and substrates are suggested to be tested with the sequential printing and energy minimization technique to verify the universality of the method introduced in chapter 2. Moreover, the method has been shown to apply to two patterns, lines and triangles. For future research, more complicated patterns can be printed and simulated. The error between simulation and experimental work for triangles was higher compared to lines. This implies that the simulation model can be further refined in applying the method to more intricate and diverse patterns.

The stacked-coin approach described in chapter 3 invites the examination of other hydrophobic materials and varying environmental conditions to expand its applicability. In producing stacked-coin lines, one limitation was the movement of the printing stage. The printing stage stops during the ejection of a droplet and moves between the two consecutive ejections. This limits the speed and acceleration of the printing and affects the merging of droplets on the surface. Thus, investigating the continuous movement of printing stages could yield improvements in line quality and printing speed. For instance, using an inkjet printer such as Dimatix or Pixdro in which droplet ejection is set with a certain frequency and the stage moves without stopping during the printing process, can be very effective in producing smooth features.

Subsequent research stemming from chapter 4 should delve into the long-term stability of the modified Teflon-AF surfaces and their interaction with different OSC materials. Exploring alternative dielectric materials and post-treatment conditions may offer insights into the broader implications of surface treatment on device performance. As post annealing of the Teflon-AF layer in OTFTs significantly affects its interface with the organic semiconductor, one can change the order of layers for possible improvement of device performance. If the devices are built in a top-gate configuration, the dielectric layer will not be subjected to a second annealing step. In this case, the semiconductor instead will go through a second annealing step and moreover it will share an interface with the substrate causing a different set of challenges. Continuing this research can add more insight into optimizing interfaces in OTFTs that incorporate hydrophobic gate dielectrics.

The promising results of chapter 5 encourage further optimization of the inkjet printing parameters for CNT channels. Inkjet printing and patterning of CNT ink in a FET channel required careful engineering of the coffee ring effect. Future work can be done on reducing the droplet volume by using other printing equipment and varying environmental conditions such as temperature and substrate surface roughness to further control the inkjet-printed patterns. Further optimization of the printing parameters and surface functionalization can be very interesting. Lastly, future studies should focus on the scalability of the process, the integration of printed CNT channels into complex circuits, and the exploration of other semiconducting materials that could benefit from controlled patterning techniques like the coffee ring effect.

In conclusion, this thesis contributes valuable methodologies and insights to the field of printed electronics, with each chapter building upon the understanding of material properties, process control, and the critical factors influencing device performance. The work lays a foundation for future innovations in printed electronic devices, with potential applications spanning from flexible electronics to advanced sensors and beyond.

Chapter 7: References

(1) Bonnassieux, Y.; Brabec, C. J.; Cao, Y.; Carmichael, T. B.; Chabinyc, M. L.; Cheng, K. T.; Cho, G.; Chung, A.; Cobb, C. L.; Distler, A.; Egelhaaf, H. J.; Grau, G.; Guo, X.; Haghiashtiani, G.; Huang, T. C.; Hussain, M. M.; Iniguez, B.; Lee, T. M.; Li, L.; Ma, Y.; Ma, D.; McAlpine, M. C.; Ng, T. N.; Österbacka, R.; Patel, S. N.; Peng, J.; Peng, H.; Rivnay, J.; Shao, L.; Steingart, D.; Street, R. A.; Subramanian, V.; Torsi, L.; Wu, Y. The 2021 Flexible and Printed Electronics Roadmap. *Flex. Print. Electron.* **2021**, *6* (2), 023001. https://doi.org/10.1088/2058-8585/ABF986.

(2) Grau, G.; Kitsomboonloha, R.; Swisher, S. L.; Kang, H.; Subramanian, V. Printed Transistors on Paper: Towards Smart Consumer Product Packaging. *Adv. Funct. Mater.* **2014**, *24* (32), 5067–5074. https://doi.org/10.1002/adfm.201400129.

(3) Borchert, J. W.; Borchert, J. W.; Zschieschang, U.; Letzkus, F.; Giorgio, M.; Giorgio, M.; Weitz, R. T.; Weitz, R. T.; Weitz, R. T.; Caironi, M.; Burghartz, J. N.; Ludwigs, S.; Klauk, H. Flexible Low-Voltage High-Frequency Organic Thin-Film Transistors. *Sci. Adv.* **2020**, *6* (21). https://doi.org/10.1126/SCIADV.AAZ5156/SUPPL_FILE/AAZ5156_SM.PDF.

(4) Grau, G.; Kitsomboonloha, R.; Swisher, S. L.; Kang, H.; Subramanian, V. Printed Transistors on Paper: Towards Smart Consumer Product Packaging. *Adv. Funct. Mater.* **2014**, *24* (32), 5067–5074. https://doi.org/10.1002/adfm.201400129.

(5) Grau, G.; Subramanian, V. Dimensional Scaling of High-Speed Printed Organic Transistors Enabling High-Frequency Operation. *Flex. Print. Electron.* **2020**, *5* (1), 014013. https://doi.org/10.1088/2058-8585/AB739A.

(6) Giri, G.; Verploegen, E.; Mannsfeld, S. C. B.; Atahan-Evrenk, S.; Kim, D. H.; Lee, S. Y.; Becerril, H. A.; Aspuru-Guzik, A.; Toney, M. F.; Bao, Z. Tuning Charge Transport in Solution-Sheared Organic Semiconductors Using Lattice Strain. *Nat. 2011 4807378* **2011**, *480* (7378), 504–508. https://doi.org/10.1038/nature10683.

(7) Mitzi, D. B. Solution-Processed Inorganic Semiconductors. *J. Mater. Chem.* **2004**, *14* (15), 2355–2365. https://doi.org/10.1039/B403482A.

(8) Schindler, A.; Brill, J.; Fruehauf, N.; Novak, J. P.; Yaniv, Z. Solution-Deposited Carbon Nanotube Layers for Flexible Display Applications. *Phys. E Low-dimensional Syst. Nanostructures* **2007**, *37* (1–2), 119–123. https://doi.org/10.1016/J.PHYSE.2006.07.016.

(9) Cai, L.; Zhang, S.; Miao, J.; Yu, Z.; Wang, C. Fully Printed Stretchable Thin-Film Transistors and Integrated Logic Circuits. *ACS Nano* **2016**, *10* (12), 11459–11468. https://doi.org/10.1021/ACSNANO.6B07190/SUPPL_FILE/NN6B07190_SI_001.PDF.

(10) Yu, M.; Wan, H.; Cai, L.; Miao, J.; Zhang, S.; Wang, C. Fully Printed Flexible Dual-Gate Carbon Nanotube Thin-Film Transistors with Tunable Ambipolar Characteristics for

Complementary Logic Circuits. *ACS Nano* **2018**, *12* (11), 11572–11578. https://doi.org/10.1021/acsnano.8b06748.

(11) Camus, A.; Reali, M.; Santato, C. Advances in High-Resolution Printed Transistors: The Case of Bio-Sourced Organic Materials. *Curr. Opin. Green Sustain. Chem.* **2022**, *34*, 100594. https://doi.org/10.1016/J.COGSC.2022.100594.

(12) Cardenas, J. A.; Catenacci, M. J.; Andrews, J. B.; Williams, N. X.; Wiley, B. J.; Franklin, A. D. In-Place Printing of Carbon Nanotube Transistors at Low Temperature. *ACS Appl. Nano Mater.* **2018**, *1* (4), 1863–1869. https://doi.org/https://doi.org/10.1021/acsanm.8b00269.

(13) Seifert, T.; Sowade, E.; Roscher, F.; Wiemer, M.; Gessner, T.; Baumann, R. R. Additive Manufacturing Technologies Compared: Morphology of Deposits of Silver Ink Using Inkjet and Aerosol Jet Printing. *Ind. Eng. Chem. Res.* **2015**, *54* (2), 769–779. https://doi.org/https://doi.org/10.1021/ie503636c.

(14) Liu, Y. F.; Tsai, M. H.; Pai, Y. F.; Hwang, W. S. Control of Droplet Formation by Operating Waveform for Inks with Various Viscosities in Piezoelectric Inkjet Printing. *Appl. Phys. A Mater. Sci. Process.* **2013**, *111* (2), 509–516. https://doi.org/10.1007/S00339-013-7569-7/FIGURES/8.

(15) Nayak, L.; Mohanty, S.; Nayak, S. K.; Ramadoss, A. A Review on Inkjet Printing of Nanoparticle Inks for Flexible Electronics. *J. Mater. Chem. C* **2019**, *7* (29), 8771–8795. https://doi.org/10.1039/C9TC01630A.

(16) Grau, G.; Cen, J.; Kang, H.; Kitsomboonloha, R.; Scheideler, W. J.; Subramanian, V. Gravure-Printed Electronics: Recent Progress in Tooling Development, Understanding of Printing Physics, and Realization of Printed Devices. *Flexible and Printed Electronics*. Institute of Physics Publishing June 1, 2016, p 023002. https://doi.org/10.1088/2058-8585/1/2/023002.

(17) Abunahla, R.; Rahman, M. S.; Naderi, P.; Grau, G. Improved Inkjet-Printed Pattern Fidelity: Suppressing Bulges by Segmented and Symmetric Drop Placement. *J. Micro Nano-Manufacturing* **2020**, *8* (3), 031001. https://doi.org/10.1115/1.4046482/1074938.

(18) Stringer, J.; Derby, B. Formation and Stability of Lines Produced by Inkjet Printing. *Langmuir* **2010**, *26* (12), 10365–10372. https://doi.org/10.1021/la101296e.

(19) Antonini, C.; Amirfazli, A.; Marengo, M. Drop Impact and Wettability: From Hydrophilic to Superhydrophobic Surfaces. *Phys. Fluids* **2012**, *24* (10), 102104. https://doi.org/10.1063/1.4757122/257852.

(20) Duineveld, P. C. The Stability of Ink-Jet Printed Lines of Liquid with Zero Receding Contact Angle on a Homogeneous Substrate. *J. Fluid Mech.* **2003**. https://doi.org/10.1017/S0022112002003117.

(21) Soltman, D.; Subramanian, V. Inkjet-Printed Line Morphologies and Temperature Control of the Coffee Ring Effect. *Langmuir* **2008**, *24* (5), 2224–2231. https://doi.org/10.1021/LA7026847/SUPPL_FILE/LA7026847-FILE006.AVI.

(22) Deegan, R. D.; Bakajin, O.; Dupont, T. F.; Huber, G.; Nagel, S. R.; Witten, T. A. Capillary Flow as the Cause of Ring Stains from Dried Liquid Drops. *Nat. 1997 3896653* **1997**, *389* (6653), 827–829. https://doi.org/10.1038/39827.

(23) Numata, H.; Ihara, K.; Saito, T.; Endoh, H.; Nihey, F. Highly Uniform Thin-Film Transistors Printed on Flexible Plastic Films with Morphology-Controlled Carbon Nanotube Network Channels. *Appl. Phys. Express* **2012**, *5* (5), 055102. https://doi.org/10.1143/APEX.5.055102/XML.

(24) Liu, R.; Ding, H.; Lin, J.; Shen, F.; Cui, Z.; Zhang, T. Fabrication of Platinum-Decorated Single-Walled Carbon Nanotube Based Hydrogen Sensors by Aerosol Jet Printing. *Nanotechnology* **2012**, *23* (50), 505301. https://doi.org/10.1088/0957-4484/23/50/505301.

(25) Fukuda, K.; Someya, T. Recent Progress in the Development of Printed Thin-Film Transistors and Circuits with High-Resolution Printing Technology. *Adv. Mater.* **2017**, *29* (25), 1602736. https://doi.org/10.1002/ADMA.201602736.

(26) Kumar Singh, V.; Mazhari, B. Measurement of Threshold Voltage in Organic Thin Film Transistors. *Appl. Phys. Lett.* **2013**, *102* (25), 253304. https://doi.org/10.1063/1.4812191.

(27) Waldrip, M.; Jurchescu, O. D.; Gundlach, D. J.; Bittle, E. G. Contact Resistance in Organic Field-Effect Transistors: Conquering the Barrier. *Adv. Funct. Mater.* **2020**, *30* (20), 1904576. https://doi.org/10.1002/adfm.201904576.

(28) Xu, Y.; Minari, T.; Tsukagoshi, K.; Chroboczek, J. A.; Ghibaudo, G. Direct Evaluation of Low-Field Mobility and Access Resistance in Pentacene Field-Effect Transistors. *J. Appl. Phys.* **2010**, *107* (11), 114507. https://doi.org/10.1063/1.3432716.

(29) Pacheco-Sanchez, A.; Claus, M.; Mothes, S.; Schröter, M. Contact Resistance Extraction Methods for Short- and Long-Channel Carbon Nanotube Field-Effect Transistors. *Solid. State. Electron.* **2016**, *125*, 161–166. https://doi.org/10.1016/J.SSE.2016.07.011.

(30) Shin, K. H.; Nguyen, H. A. D.; Park, J.; Shin, D.; Lee, D. Roll-to-Roll Gravure Printing of Thick-Film Silver Electrode Micropatterns for Flexible Printed Circuit Board. *J. Coatings Technol. Res.* **2017**, *14* (1), 95–106. https://doi.org/10.1007/S11998-016-9844-Y/TABLES/3.

(31) Falconnet, D.; Csucs, G.; Michelle Grandin, H.; Textor, M. Surface Engineering Approaches to Micropattern Surfaces for Cell-Based Assays. *Biomaterials* **2006**, *27* (16), 3044–3063. https://doi.org/10.1016/J.BIOMATERIALS.2005.12.024.

(32) Shin, W. C.; Seo, S.; Cho, B. J. Highly Air-Stable Electrical Performance of Graphene Field Effect Transistors by Interface Engineering with Amorphous Fluoropolymer. *Appl. Phys.*

Lett. **2011**, *98* (15), 153505. https://doi.org/10.1063/1.3578396.

(33) Lefebvre, J.; Ding, J.; Li, Z.; Cheng, F.; Du, N.; Malenfant, P. R. L. Hysteresis Free Carbon Nanotube Thin Film Transistors Comprising Hydrophobic Dielectrics. *Appl. Phys. Lett.* **2015**, *107* (24), 243301. https://doi.org/10.1063/1.4937223.

(34) Ameduri, B. Fluoropolymers: The Right Material for the Right Applications. *Chem. – A Eur. J.* **2018**, *24* (71), 18830–18841. https://doi.org/10.1002/CHEM.201802708.

(35) Naderi, P.; Grau, G. Organic Thin-Film Transistors with Inkjet-Printed Electrodes on Hydrophobic Teflon-AF Gate Dielectric with Reversible Surface Properties. *Org. Electron.* **2022**, *108*, 106612. https://doi.org/10.1016/J.ORGEL.2022.106612.

(36) Zanini, S.; Barni, R.; Pergola, R. Della; Riccardi, C. Modification of the PTFE Wettability by Oxygen Plasma Treatments: Influence of the Operating Parameters and Investigation of the Ageing Behaviour. *J. Phys. D. Appl. Phys.* **2014**, *47* (32), 325202. https://doi.org/10.1088/0022-3727/47/32/325202.

(37) Sprang, N.; Theirich, D.; Engemann, J. Surface Modification of Fluoropolymers by Microwave Plasmas: FTIR Investigations. *Surf. Coatings Technol.* **1998**, *98* (1–3), 865–871. https://doi.org/10.1016/S0257-8972(97)00362-9.

(38) Wilson, D. J.; Williams, R. L.; Pond, R. C. Plasma Modification of PTFE Surfaces. Part I: Surfaces Immediately Following Plasma Treatment. *Surf. Interface Anal.* **2001**, *31* (5), 385–396. https://doi.org/10.1002/SIA.1065.

(39) Vesel, A.; Mozetic, M.; Zalar, A. XPS Characterization of PTFE after Treatment with RF Oxygen and Nitrogen Plasma. *Surf. Interface Anal.* **2008**, *40* (3–4), 661–663. https://doi.org/10.1002/SIA.2691.

(40) Vandencasteele, N.; Merche, D.; Reniers, F. XPS and Contact Angle Study of N2 and O2 Plasma-Modified PTFE, PVDF and PVF Surfaces. *Surf. Interface Anal.* **2006**, *38* (4), 526–530. https://doi.org/10.1002/SIA.2255.

(41) Cho, C.-C.; Wallace, R. M.; Files-Sesler, L. A. Patterning and Etching of Amorphous Teflon Films. *J. Electron. Mater.* **1994**, *23* (8), 827–830. https://doi.org/https://doi.org/10.1007/BF02651379.

(42) Matsui, H.; Noda, Y.; Hasegawa, T. Hybrid Energy-Minimization Simulation of Equilibrium Droplet Shapes on Hydrophilic/Hydrophobic Patterned Surfaces. *Langmuir* **2012**, *28* (44), 15450–15453. https://doi.org/https://doi.org/10.1021/la303717n.

(43) Noda, Y.; Matsui, H.; Minemawari, H.; Yamada, T.; Hasegawa, T. Observation and Simulation of Microdroplet Shapes on Surface-Energy-Patterned Substrates: Contact Line Engineering for Printed Electronics. *J. Appl. Phys.* **2013**, *114* (4), 044905. https://doi.org/10.1063/1.4816461.

(44) Lefebvre, J.; Ding, J.; Li, Z.; Cheng, F.; Du, N.; Malenfant, P. R. L. Hysteresis Free Carbon Nanotube Thin Film Transistors Comprising Hydrophobic Dielectrics. *Appl. Phys. Lett.* **2015**. https://doi.org/10.1063/1.4937223.

(45) Kalb, W. L.; Mathis, T.; Haas, S.; Stassen, A. F.; Batlogg, B. Organic Small Molecule Field-Effect Transistors with Cytop^{TM} Gate Dielectric: Eliminating Gate Bias Stress Effects. *Appl. Phys. Lett.* **2007**, *90* (9), 092104. https://doi.org/10.1063/1.2709894.

(46) Sun, B.; Hong, W.; Yan, Z.; Aziz, H.; Li, Y. Record High Electron Mobility of 6.3 Cm ^{2} V $^{-1}$ s $^{-1}$ Achieved for Polymer Semiconductors Using a New Building Block. *Adv. Mater.* **2014**, *26* (17), 2636–2642. https://doi.org/10.1002/adma.201305981.

(47) Singh, R. S.; Takagi, K.; Aoki, T.; Moon, J. H.; Neo, Y.; Iwata, F.; Mimura, H.; Moraru, D. Precise Deposition of Carbon Nanotube Bundles by Inkjet-Printing on a CMOS-Compatible Platform. *Mater. 2022, Vol. 15, Page 4935* **2022**, *15* (14), 4935. https://doi.org/10.3390/MA15144935.

(48) Beecher, P.; Servati, P.; Rozhin, A.; Colli, A.; Scardaci, V.; Pisana, S.; Hasan, T.; Flewitt, A. J.; Robertson, J.; Hsieh, G. W.; Li, F. M.; Nathan, A.; Ferrari, A. C.; Milne, W. I. Ink-Jet Printing of Carbon Nanotube Thin Film Transistors. *J. Appl. Phys.* **2007**, *102* (4), 043710. https://doi.org/10.1063/1.2770835.

(49) Cao, X.; Wu, F.; Lau, C.; Liu, Y.; Liu, Q.; Zhou, C. Top-Contact Self-Aligned Printing for High-Performance Carbon Nanotube Thin-Film Transistors with Sub-Micron Channel Length. *ACS Nano* **2017**, *11* (2), 2008–2014. https://doi.org/10.1021/acsnano.6b08185.

(50) Kim, B.; Geier, M. L.; Hersam, M. C.; Dodabalapur, A. Inkjet Printed Circuits Based on Ambipolar and P-Type Carbon Nanotube Thin-Film Transistors. *Sci. Rep.* **2017**, *7*. https://doi.org/https://doi.org/10.1038/srep39627.

(51) Ervasti, H.; Järvinen, T.; Pitkänen, O.; Bozó, É.; Hiitola-Keinänen, J.; Huttunen, O. H.; Hiltunen, J.; Kordas, K. Inkjet-Deposited Single-Wall Carbon Nanotube Micropatterns on Stretchable PDMS-Ag Substrate-Electrode Structures for Piezoresistive Strain Sensing. *ACS Appl. Mater. Interfaces* **2021**, *13* (23), 27284–27294. https://doi.org/https://doi.org/10.1021/acsami.1c04397.

(52) Ammu, S.; Dua, V.; Agnihotra, S. R.; Surwade, S. P.; Phulgirkar, A.; Patel, S.; Manohar, S. K. Flexible, All-Organic Chemiresistor for Detecting Chemically Aggressive Vapors. *J. Am. Chem. Soc.* **2012**, *134* (10), 4553–4556. https://doi.org/10.1021/JA300420T/SUPPL_FILE/JA300420T_SI_002.PDF.

(53) Beyer, S. T.; Walus, K. Controlled Orientation and Alignment in Films of Single-Walled Carbon Nanotubes Using Inkjet Printing. *Langmuir* **2012**. https://doi.org/10.1021/la300770b.

(54) Kordás, K.; Mustonen, T.; Tóth, G.; Jantunen, H.; Lajunen, M.; Soldano, C.; Talapatra, S.; Kar, S.; Vajtai, R.; Ajayan, P. M. Inkjet Printing of Electrically Conductive Patterns of

Carbon Nanotubes. *Small* **2006**, *2* (8–9), 1021–1025. https://doi.org/10.1002/SMLL.200600061.

(55) Kim, B.; Geier, M. L.; Hersam, M. C.; Dodabalapur, A. Inkjet Printed Circuits on Flexible and Rigid Substrates Based on Ambipolar Carbon Nanotubes with High Operational Stability. *ACS Appl. Mater. Interfaces* **2015**, *7* (50), 27654–27660. https://doi.org/https://doi.org/10.1021/acsami.5b07727.

(56) Chen, H.; Cao, Y.; Zhang, J.; Zhou, C. Large-Scale Complementary Macroelectronics Using Hybrid Integration of Carbon Nanotubes and IGZO Thin-Film Transistors. *Nat. Commun.* **2014**. https://doi.org/10.1038/ncomms5097.

(57) Ko, H.; Tsukruk, V. V. Liquid-Crystalline Processing of Highly Oriented Carbon Nanotube Arrays for Thin-Film Transistors. *Nano Lett.* **2006**, *6* (7), 1443–1448. https://doi.org/10.1021/NL060608R/SUPPL_FILE/NL060608RSI20060531_115044.PDF.

(58) Liu, L.; Han, J.; Xu, L.; Zhou, J.; Zhao, C.; Ding, S.; Shi, H.; Xiao, M.; Ding, L.; Ma, Z.; Jin, C.; Zhang, Z.; Peng, L. M. Aligned, High-Density Semiconducting Carbon Nanotube Arrays for High-Performance Electronics. *Science (80-.).* **2020**, *368* (6493), 850–856. https://doi.org/10.1126/SCIENCE.ABA5980/SUPPL_FILE/ABA5980_LIU_SM.PDF.

(59) Oh, H.; Kim, H.; Yoo, H.; Park, B.; Chung, S.; Lee, B.; Hong, Y. Inkjet-Printing-Based Density Profile Engineering of Single-Walled Carbon Nanotube Networks for Conformable High-On/Off-Performance Thin-Film Transistors. *ACS Appl. Mater. Interfaces* **2021**, *13* (36), 43163–43173. https://doi.org/10.1021/ACSAMI.1C11891/ASSET/IMAGES/LARGE/AM1C11891_0007.JPEG.

(60) Artukovic, E.; Kaempgen, M.; Hecht, D. S.; Roth, S.; Grüner, G. Transparent and Flexible Carbon Nanotube Transistors. *Nano Lett.* **2005**, *5* (4), 757–760. https://doi.org/10.1021/NL050254O/ASSET/IMAGES/LARGE/NL050254OF00004.JPEG.

(61) Bo, X. Z.; Lee, C. Y.; Strano, M. S.; Goldfinger, M.; Nuckolls, C.; Blanchet, G. B. Carbon Nanotubes-Semiconductor Networks for Organic Electronics: The Pickup Stick Transistor. *Appl. Phys. Lett.* **2005**, *86* (18), 182102. https://doi.org/10.1063/1.1906316.

(62) Artukovic, E.; Kaempgen, M.; Hecht, D. S.; Roth, S.; Grüner, G. Transparent and Flexible Carbon Nanotube Transistors. *Nano Lett.* **2005**, *5* (4), 757–760. https://doi.org/10.1021/NL050254O/ASSET/IMAGES/LARGE/NL050254OF00004.JPEG.

(63) Rozlosnik, N.; Gerstenberg, M. C.; Larsen, N. B. Effect of Solvents and Concentration on the Formation of a Self-Assembled Monolayer of Octadecylsiloxane on Silicon (001). *Langmuir* **2003**, *19* (4), 1182–1188. https://doi.org/10.1021/LA025906S/ASSET/IMAGES/MEDIUM/LA025906SE00004.GI

F.

(64) Okimoto, H.; Takenobu, T.; Yanagi, K.; Miyata, Y.; Shimotani, H.; Kataura, H.; Iwasa, Y. Tunable Carbon Nanotube Thin-Film Transistors Produced Exclusively via Inkjet Printing. *Adv. Mater.* **2010**, *22* (36), 3981–3986. https://doi.org/10.1002/ADMA.201000889.

(65) Cui, L.; Zhang, J.; Zhang, X.; Li, Y.; Wang, Z.; Gao, H.; Wang, T.; Zhu, S.; Yu, H.; Yang, B. Avoiding Coffee Ring Structure Based on Hydrophobic Silicon Pillar Arrays during Single-Drop Evaporation. *Soft Matter* **2012**, *8* (40), 10448–10456. https://doi.org/10.1039/C2SM26271A.

(66) Lim, J. A.; Lee, W. H.; Lee, H. S.; Lee, J. H.; Park, Y. D.; Cho, K. Self-Organization of Ink-Jet-Printed Triisopropylsilylethynyl Pentacene via Evaporation-Induced Flows in a Drying Droplet. *Adv. Funct. Mater.* **2008**, *18* (2), 229–234. https://doi.org/10.1002/ADFM.200700859.

(67) Fukuda, K.; Takeda, Y.; Kobayashi, Y.; Shimizu, M.; Sekine, T.; Kumaki, D.; Kurihara, M.; Sakamoto, M.; Tokito, S. Patterning Method for Silver Nanoparticle Electrodes in Fully Solution-Processed Organic Thin-Film Transistors Using Selectively Treated Hydrophilic and Hydrophobic Surfaces. *Jpn. J. Appl. Phys.* **2013**. https://doi.org/10.7567/JJAP.52.05DB05.

(68) Hu, G.; Albrow-Owen, T.; Jin, X.; Ali, A.; Hu, Y.; Howe, R. C. T.; Shehzad, K.; Yang, Z.; Zhu, X.; Woodward, R. I.; Wu, T. C.; Jussila, H.; Wu, J. Bin; Peng, P.; Tan, P. H.; Sun, Z.; Kelleher, E. J. R.; Zhang, M.; Xu, Y.; Hasan, T. Black Phosphorus Ink Formulation for Inkjet Printing of Optoelectronics and Photonics. *Nat. Commun. 2017 81* **2017**, *8* (1), 1–10. https://doi.org/10.1038/s41467-017-00358-1.

(69) Park, B.; Jang, J.; Kim, H.; Seo, J.; Yoo, H.; Kim, T.; Hong, Y. Enhanced Current Path by Circularly and Periodically-Aligned Semiconducting Single-Walled Carbon Nanotubes for Logic Circuit Device. *Flex. Print. Electron.* **2022**, *7* (1), 015005. https://doi.org/10.1088/2058-8585/AC4EA0.

(70) Kannan Idris, M.; Naderi, P.; Melenka, G. W.; Grau, G. Damage Location Sensing in Carbon Fiber Composites Using Extrusion Printed Electronics. *Funct. Compos. Struct.* **2021**, *3* (4), 045001. https://doi.org/10.1088/2631-6331/AC3731.

(71) Kim, Y.; Lee, B.; Yang, S.; Byun, I.; Jeong, I.; Cho, S. M. Use of Copper Ink for Fabricating Conductive Electrodes and RFID Antenna Tags by Screen Printing. *Curr. Appl. Phys.* **2012**, *12* (2), 473–478. https://doi.org/10.1016/J.CAP.2011.08.003.

(72) Wu, J.; Roberts, R. C.; Tien, N. C.; Li, D. Inkjet Printed Silver Patterning on PDMS to Fabricate Microelectrodes for Microfluidic Sensing. *Proc. IEEE Sensors* **2014**, 1100–1103. https://doi.org/10.1109/ICSENS.2014.6985197.

(73) Sirringhaus, H.; Kawase, T.; Friend, R. H.; Shimoda, T.; Inbasekaran, M.; Wu, W.; Woo, E. P. High-Resolution Inkjet Printing of All-Polymer Transistor Circuits. *Science (80-.).*

2000, *290* (5499), 2123–2126. https://doi.org/10.1126/science.290.5499.2123.

(74) Ito, Y.; Heydari, M.; Hashimoto, A.; Konno, T.; Hirasawa, A.; Hori, S.; Kurita, K.; Nakajima, A. The Movement of a Water Droplet on a Gradient Surface Prepared by Photodegradation. *Langmuir* **2006**, *23* (4), 1845–1850. https://doi.org/10.1021/LA0624992.

(75) Choi, S. H.; Newby, B. M. Z. Micrometer-Scaled Gradient Surfaces Generated Using Contact Printing of Octadecyltrichlorosilane. *Langmuir* **2003**, *19* (18), 7427–7435. https://doi.org/10.1021/LA035027L.

(76) Van Den Berg, A. M. J.; De Laat, A. W. M.; Smith, P. J.; Perelaer, J.; Schubert, U. S. Geometric Control of Inkjet Printed Features Using a Gelating Polymer. *J. Mater. Chem.* **2007**, *17* (7), 677–683. https://doi.org/10.1039/B612158F.

(77) Pierre, A.; Sadeghi, M.; Payne, M. M.; Facchetti, A.; Anthony, J. E.; Arias, A. C. All-Printed Flexible Organic Transistors Enabled by Surface Tension-Guided Blade Coating. *Adv. Mater.* **2014**, *26*, 5722–5727. https://doi.org/10.1002/adma.201401520.

(78) Chen, S.; Su, M.; Zhang, C.; Gao, M.; Bao, B.; Yang, Q.; Su, B.; Song, Y.; Chen, S.; Su, M.; Zhang, C.; Gao, M.; Bao, B.; Yang, Q.; Su, B.; Song, Y. Fabrication of Nanoscale Circuits on Inkjet-Printing Patterned Substrates. *Adv. Mater.* **2015**, *27* (26), 3928–3933. https://doi.org/10.1002/ADMA.201500225.

(79) Brishty, F. P.; Grau, G. Machine Vision Methodology for Inkjet Printing Drop Sequence Generation and Validation. *Flex. Print. Electron.* **2021**, *6* (3), 035009. https://doi.org/10.1088/2058-8585/AC1C5C.

(80) Sussman, M. A Level Set Approach for Computing Solutions to Incompressible Two-Phase Flow. *J. Comput. Phys.* **1994**, *114* (1), 146–159. https://doi.org/10.1006/JCPH.1994.1155.

(81) Jacqmin, D. Calculation of Two-Phase Navier–Stokes Flows Using Phase-Field Modeling. *J. Comput. Phys.* **1999**, *155* (1), 96–127. https://doi.org/10.1006/JCPH.1999.6332.

(82) Léopoldès, J.; Dupuis, A.; Bucknall, D. G.; Yeomans, J. M. Jetting Micron-Scale Droplets onto Chemically Heterogeneous Surfaces. *Langmuir* **2003**, *19* (23), 9818–9822. https://doi.org/10.1021/LA0353069.

(83) Kusumaatmaja, H.; Yeomans, J. M. Modeling Contact Angle Hysteresis on Chemically Patterned and Superhydrophobic Surfaces. *Langmuir* **2007**, *23* (11), 6019–6032. https://doi.org/10.1021/LA063218T.

(84) Brakke, K. A. Surface Evolver Manual. **2013**.

(85) Brakke, K. A. The Surface Evolver. *Exp. Math. 1.2* **1992**, 141–165.

(86) Xu, J.; Wang, Z.; Chu, H. C. W. Unidirectional Drying of a Suspension of Diffusiophoretic Colloids under Gravity. *RSC Adv.* **2023**, *13* (14), 9247–9259.

https://doi.org/10.1039/D3RA00115F.

(87) Gerber, G.; Bensouda, M.; Weitz, D. A.; Coussot, P. Self-Limited Accumulation of Colloids in Porous Media. *Phys. Rev. Lett.* **2019**, *123* (15), 158005. https://doi.org/10.1103/PHYSREVLETT.123.158005/FIGURES/3/MEDIUM.

(88) Layani, M.; Gruchko, M.; Milo, O.; Balberg, I.; Azulay, D.; Magdassi, S. Transparent Conductive Coatings by Printing Coffee Ring Arrays Obtained at Room Temperature. *ACS Nano* **2009**, *3* (11), 3537–3542. https://doi.org/10.1021/NN901239Z/ASSET/IMAGES/LARGE/NN-2009-01239Z_0007.JPEG.

(89) Kovalchuk, N. M.; Trybala, A.; Starov, V. M. Evaporation of Sessile Droplets. *Curr. Opin. Colloid Interface Sci.* **2014**, *19* (4), 336–342. https://doi.org/10.1016/J.COCIS.2014.07.005.

(90) Kwon, J.; Jung, S.; Baek, S.; Lee, Y.; Tokito, S. Layout-to-Bitmap Conversion and Design Rules for Inkjet-Printed Large-Scale Integrated Circuits. *Langmuir* **2021**, *37* (36), 10692–10701. https://doi.org/10.1021/ACS.LANGMUIR.1C01296/ASSET/IMAGES/MEDIUM/LA1C01296_0010.GIF.

(91) Shimoni, A.; Azoubel, S.; Magdassi, S. Inkjet Printing of Flexible High-Performance Carbon Nanotube Transparent Conductive Films by "Coffee Ring Effect." *Nanoscale* **2014**, *6* (19), 11084–11089. https://doi.org/10.1039/C4NR02133A.

(92) Naderi, P.; Sheuten, B. R.; Amirfazli, A.; Grau, G. Inkjet Printing on Hydrophobic Surfaces: Controlled Pattern Formation Using Sequential Drying. *J. Chem. Phys.* **2023**, *159* (2). https://doi.org/10.1063/5.0149663/2902200.

(93) Ahosan Ul Karim, M.; Chung, S.; Alon, E.; Subramanian, V.; U Karim, M. A.; Chung, S.; Alon, E.; Subramanian, V. Fully Inkjet-Printed Stress-Tolerant Microelectromechanical Reed Relays for Large-Area Electronics. *Adv. Electron. Mater.* **2016**, *2* (5), 1500482. https://doi.org/10.1002/AELM.201500482.

(94) Chandra, S.; Di Marzo, M.; Qiao, Y. M.; Tartarini, P. Effect of Liquid-Solid Contact Angle on Droplet Evaporation. *Fire Saf. J.* **1996**, *27* (2), 141–158. https://doi.org/10.1016/S0379-7112(96)00040-9.

(95) Almohammadi, H.; Amirfazli, A. Asymmetric Spreading of a Drop upon Impact onto a Surface. *Langmuir* **2017**, *33* (23), 5957–5964. https://doi.org/10.1021/ACS.LANGMUIR.7B00704/ASSET/IMAGES/LARGE/LA-2017-00704M_0007.JPEG.

(96) Al-Chami, H.; Cretu, E. Inkjet Printing of Microsensors. *2009 IEEE 15th Int. Mix. Sensors, Syst. Test Work. IMS3TW '09* **2009**. https://doi.org/10.1109/IMS3TW.2009.5158692.

(97) Jung, Y.; Joseph Kline, R.; Fischer, D. A.; Kline, R. J.; Heeney, M.; McCulloch, L.; DeLongchamp, D. M. The Effect of Interfacial Roughness on the Thin Film Morphology and Charge Transport of High-Performance Polythiophenes. *Adv. Funct. Mater.* **2008**, *18* (5), 742–750. https://doi.org/10.1002/ADFM.200701089.

(98) Pernstich, K. P.; Oberhoff, D.; Goldmann, C.; Batlogg, B. Modeling the Water Related Trap State Created in Pentacene Transistors. *Appl. Phys. Lett.* **2006**, *89* (21), 213509. https://doi.org/10.1063/1.2396924.

(99) Salleo, A. Charge Transport in Polymeric Transistors. *Mater. Today* **2007**, *10* (3), 38–45. https://doi.org/10.1016/S1369-7021(07)70018-4.

(100) Facchetti, A.; Yoon, M.-H.; Marks, T. J. Gate Dielectrics for Organic Field-Effect Transistors: New Opportunities for Organic Electronics. *Adv. Mater.* **2005**, *17* (14), 1705–1725. https://doi.org/10.1002/ADMA.200500517.

(101) Dinelli, F.; Murgia, M.; Levy, P.; Cavallini, M.; Biscarini, F.; Leeuw, D. M. de. Spatially Correlated Charge Transport in Organic Thin Film Transistors. *Phys. Rev. Lett.* **2004**, *92* (11), 116802. https://doi.org/10.1103/PhysRevLett.92.116802.

(102) Kitahara, G.; Aoshima, K.; Tsutsumi, J.; Minemawari, H.; Arai, S.; Hasegawa, T. Low-Voltage Operation of Organic Thin-Film Transistors Based on Ultrafine Printed Silver Electrodes. *Org. Electron.* **2017**, *50*, 426–428. https://doi.org/10.1016/J.ORGEL.2017.08.023.

(103) Sekine, T.; Ikeda, H.; Kosakai, A.; Fukuda, K.; Kumaki, D.; Tokito, S. Improvement of Mechanical Durability on Organic TFT with Printed Electrodes Prepared from Nanoparticle Ink. *Appl. Surf. Sci.* **2014**. https://doi.org/10.1016/j.apsusc.2013.12.168.

(104) Lee, S. H.; Xu, Y.; Khim, D.; Park, W. T.; Kim, D. Y.; Noh, Y. Y. Effect of Polymer Gate Dielectrics on Charge Transport in Carbon Nanotube Network Transistors: Low-k Insulator for Favorable Active Interface. *ACS Appl. Mater. Interfaces* **2016**, *8* (47), 32421–32431. https://doi.org/10.1021/ACSAMI.6B06882/SUPPL_FILE/AM6B06882_SI_001.PDF.

(105) Ebnesajjad, S. *Introduction to Fluoropolymers: Materials, Technology, and Applications*; 2020.

(106) He, F.; Jin, K.; Wang, J.; Luo, Y.; Sun, J.; Fang, Q.; He, F.; Jin, K.; Wang, J.; Luo, Y.; Sun, J.; Fang, Q. New Fluoropolymers Having Both Low Water Uptake and a Low Dielectric Constant. *Macromol. Chem. Phys.* **2015**, *216* (23), 2302–2308. https://doi.org/10.1002/MACP.201500394.

(107) Zhang, H.; Weber, S. G. Teflon AF Materials. *Top. Curr. Chem.* **2011**, *308*, 307–337. https://doi.org/10.1007/128_2011_249.

(108) Legeay, G.; Coudreuse, A.; Legeais, J. M.; Werner, L.; Bulou, A.; Buzaré, J. Y.; Emery, J.; Silly, G. AF Fluoropolymer for Optical Use: Spectroscopic and Surface Energystudies;

Comparison with Other Fluoropolymers. *Eur. Polym. J.* **1998**, *34* (10), 1457–1465. https://doi.org/10.1016/S0014-3057(97)00289-9.

(109) Ha, T. J.; Kiriya, D.; Chen, K.; Javey, A. Highly Stable Hysteresis-Free Carbon Nanotube Thin-Film Transistors by Fluorocarbon Polymer Encapsulation. *ACS Appl. Mater. Interfaces* **2014**, *6* (11), 8441–8446. https://doi.org/10.1021/AM5013326.

(110) Baeg, K. J.; Noh, Y. Y.; Kim, D. Y. Charge Transfer and Trapping Properties in Polymer Gate Dielectrics for Non-Volatile Organic Field-Effect Transistor Memory Applications. *Solid. State. Electron.* **2009**, *53* (11), 1165–1168. https://doi.org/10.1016/J.SSE.2009.07.003.

(111) Wilson, D. J.; Williams, R. L.; Pond, R. C. Plasma Modification of PTFE Surfaces - Part I: Surfaces Immediately Following Plasma Treatment. *Surf. Interface Anal.* **2001**, *31* (5), 385–396. https://doi.org/10.1002/SIA.1065/FORMAT/PDF.

(112) Trapuzzano, M.; Crane, N. B.; Guldiken, R.; Tejada-Martínez, A. Wetting Metamorphosis of Hydrophobic Fluoropolymer Coatings Submerged in Water and Ultrasonically Vibrated. *J. Coatings Technol. Res. 2019 173* **2019**, *17* (3), 633–642. https://doi.org/10.1007/S11998-019-00250-1.

(113) Yoon, M.-H.; Kim, C.; Facchetti, A.; Marks, T. J. Gate Dielectric Chemical Structure-Organic Field-Effect Transistor Performance Correlations for Electron, Hole, and Ambipolar Organic Semiconductors. **2006**. https://doi.org/10.1021/ja063290d.

(114) Xu, W.; Rhee, S. W. Compromise of Electrical Leakage and Capacitance Density Effects: A Facile Route for High Mobility and Sharp Subthreshold Slope in Low-Voltage Operable Organic Field-Effect Transistors. *J. Mater. Chem.* **2011**, *21* (4), 998–1004. https://doi.org/10.1039/C0JM02401E.

(115) Sun, B.; Hong, W.; Aziz, H.; Li, Y. A Pyridine-Flanked Diketopyrrolopyrrole (DPP)-Based Donor–Acceptor Polymer Showing High Mobility in Ambipolar and n-Channel Organic Thin Film Transistors. *Polym. Chem.* **2015**, *6* (6), 938–945. https://doi.org/10.1039/C4PY01193G.

(116) Liu, Q.; Wang, Y.; Kohara, A.; Matsumoto, H.; Manzhos, S.; Feron, K.; Bottle, S. E.; Bell, J.; Michinobu, T.; Sonar, P. Tuning the Charge Carrier Polarity of Organic Transistors by Varying the Electron Affinity of the Flanked Units in Diketopyrrolopyrrole-Based Copolymers. *Adv. Funct. Mater.* **2020**, *30* (7), 1907452. https://doi.org/10.1002/ADFM.201907452.

(117) Jurchescu, O. D.; Popinciuc, M.; Van Wees, B. J.; Palstra, T. T. M. Interface-Controlled, High-Mobility Organic Transistors. *Adv. Mater.* **2007**, *19* (5), 688–692. https://doi.org/10.1002/ADMA.200600929/FORMAT/PDF.

(118) Dong, J.; Yu, P.; Arabi, S. A.; Wang, J.; He, J.; Jiang, C. Enhanced Mobility in Organic Field-Effect Transistors Due to Semiconductor/Dielectric Interface Control and Very Thin

Single Crystal. *Nanotechnology* **2016**, *27* (27), 275202. https://doi.org/10.1088/0957-4484/27/27/275202.

(119) Shichao Zhang; Yunfeng Qiu; Huihui Yang; Dao Wang; Yunxia Hu; Xubing Lu; Zhonghua Li; PingAn Hu. The Role of Hybrid Dielectric Interfaces in Improving the Performance of Multilayer InSe Transistors. *J. Mater. Chem. C* **2020**, *8* (20), 6701–6709. https://doi.org/10.1039/D0TC00331J.

(120) Meiron, T. S.; Marmur, A.; Saguy, I. S. Contact Angle Measurement on Rough Surfaces. *J. Colloid Interface Sci.* **2004**, *274* (2), 637–644. https://doi.org/10.1016/J.JCIS.2004.02.036.

(121) Miller, J. D.; Veeramasuneni, S.; Drelich, J.; Yalamanchili, M. R.; Yamauchi, G. Effect of Roughness as Determined by Atomic Force Microscopy on the Wetting Properties of PTFE Thin Films. *Polym. Eng. Sci.* **1996**, *36* (14), 1849–1855. https://doi.org/10.1002/PEN.10580.

(122) Liu, Q.; Yu, J.; Wang, H. The Role of the Substrate Roughness in Contact Angle Hysteresis and Dynamic Deviation. *Int. J. Heat Mass Transf.* **2020**, *148*, 118985. https://doi.org/10.1016/J.IJHEATMASSTRANSFER.2019.118985.

(123) Li, Y.; Liu, C.; Xu, Y.; Minari, T.; Darmawan, P.; Tsukagoshi, K. Solution-Processed Organic Crystals for Field-Effect Transistor Arrays with Smooth Semiconductor/Dielectric Interface on Paper Substrates. *Org. Electron.* **2012**, *13* (5), 815–819. https://doi.org/10.1016/J.ORGEL.2012.01.021.

(124) Horowitz, G.; Hajlaoui, M. E. Grain Size Dependent Mobility in Polycrystalline Organic Field-Effect Transistors. *Synth. Met.* **2001**, *122* (1), 185–189. https://doi.org/10.1016/S0379-6779(00)01351-5.

(125) Geiger, M.; Acharya, R.; Reutter, E.; Ferschke, T.; Zschieschang, U.; Weis, J.; Pflaum, J.; Klauk, H.; Weitz, R. T. Effect of the Degree of the Gate-Dielectric Surface Roughness on the Performance of Bottom-Gate Organic Thin-Film Transistors. *Adv. Mater. Interfaces* **2020**, *7* (10), 1902145. https://doi.org/10.1002/ADMI.201902145.

(126) Wang, J.; Wu, Y.; Cao, Y.; Li, G.; Liao, Y. Influence of Surface Roughness on Contact Angle Hysteresis and Spreading Work. https://doi.org/10.1007/s00396-020-04680-x/Published.

(127) Spori, D. M.; Drobek, T.; Zürcher, S.; Ochsner, M.; Sprecher, C.; Mühlebach, A.; Spencer, N. D. Beyond the Lotus Effect: Roughness Influences on Wetting over a Wide Surface-Energy Range. *Langmuir* **2008**, *24* (10), 5411–5417. https://doi.org/10.1021/LA800215R.

(128) Bracco, G.; Holst, B. *Surface Science Techniques*; Springer Science & Business Media, 2013.

(129) Nason, T. C.; Moore, J. A.; Lu, T. -M. Deposition of Amorphous Fluoropolymer Thin Films by Thermolysis of Teflon Amorphous Fluoropolymer. *Appl. Phys. Lett.* **1998**, *60* (15), 1866.

https://doi.org/10.1063/1.107163.

(130) Abdmouleh, M.; Jedidi, I.; Khitouni, M.; Salah, A. Ben; Kabadou, A. LDPE PHASE COMPOSITION IN LDPE/Cu COMPOSITES USING THERMAL ANALYSIS AND FTIR SPECTROSCOPY.

(131) Ding, S. J.; Wang, P. F.; Wan, X. G.; Zhang, D. W.; Wang, J. T.; Lee, W. W. Effects of Thermal Treatment on Porous Amorphous Fluoropolymer Film with a Low Dielectric Constant. *Mater. Sci. Eng. B* **2001**, *83* (1–3), 130–136. https://doi.org/10.1016/S0921-5107(01)00504-9.

(132) Cioffi, N.; Torsi, L.; Farella, I.; Altamura, D.; Valentini, A.; Ditaranto, N.; Sabbatini, L.; Zambonin, P. G.; Bleve-Zacheo, T. Deposition and Analytical Characterization of Fluoropolymer Thin Films Modified by Palladium Nanoparticles. *Thin Solid Films* **2004**, *449* (1–2), 25–33. https://doi.org/10.1016/J.TSF.2003.10.016.

(133) Sandrin, L.; Silverstein, M. S.; Sacher, E. Fluorine Incorporation in Plasma-Polymerized Octofluorocyclobutane, Hexafluoropropylene and Trifluoroethylene. *Polymer (Guildf).* **2001**, *42* (8), 3761–3769. https://doi.org/10.1016/S0032-3861(00)00693-5.

(134) Suzuki, Y.; Fu, H.; Abe, Y.; Kawamura, M. Effects of Substrate Temperature on Structure and Mechanical Properties of Sputter Deposited Fluorocarbon Thin Films. *Vacuum* **2013**, *87*, 218–221. https://doi.org/10.1016/J.VACUUM.2012.05.029.

(135) Gnanappa, A. K.; O'Murchu, C.; Slattery, O.; Peters, F.; Aszalós-Kiss, B.; Tofail, S. A. M. Effect of Annealing on Hydrophobic Stability of Plasma Deposited Fluoropolymer Coatings. *Polym. Degrad. Stab.* **2008**, *93* (12), 2119–2126. https://doi.org/10.1016/J.POLYMDEGRADSTAB.2008.08.012.

(136) Gardella, J.; Ferguson, S. A.; Chin, R. L. Π* ← π Shakeup Satellites for the Analysis of Structure and Bonding in Aromatic Polymers by X-Ray Photoelectron Spectroscopy: *http://dx.doi.org/10.1366/0003702864509565* **2016**, *40* (2), 224–232. https://doi.org/10.1366/0003702864509565.

(137) Taylor, J. A.; Lancaster, G. M.; Rabalais, J. W. Surface Alteration of Graphite, Graphite Monofluoride and Teflon by Interaction with Ar+ and Xe+ Beams. *Appl. Surf. Sci.* **1978**, *1* (4), 503–514. https://doi.org/10.1016/0378-5963(78)90027-2.

(138) Avval, T. G.; Chatterjee, S.; Bahr, S.; Dietrich, P.; Meyer, M.; Thißen, A.; Linford, M. R. Carbon Dioxide Gas, CO2(g), by near-Ambient Pressure XPS. *Surf. Sci. Spectra* **2019**, *26* (1), 014022. https://doi.org/10.1116/1.5053761.

(139) De La Puente, G.; Pis, J. J.; Menéndez, J. A.; Grange, P. Thermal Stability of Oxygenated Functions in Activated Carbons. *J. Anal. Appl. Pyrolysis* **1997**, *43* (2), 125–138. https://doi.org/10.1016/S0165-2370(97)00060-0.

(140) Everhart, D. S.; Reilley, C. N. Polymer Functional Group Mobility. 2—Partition of Ion Pairs

between Hydrophobic and Hydrophilic Phases of Plasma Oxidized Polyethylene. *Surf. Interface Anal.* **1981**, *3* (6), 258–268. https://doi.org/10.1002/SIA.740030606.

(141) Qiu, Y.; Wei, P.; Wang, Z.; Lu, W.; Jiang, Y.; Zhang, C.; Qu, Y.; Lu, G. Manipulating Doping of Organic Semiconductors by Reactive Oxygen for Field-Effect Transistors. *Phys. status solidi – Rapid Res. Lett.* **2018**, *12* (10), 1800297. https://doi.org/10.1002/PSSR.201800297.

(142) Kimura, Y.; Kitamura, M.; Kitani, A.; Arakawa, Y. Operational Stability in Pentacene Thin-Film Transistors with Threshold Voltages Tuned by Oxygen Plasma Treatment. *Jpn. J. Appl. Phys.* **2016**, *55* (2), 02BB14. https://doi.org/10.7567/JJAP.55.02BB14/XML.

(143) Yunker, P. J.; Still, T.; Lohr, M. A.; Yodh, A. G. Suppression of the Coffee-Ring Effect by Shape-Dependent Capillary Interactions. *Nat. 2011 4767360* **2011**, *476* (7360), 308–311. https://doi.org/10.1038/nature10344.

(144) Song, J. W.; Kim, J.; Yoon, Y. H.; Choi, B. S.; Kim, J. H.; Han, C. S. Inkjet Printing of Single-Walled Carbon Nanotubes and Electrical Characterization of the Line Pattern. *Nanotechnology* **2008**, *19* (9). https://doi.org/10.1088/0957-4484/19/9/095702.

(145) Cao, C.; Andrews, J. B.; Kumar, A.; Franklin, A. D. Improving Contact Interfaces in Fully Printed Carbon Nanotube Thin-Film Transistors. *ACS Nano* **2016**, *10* (5), 5221–5229. https://doi.org/10.1021/ACSNANO.6B00877/SUPPL_FILE/NN6B00877_SI_001.PDF.

(146) Cardenas, J. A.; Upshaw, S.; Williams, N. X.; Catenacci, M. J.; Wiley, B. J.; Franklin, A. D.; Cardenas, J. A.; Upshaw, S.; Williams, N. X.; Franklin, A. D.; Catenacci, M. J.; Wiley, B. J. Impact of Morphology on Printed Contact Performance in Carbon Nanotube Thin-Film Transistors. *Adv. Funct. Mater.* **2019**, *29* (1), 1805727. https://doi.org/10.1002/ADFM.201805727.

(147) Choi, S. J.; Wang, C.; Chi Lo, C.; Bennett, P.; Javey, A.; Bokor, J. Comparative Study of Solution-Processed Carbon Nanotube Network Transistors. *Appl. Phys. Lett.* **2012**, *101* (11), 112104. https://doi.org/10.1063/1.4752006/127334.

(148) Brishty, F. P.; Urner, R.; Grau, G. Machine Learning Based Data Driven Inkjet Printed Electronics: Jetting Prediction for Novel Inks. *Flex. Print. Electron.* **2022**, *7* (1), 015009. https://doi.org/10.1088/2058-8585/AC5A39.

(149) Derby, B. Inkjet Printing of Functional and Structural Materials: Fluid Property Requirements, Feature Stability, and Resolution. *https://doi.org/10.1146/annurev-matsci-070909-104502* **2010**, *40*, 395–414. https://doi.org/10.1146/ANNUREV-MATSCI-070909-104502.

(150) Ravi, S.; Kaiser, A. B.; Bumby, C. W. Improved Conduction in Transparent Single Walled Carbon Nanotube Networks Drop-Cast from Volatile Amine Dispersions. *Chem. Phys. Lett.* **2010**, *496* (1–3), 80–85. https://doi.org/10.1016/J.CPLETT.2010.06.084.

(151) Wang, C.; Wang, Y.; Yao, Y.; Luo, W.; Wan, J.; Dai, J.; Hitz, E.; Fu, K.; Hu, L.; Wang, C.; Wang, Y.; Yao, Y.; Luo, W.; Wan, J.; Dai, J.; Hitz, E.; Fu, K.; Hu, L. A Solution-Processed High-Temperature, Flexible, Thin-Film Actuator. *Adv. Mater.* **2016**, *28* (39), 8618–8624. https://doi.org/10.1002/ADMA.201602777.

(152) Lau, P. H.; Takei, K.; Wang, C.; Ju, Y.; Kim, J.; Yu, Z.; Takahashi, T.; Cho, G.; Javey, A. Fully Printed, High Performance Carbon Nanotube Thin-Film Transistors on Flexible Substrates. *Nano Lett.* **2013**, *13* (8), 3864–3869. https://doi.org/10.1021/NL401934A/SUPPL_FILE/NL401934A_SI_001.PDF.

(153) Street, R. A.; Salleo, A. Contact Effects in Polymer Transistors. *Appl. Phys. Lett* **2002**, *81*, 2887. https://doi.org/https://doi.org/10.1063/1.1512950.

(154) Lin, D. W.; Bettinger, C. J.; Ferreira, J. P.; Wang, C. L.; Bao, Z. A Cell-Compatible Conductive Film from a Carbon Nanotube Network Adsorbed on Poly-L-Lysine. *ACS Nano* **2011**, *5* (12), 10026–10032. https://doi.org/10.1021/NN203870C/ASSET/IMAGES/LARGE/NN-2011-03870C_0005.JPEG.

(155) Schießl, S. P.; De Vries, X.; Rother, M.; Massé, A.; Brohmann, M.; Bobbert, P. A.; Zaumseil, J. Modeling Carrier Density Dependent Charge Transport in Semiconducting Carbon Nanotube Networks. *Phys. Rev. Mater.* **2017**, *1*, 46003. https://doi.org/10.1103/PhysRevMaterials.1.046003.

(156) Zorn, N. F.; Zaumseil, J. Charge Transport in Semiconducting Carbon Nanotube Networks. *Appl. Phys. Rev.* **2021**, *8* (4), 041318. https://doi.org/10.1063/5.0065730.

(157) Klimm, W.; Kwok, K. Tunneling Resistance Model for Piezoresistive Carbon Nanotube Polymer Composites. *Nanotechnology* **2022**, *34* (4), 045502. https://doi.org/10.1088/1361-6528/AC9C0D.

(158) Gong, Q.; Bhatt, V. D.; Albert, E.; Abdellah, A.; Fabel, B.; Lugli, P.; Scarpa, G. On the Performance of Solution-Processable Random Network Carbon Nanotube Transistors: Unveiling the Role of Network Density and Metallic Tube Content. *IEEE Trans. Nanotechnol.* **2014**, *13* (6), 1181–1185. https://doi.org/10.1109/TNANO.2014.2351011.

(159) Balberg, I.; Binenbaum, N.; Anderson, C. H. Critical Behavior of the Two-Dimensional Sticks System. *Phys. Rev. Lett.* **1983**, *51* (18), 1605. https://doi.org/10.1103/PhysRevLett.51.1605.

(160) Balberg, I.; Binenbaum, N. Computer Study of the Percolation Threshold in a Two-Dimensional Anisotropic System of Conducting Sticks. *Phys. Rev. B* **1983**, *28* (7), 3799. https://doi.org/10.1103/PhysRevB.28.3799.

(161) Munson-Mcgee, S. H. Estimation of the Critical Concentration in an Anisotropic Percolation Network. *Phys. Rev. B* **1991**, *43* (4), 3331. https://doi.org/10.1103/PhysRevB.43.3331.

(162) Hoffmann, T.; Martínez-Salazar, J.; Herrero, P.; Petermann, J. Percolative Behavior of an Anisotropic Two-Dimensional Network:Growth of Tellurium onto an Oriented Polymer Film. *Phys. Rev. B* **1997**, *55* (3), 1858. https://doi.org/10.1103/PhysRevB.55.1858.